

8-2009

Improved Thermoelectric Performance of P-type Polycrystalline Bi₂Te₃ via Hydrothermal Treatment with Alkali Metal Salts

Zhe Su

Clemson University, zsu@clermson.edu

Follow this and additional works at: https://tigerprints.clemson.edu/all_dissertations

 Part of the [Physics Commons](#)

Recommended Citation

Su, Zhe, "Improved Thermoelectric Performance of P-type Polycrystalline Bi₂Te₃ via Hydrothermal Treatment with Alkali Metal Salts" (2009). *All Dissertations*. 420.

https://tigerprints.clemson.edu/all_dissertations/420

This Dissertation is brought to you for free and open access by the Dissertations at TigerPrints. It has been accepted for inclusion in All Dissertations by an authorized administrator of TigerPrints. For more information, please contact kokeefe@clemson.edu.

IMPROVED THERMOELECTRIC PERFORMANCE OF P-TYPE
POLYCRYSTALLINE Bi_2Te_3 VIA HYDROTHERMAL TREATMENT
WITH ALKALI METAL SALTS

A Thesis
Presented to
the Graduate School of
Clemson University

In Partial Fulfillment
of the Requirements for the Degree
Doctor of Philosophy
Physics

by
Zhe Su
August 2009

Accepted by:
Dr. Terry Tritt, Committee Chair
Dr. Joseph Manson
Dr. Murray Daw
Dr. Fivos Drymiotis

ABSTRACT

The field of thermoelectric research has attracted a lot of interest in hope of helping address the energy crisis. In recent years, low-dimensional thermoelectric materials have been found promising and thus become a popular school of thought. However, the high complexity and cost for fabricating low-dimensional materials give rise to the attempt to further improve conventional bulk polycrystalline materials. Polycrystals are featured by numerous grain boundaries that can scatter heat-carrying phonons to significantly reduce the thermal conductivity κ whereas at the same time can unfortunately deteriorate the electrical resistivity ρ . Aiming at the dualism of the grain boundaries in determining the transport properties of polycrystalline materials, a novel concept of “grain boundary engineering” has been proposed in order to have a thermoelectrically favorable grain boundary. In this dissertation, a polycrystalline p-type Bi_2Te_3 system has been intensively investigated in light of such a concept that was realized through a hydrothermal nano-coating treatment technique.

P-type $\text{Bi}_{0.4}\text{Sb}_{1.6}\text{Te}_3$ powder was hydrothermally treated with alkali metal salt XBH_4 ($X = \text{Na}, \text{K}$ or Rb) solution. After the treatment, there formed an alkali-metal-containing surface layer of nanometers thick on the p- Bi_2Te_3 grains. The Na-treatment, leaving the Seebeck coefficient α almost untouched, lowered κ the most while the Rb-treatment at the same time increased α slightly and decreased ρ the most. Compared to the untreated sample, Na- and Rb-treatments improved the dimensionless figure of merit ZT by $\sim 30\%$ due to the reduced κ and $\sim 38\%$ owing to the improved the power factor PF ,

respectively. The grain boundary phase provides a new avenue by which one can potentially decouple the otherwise inter-related α , ρ and κ within one thermoelectric material. The morphologic investigation showed this surface layer lacked crystallinity, if any, and was possibly an amorphous phase.

Once Na- and Rb-treatments with various molar ratios were applied to the same sample, a similar grain boundary layer formed with a compositional gradient along the depth direction. The Hall effect measurements showed that the grain boundary phase introduced new carriers into the system and thereby compensated the loss in mobility. With α almost untouched, the ρ to κ ratio has been optimized by varying the Na:Rb ratio in the starting solution. As a result, the Na:Rb = 1:2 ratio yielded the best ZT value of ~ 0.92 at 350K, comparable with that of the state-of-the-art p-Bi₂Te₃ commercial ingot.

Besides ZT , the hydrothermal treatment lessened the temperature dependence of compatibility factor S of as-treated polycrystalline samples, helping a thermoelectric device have overall better performance even if it did not work under its optimal condition.

DEDICATION

This dissertation is dedicated to my parents, Xiangyun Su and Shuiyun Yu, and my sister, Jun Su, in China. I could not have made it without their deep love, great support and encouragement.

ACKNOWLEDGEMENTS

I would like to thank my advisor and the committee chair, Dr. Terry M. Tritt, for his motivation, guidance, support and patience. I would like to extend my gratitude to Dr. Joseph R. Manson, Dr. Murray S. Daw and Dr. Fivos R. Drymiotis for serving on the committee.

I would like to express my sincere gratitude to Dr. Jian He for his great help, encouragement, friendship, enlightening discussions and instructions throughout the completion of this project presented in this dissertation. I am also deeply grateful to Dr. Xihua Ji who sparked the idea to initiate the project and synthesized the samples.

I would like to thank Dr. Jeff Sharp of Marlow Industries, Inc. for providing the p-type Bi_2Te_3 ingots. I would like to thank Dr. Colin McMillen of the Department of Chemistry, Clemson University, who did the TGA and XRD analyses. Also, I would like to thank Jason Reppert of Dr. Apparao M. Rao's group for the Raman spectroscopy. Finally, I would like to thank every member of the Complex and Advanced Materials Laboratory, Department of Physics and Astronomy, Clemson University, who makes the group a great team to learn from each other and work with.

The author also acknowledges the financial support from the Department of Energy/EPSCoR Implementation Grant (No. DE-FG02-04ER-46139) and the SC EPSCoR Office/Clemson University cost sharing.

TABLE OF CONTENT

	Page
TITLE PAGE	i
ABSTRACT.....	ii
DEDICATION	iv
ACKNOWLEDGEMENTS	v
LIST OF TABLES	ix
LIST OF FIGURES	x
CHAPTER	
1. INTRODUCTION	1
1.1 The Seebeck Effect.....	1
1.2 The Peltier Effect	3
1.3 The Thomson Effect.....	5
1.4 The Energy Conversion Efficiencies.....	7
1.5 The Early Years of Thermoelectrics	9
1.6 Thermoelectrics in the Early and Middle 20th Century	10
1.7 State-of-the-art Thermoelectric Materials	14
1.8 The Trends in Thermoelectric Research	18

Table of Contents (Continued)

	Page
1.9 Thermoelectric Modules and Applications	22
2. HYDROTHERMAL TREATMENT WITH SINGLE ALKALI METAL SALTS	26
2.1 Motivations.....	26
2.2 Synthesis and Characterization	29
2.3 The Effects of Particle Size on Thermoelectric Properties	34
2.4 Effects of Different Alkali Metal Salts.....	41
2.5 Conclusion.....	52
3. SURFACE LAYER ON THE GRAIN BOUNDARY AFTER THE HYDROTHERMAL TREATMENT	53
3.1 Introduction	53
3.2 Composition of Surface Layers.....	54
3.3 Structure of Surface Layers.....	61
3.4 Possibility of Alkali Atoms' Intercalation into the Bi ₂ Te ₃ Matrix	67
3.5 TGA Analysis.....	72
3.6 Conclusion.....	74

Table of Contents (Continued)

	Page
4. HYDROTHERMAL TREATMENT WITH COMBINED ALKALI METAL SALTS	75
4.1 Introduction	75
4.2 Sample Synthesis.....	76
4.3 Microscopic Images	77
4.4 The Decoupling of Thermoelectric Properties	79
4.5 Thermoelectric Properties of Na-and-Rb-Treated Samples	82
4.6 The Change in n and μ after Hydrothermal Treatment	89
4.7 Conclusion.....	93
5. THE IMPROVEMENT IN COMPATIBILITY FACTOR.....	95
5.1 Introduction	95
5.2 The Temperature Dependence of the Compatibility Factor	98
5.3 The Improvement in Overall Performance.....	98
5.4 Conclusion.....	105
6. SUMMARY	107
REFERENCES	112

LIST OF TABLES

Table	Page
2.1 The electrical transport properties at 310K of p-type $\text{Bi}_{0.4}\text{Sb}_{1.6}\text{Te}_3$ polycrystalline samples.....	51

LIST OF FIGURES

Figure		Page
1.1	The diagram of the Seebeck effect	2
1.2	The diagram of the Peltier effect	4
1.3	The diagram of the Thomson effect	6
1.4	Schematic dependence of electrical conductivity, Seebeck coefficient, power factor, and thermal conductivity on concentration of free carrier.....	13
1.5	The dimensionless figure-of-merit ZT of established state-of-the- art thermoelectric materials as a function of temperature T	16
1.6	Electronic density of states (DOS) changes as the dimensionality is decreased from 3D bulk crystalline to 2D quantum well to 1D quantum wire and 0D quantum dot.....	21
1.7	The schematic bandgap of Bi nanowire transition from semimetal to semiconductor as the diameter d_w of the nanowire is decreased.....	21
1.8	The schematic drawing of PbTe/ PbSe _{0.98} Te _{0.02} quantum-dot superlattice	21
1.9	Thermoelectric elements made of p- and n-type legs.....	23

Table of Figures (Continued)

Figure	Page
2.1 The diagram of p-type polycrystalline $\text{Bi}_{0.4}\text{Sb}_{1.6}\text{Te}_3$ sample preparation procedures.....	30
2.2 The anisotropy of thermal diffusivity D of p-type $\text{Bi}_{0.4}\text{Sb}_{1.6}\text{Te}_3$ pellet due to the texture formed during hot-press	32
2.3 (a) The diagram of realignment of p-type $\text{Bi}_{0.4}\text{Sb}_{1.6}\text{Te}_3$ bars cut from the pellet and (b) actual pictures of such realigned bars	33
2.4 The Seebeck coefficient α as a function of temperature T for hydrothermally Na-treated p-type $\text{Bi}_{0.4}\text{Sb}_{1.6}\text{Te}_3$ polycrystalline samples prepared with powder of particle sizes $<20\ \mu\text{m}$, $20 \sim 32\ \mu\text{m}$ and $32 \sim 45\ \mu\text{m}$, respectively	35
2.5 The electrical resistivity ρ as a function of temperature T for hydrothermally Na-treated p-type $\text{Bi}_{0.4}\text{Sb}_{1.6}\text{Te}_3$ polycrystalline samples prepared with powder of particle sizes $<20\ \mu\text{m}$, $20 \sim 32\ \mu\text{m}$ and $32 \sim 45\ \mu\text{m}$, respectively	36
2.6 The power factor PF as a function of temperature T for hydrothermally Na-treated p-type $\text{Bi}_{0.4}\text{Sb}_{1.6}\text{Te}_3$ polycrystalline samples prepared with powder of particle sizes $<20\ \mu\text{m}$, $20 \sim 32\ \mu\text{m}$ and $32 \sim 45\ \mu\text{m}$, respectively	37

Table of Figures (Continued)

Figure	Page
2.7 The thermal conductivity κ as a function of temperature T for hydrothermally Na-treated p-type $\text{Bi}_{0.4}\text{Sb}_{1.6}\text{Te}_3$ polycrystalline samples prepared with powder of particle sizes $<20\ \mu\text{m}$, $20 \sim 32\ \mu\text{m}$ and $32 \sim 45\ \mu\text{m}$, respectively	38
2.8 The dimensionless figure of merit ZT as a function of temperature T for hydrothermally Na-treated p-type $\text{Bi}_{0.4}\text{Sb}_{1.6}\text{Te}_3$ polycrystalline samples prepared with powder of particle sizes $<20\ \mu\text{m}$, $20 \sim 32\ \mu\text{m}$ and $32 \sim 45\ \mu\text{m}$, respectively	40
2.9 The Seebeck coefficient α as a function of temperature T for p-type $\text{Bi}_{0.4}\text{Sb}_{1.6}\text{Te}_3$ polycrystalline samples hydrothermally treated with Na, K and Rb metal salts, respectively, and untreated Bulk Reference, all of which are prepared with powder of particle size $<20\ \mu\text{m}$	42
2.10 The electrical resistivity ρ as a function of temperature T for p-type $\text{Bi}_{0.4}\text{Sb}_{1.6}\text{Te}_3$ polycrystalline samples hydrothermally treated with Na, K and Rb salts, respectively, and untreated Bulk Reference, all of which are prepared with powder of particle size $<20\ \mu\text{m}$	43

Table of Figures (Continued)

Figure	Page
2.11 The power factor PF as a function of temperature T for p-type $\text{Bi}_{0.4}\text{Sb}_{1.6}\text{Te}_3$ polycrystalline samples hydrothermally treated with Na, K and Rb salts, respectively, and untreated Bulk Reference, all of which are prepared with powder of particle size $<20\ \mu\text{m}$	44
2.12 The thermal conductivity κ as a function of temperature T for p-type $\text{Bi}_{0.4}\text{Sb}_{1.6}\text{Te}_3$ polycrystalline samples hydrothermally treated with Na, K and Rb salts, respectively, and untreated Bulk Reference, all of which are prepared with powder of particle size $<20\ \mu\text{m}$	46
2.13 The lattice thermal conductivity κ_L as a function of temperature T for p-type $\text{Bi}_{0.4}\text{Sb}_{1.6}\text{Te}_3$ polycrystalline samples hydrothermally treated with Na, K and Rb salts, respectively, and untreated Bulk Reference, all of which are prepared with powder of particle size $<20\ \mu\text{m}$	48
2.14 The dimensionless figure of merit ZT as a function of temperature T for p-type $\text{Bi}_{0.4}\text{Sb}_{1.6}\text{Te}_3$ polycrystalline samples hydrothermally treated with Na, K and Rb salts, respectively,	

Table of Figures (Continued)

Figure	Page
and untreated Bulk Reference, all of which are prepared with powder of particle size $<20 \mu\text{m}$	49
2.15 Itemized contributions at temperature $T = 323\text{K}$ from the thermal conductivity κ , the lattice thermal conductivity κ_L and the power factor PF to the enhancements in the dimensionless figure of merit ZT of p-type $\text{Bi}_{0.4}\text{Sb}_{1.6}\text{Te}_3$ polycrystalline samples hydrothermally treated with Na, K and Rb salts, respectively, all of which are prepared with powder of particle size $<20 \mu\text{m}$	50
3.1 The FESEM pictures of p-type $\text{Bi}_{0.4}\text{Sb}_{1.6}\text{Te}_3$ grains (a) with and (b) without the hydrothermal treatment, while (c) and (d) show clearer details in smaller scales about the fluffy surface after the treatment	55
3.2 SEM pictures of commercial p-type $\text{Bi}_{0.4}\text{Sb}_{1.6}\text{Te}_3$ ingot after hydrothermal treatment.....	56
3.3 The EDS analysis of the surface layer formed on the hydrothermally treated p-type $\text{Bi}_{0.4}\text{Sb}_{1.6}\text{Te}_3$ ingot	57

Table of Figures (Continued)

Figure	Page
3.4 The EDS analysis of a Na-hydrothermally treated p-type $\text{Bi}_{0.4}\text{Sb}_{1.6}\text{Te}_3$ grain.....	59
3.5 The XRD patterns of p-type $\text{Bi}_{0.4}\text{Sb}_{1.6}\text{Te}_3$ powders before and after hydrothermal treatment	60
3.6 (a) The LEED pattern of untreated p-type $\text{Bi}_{0.4}\text{Sb}_{1.6}\text{Te}_3$ grains. (b) The SAED pattern of treated p-type $\text{Bi}_{0.4}\text{Sb}_{1.6}\text{Te}_3$ grains	62
3.7 The HRTEM images of p-type $\text{Bi}_{0.4}\text{Sb}_{1.6}\text{Te}_3$ grains (a) before and (b) after the hydrothermal treatment.....	63
3.8 The easy peeling of the surface layer from hydrothermally treated p-type $\text{Bi}_{0.4}\text{Sb}_{1.6}\text{Te}_3$ grains after ultrasonic vibration.....	65
3.9 The SAED image of the surface layers peeled off from hydrothermally treated p-type $\text{Bi}_{0.4}\text{Sb}_{1.6}\text{Te}_3$ grains after ultrasonic vibration	66
3.10 The lattice structure of Bi_2Te_3	68
3.11 The Fourier transform infrared absorption spectra of untreated and hydrothermally treated p-type $\text{Bi}_{0.4}\text{Sb}_{1.6}\text{Te}_3$ samples	70
3.12 The Raman spectra of untreated and hydrothermally treated p-type $\text{Bi}_{0.4}\text{Sb}_{1.6}\text{Te}_3$ samples	71

Table of Figures (Continued)

Figure	Page
3.13 The TGA analysis of untreated, Na- and K-treated p-type $\text{Bi}_{0.4}\text{Sb}_{1.6}\text{Te}_3$ polycrystalline samples	73
4.1 A TEM image of combined Na- and Rb-treated $\text{Bi}_{0.4}\text{Sb}_{1.6}\text{Te}_3$ grain	78
4.2 The compositional dependences of the Seebeck coefficient α , resistivity ρ , lattice thermal conductivity κ_L , thermal conductivity κ , power factor PF and ZT of Na- and Rb- treated polycrystalline p- Bi_2Te_3 samples at 300K.....	80
4.3 At 300K, ZT as a function of σ/κ , the ratio of the electrical to thermal conductivity for hydrothermally treated polycrystalline p- Bi_2Te_3 samples.....	81
4.4 The Seebeck coefficient α as a function of temperature T for the as-hydrothermally treated polycrystalline p-type $\text{Bi}_{0.4}\text{Sb}_{1.6}\text{Te}_3$ samples compared with the Ingot and the Bulk Reference.....	83
4.5 The electric resistivity ρ as a function of temperature T for the as-hydrothermally treated polycrystalline p-type $\text{Bi}_{0.4}\text{Sb}_{1.6}\text{Te}_3$ samples compared with the Ingot and the Bulk Reference.....	84

Table of Figures (Continued)

Figure	Page
4.6 The power factor PF as a function of temperature T for the as-hydrothermally treated polycrystalline p-type $\text{Bi}_{0.4}\text{Sb}_{1.6}\text{Te}_3$ samples compared with the Ingot and the Bulk Reference.....	85
4.7 The thermal conductivity κ as a function of temperature T for the as-hydrothermally treated polycrystalline p-type $\text{Bi}_{0.4}\text{Sb}_{1.6}\text{Te}_3$ samples compared with the Ingot and the Bulk Reference.....	87
4.8 The lattice thermal conductivity κ_L as a function of temperature T for the as-hydrothermally treated polycrystalline p-type $\text{Bi}_{0.4}\text{Sb}_{1.6}\text{Te}_3$ samples compared with the Ingot and the Bulk Reference	88
4.9 The dimensionless figure of merit ZT as a function of temperature T for the as-hydrothermally treated polycrystalline p-type $\text{Bi}_{0.4}\text{Sb}_{1.6}\text{Te}_3$ samples compared with the Ingot and the Bulk Reference	90
4.10 The Hall mobility μ as a function of temperature T for the as-hydrothermally treated polycrystalline p-type $\text{Bi}_{0.4}\text{Sb}_{1.6}\text{Te}_3$ samples compared with the Ingot and the Bulk Reference.....	91

Table of Figures (Continued)

Figure	Page
4.11 The carrier concentration n as a function of temperature T for the as-hydrothermally treated polycrystalline p-type $\text{Bi}_{0.4}\text{Sb}_{1.6}\text{Te}_3$ samples compared with the Ingot and the Bulk Reference.....	92
5.1 The compatibility factor S as a function of temperature T for the as-hydrothermally treated polycrystalline p-type $\text{Bi}_{0.4}\text{Sb}_{1.6}\text{Te}_3$ samples compared with the ingot and the Bulk Reference.....	99
5.2 The reduced efficiency η_r of the p-type $\text{Bi}_{0.4}\text{Sb}_{1.6}\text{Te}_3$ ingot as a function of temperature T and the relative current density u	100
5.3 The reduced efficiency η_r of the 1Na2Rb-hydrothermally treated p-type $\text{Bi}_{0.4}\text{Sb}_{1.6}\text{Te}_3$ polycrystalline sample as a function of temperature T and the relative current density u	101
5.4 The comparison of the reduced efficiency η_r between the p-type $\text{Bi}_{0.4}\text{Sb}_{1.6}\text{Te}_3$ ingot and 1Na2Rb-hydrothermally treated sample.....	103
5.5 The percent difference between the total efficiency of the 1Na2Rb-treated sample, $\eta_{1\text{Na}2\text{Rb}}$, and that of the ingot, η_{ingot} , when the relative current density u deviates from S_{middle} , the compatibility factor value at the midpoint temperature for a	

Table of Figures (Continued)

Figure	Page
thermoelectric element sandwiched between cold and hot ends, T_c and T_h , respectively	104

1. INTRODUCTION

1.1 The Seebeck Effect

The imminent oil crisis has revitalized research on thermoelectricity as an alternative power generation approach.¹⁻³ Thermoelectric effects actually consist of three separate effects, the Seebeck effect, the Peltier effect and the Thomson effect, all of which were named after their discoverers.⁴⁻⁶ Being the first effect reported, the Seebeck effect (Figure 1.1) was discovered in 1821 by Thomas Johann Seebeck who observed the deflection of a compass needle due to a nearby circuit made from two dissimilar metals, with junctions at different temperatures.⁷ The temperature difference ΔT produced an electrical potential ΔV that drove a current in the circuit which, as per Ampere's law, deflected the compass. ΔV is found to be proportional to ΔT if ΔT is small across the sample. Therefore, the Seebeck coefficient α , or the thermopower, can be defined as

$$\alpha = -\frac{\Delta V}{\Delta T} \quad (1.1)$$

The measurement in Figure 1.1 involves two different materials, thus the resultant α is actually the relative Seebeck coefficient $\alpha_{AB} = \alpha_A - \alpha_B$, where α_A and α_B are the absolute Seebeck coefficients of Metal A and B, respectively. Even if Metal B is removed, the thermoelectric voltage read by the voltmeter inevitably contains the thermoelectric voltage across the measurement electrodes due to the temperature gradient established there whenever the electrodes are placed onto the sample. Therefore, unless

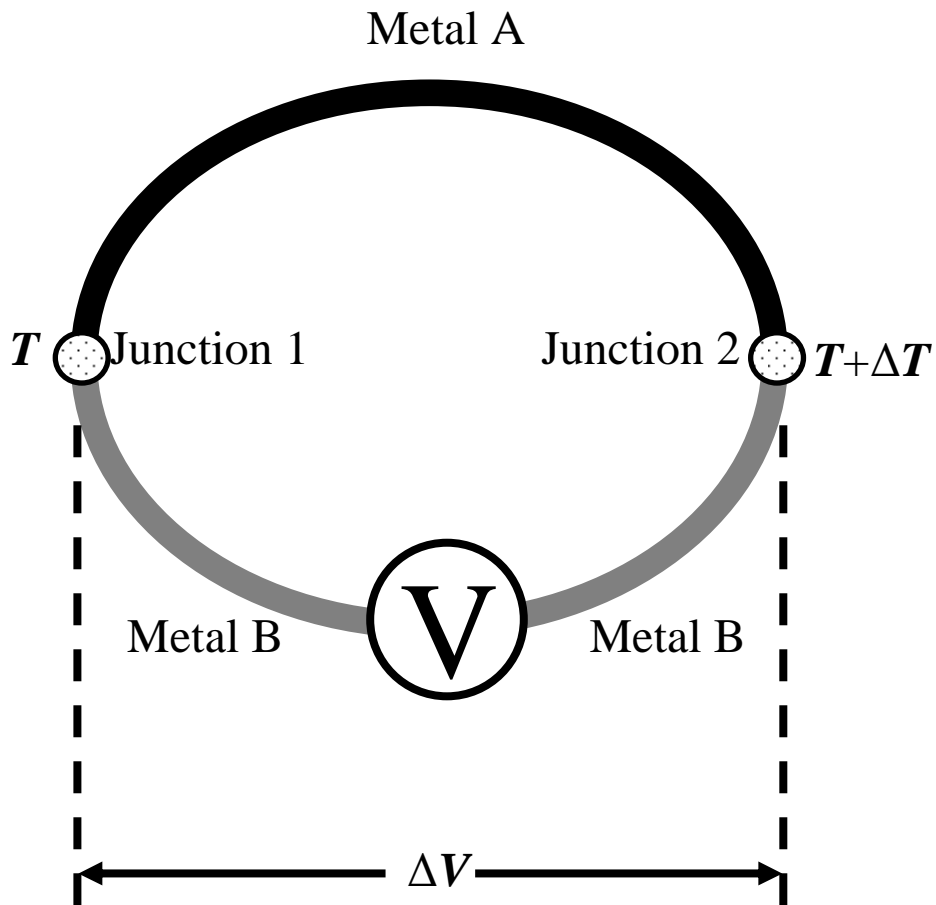


Figure 1.1 The diagram of the Seebeck effect. An electrical potential difference ΔV is established when Junction 1 and 2, where two metals A and B join, are put at different temperatures T and $T + \Delta T$.

one metal in Figure 1.1 is a superconductor whose absolute Seebeck coefficient is zero,⁸ there is no way to directly measure a material's absolute Seebeck coefficient, which, however, can be deduced from the Thomson relationships that will be discussed in the following paragraphs.

1.2 The Peltier Effect

The Peltier effect was discovered by Jean-Charles Peltier in 1834.⁹ In Figure 1.2, when a current I flows through the circuit clockwise made of Metals A and B, heat is absorbed at Junction 1 and repelled at Junction 2, depending on the direction of the current and the metals in use. If the current passes through the circuit counterclockwise, heat would be absorbed at Junction 2 and repelled at Junction 1. One may conveniently analogize the Peltier effect to the “reversed” Seebeck effect. Likewise, the proportionality exists between the heat flow rate dQ/dt and the current I , i.e.,

$$\frac{dQ}{dt} = \Pi_{AB} I = (\Pi_B - \Pi_A) I \quad (1.2)$$

where Π_{AB} is the relative Peltier coefficient, and Π_A and Π_B are the coefficients of Metals A and B, respectively. The determination of the exact values of Π_A and Π_B also relies on the Thomson relationships discussed below. In the Peltier effect, one can change the direction of heat flow by controlling the direction of the current. Therefore, the Peltier effect has found its application in thermoelectric refrigeration other than in power generation, which is currently the most discussed applications of thermoelectric materials.

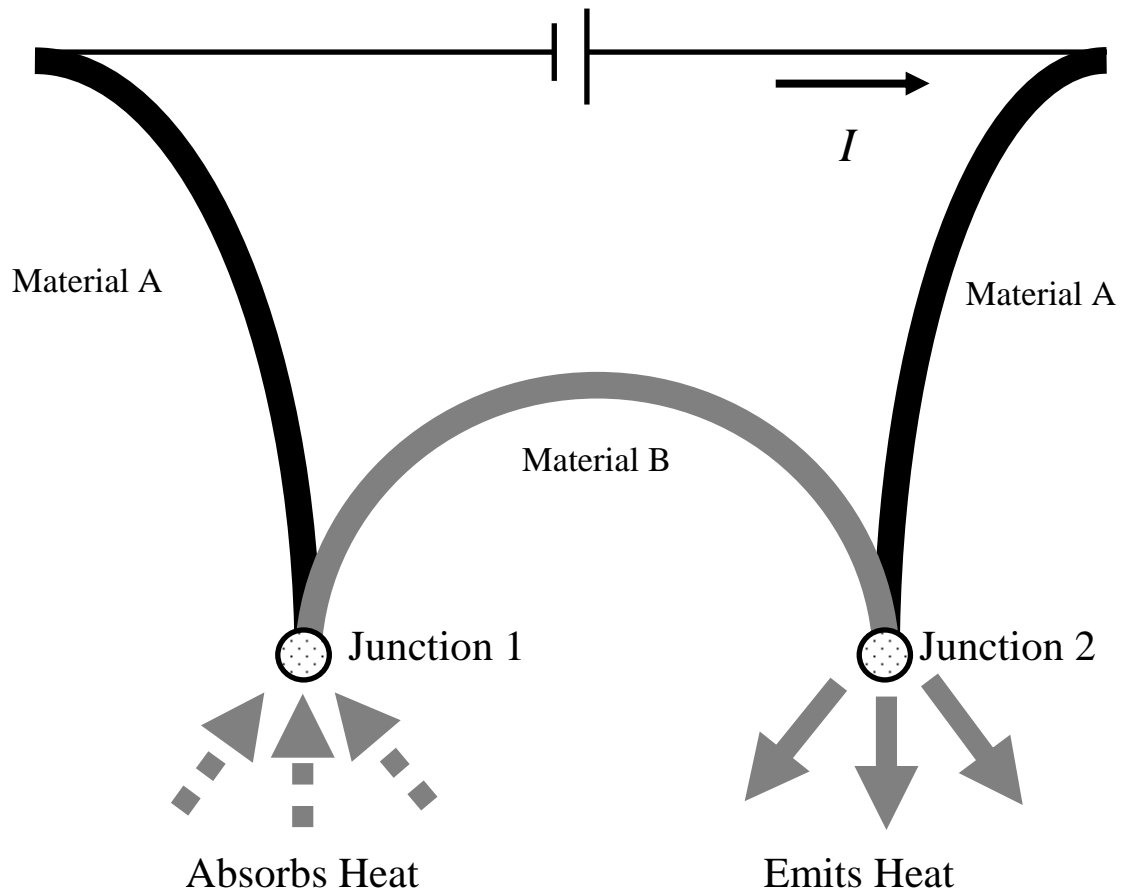


Figure 1.2 The diagram of the Peltier effect. When the current I is flowing through Junction 1 and 2 made of materials A and B, heat is absorbed at Junction 1 and emitted at another.

1.3 The Thomson Effect

In 1851 William Thomson predicted and proved in experiments that in the presence of a temperature gradient, the heat emission or absorption take places not only at the junctions where two different materials meet but also for any homogeneous material that carries a current.^{10,11} In Figure 1.3, two ends of a current carrying wire are put at different temperatures. The heat absorption or emission rate per unit length of the wire is

$$\frac{dq}{dt} = \tau_{th} I \frac{dT}{dx} \quad (1.3)$$

where I is the current, τ_{th} , the Thomson coefficient and dT/dx , the temperature gradient along the wire. Given the material, heat is absorbed or emitted depending on the sign of I .

Unlike the Seebeck and Peltier coefficients, one can determine an individual material's Thomson coefficient from Eq. 1.3. Accordingly, the absolute value of Thomson coefficient is the only thermoelectric coefficient that can be directly measured. To solve for other two thermoelectric coefficients, Thomson developed two relationships bearing his name to relate all three thermoelectric coefficients α , Π and τ_{th} :

$$\Pi = \alpha T \quad (1.4)$$

$$\tau_{th} = T \frac{d\alpha}{dT} \quad (1.5)$$

where T is the temperature. The absolute values of α and Π can be deduced using Equations 1.4 and 1.5 once τ_{th} is measured against T .

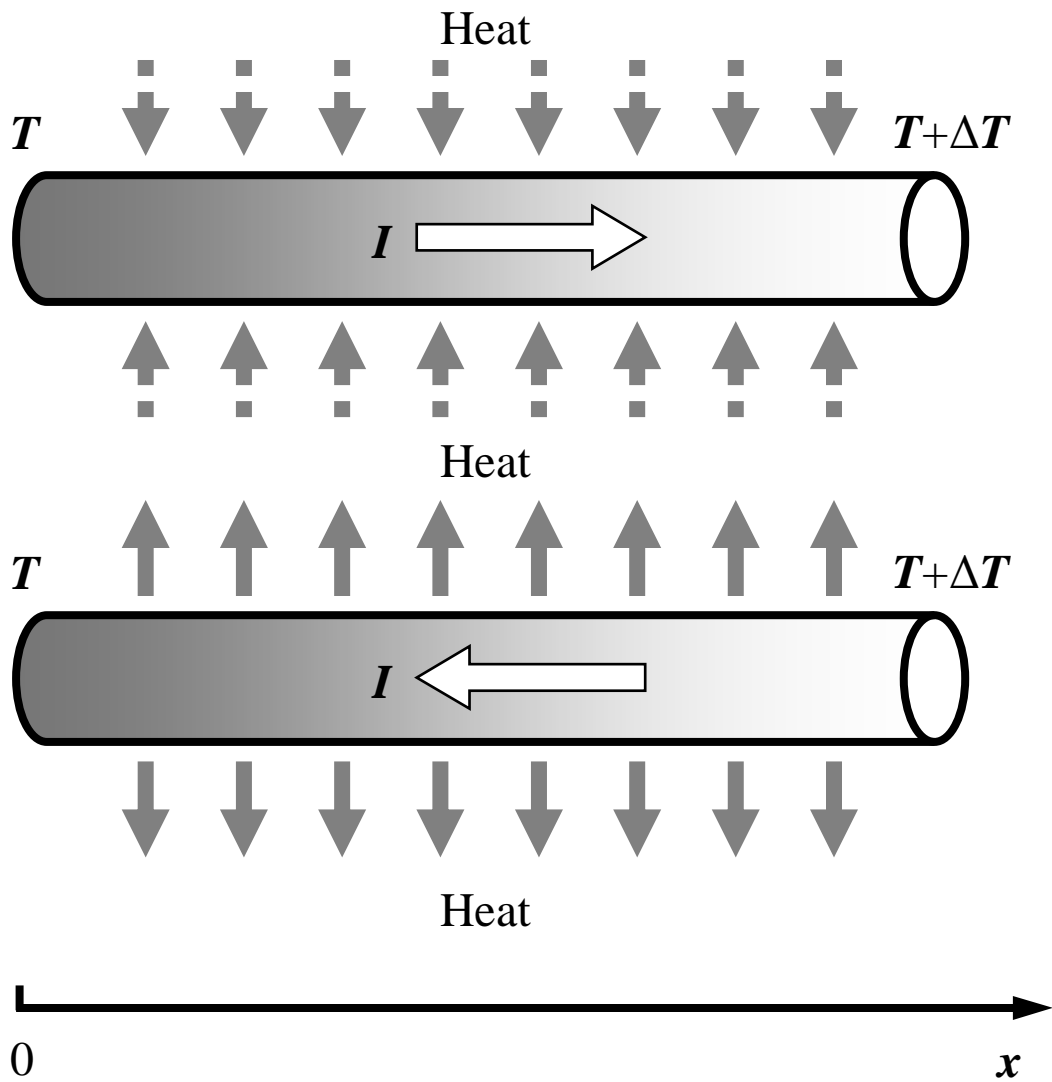


Figure 1.3 The diagram of the Thomson effect. When two ends of a wire carrying current I are at different temperatures T and $T + \Delta T$, heat is absorbed (upper) or emitted (lower) along the wire depending on the direction of I .

1.4 The Energy Conversion Efficiencies⁴⁻⁶

The direct application of the Seebeck effect is power generation. If the work output by a thermoelectric material is w when the net heat it absorbs from the high and low temperature ends T_c and T_h , respectively, is q_H , the efficiency η can be expressed as

$$\eta = \frac{w}{q_H} \approx \frac{T_h - T_c}{T_h} \cdot \frac{\sqrt{1 + ZT} - 1}{\sqrt{1 + ZT} + \frac{T_c}{T_h}} \quad (1.6)$$

where

$$T = \frac{T_h + T_c}{2} \quad (1.7)$$

$$Z = \frac{\alpha^2}{\rho\kappa} = \frac{\alpha^2\sigma}{\kappa} \quad (1.8)$$

In Eq. 1.8, α , ρ and κ are the material's Seebeck coefficient, electrical resistivity and thermal conductivity, respectively, and σ is the electrical conductivity, i.e., the reciprocal of ρ . Z , which is in the unit of K^{-1} , is defined as the figure of merit of a thermoelectric material. However, as Z is temperature dependent, the product of Z and T , or the dimensionless figure of merit,

$$ZT = \frac{\alpha^2 T}{\rho\kappa} = \frac{\alpha^2 \sigma T}{\kappa} \quad (1.9)$$

which conveniently results in a dimensionless number, is more appropriately and frequently referred in order to characterize a thermoelectric material's power generation

efficiency at a specific temperature. Except for superconductors whose Seebeck coefficients are zero, thermoelectric effects exist in almost all conducting materials. Nevertheless, only materials of $ZT > 0.5$ are considered as promising thermoelectric materials.

The expression of ZT in Eq. 1.9 is often written as the ratio of power factor PF to the thermal conductivity κ

$$ZT = \frac{PF}{\kappa} \quad (1.10)$$

where

$$PF = \frac{\alpha^2 T}{\rho} = \alpha^2 \sigma T \quad (1.11)$$

Different from the expression in Eq. 1.11, the PF is often defined as $\alpha^2 \sigma$ in many other literatures. The author would like to remind the readers that the definition of PF in Eq. 1.11 applies throughout this dissertation unless otherwise indicated. As its name implies, thermoelectricity aims at the relation between thermal and electrical energies. The PF is more a parameter reflecting a material's electrical transport properties while κ more describes the material's thermal transport properties. As per Eq. 1.10, improving ZT is to optimize the ratio of PF to κ .

For thermoelectric refrigeration, the coefficient of performance is approximately

$$\phi = \frac{T_c}{T_h - T_c} \cdot \frac{\sqrt{1+ZT} - \frac{T_h}{T_c}}{\sqrt{1+ZT} + 1} \quad (1.12)$$

Based on Eq. 1.6, one may conclude that the bigger the ZT , the higher the η with an upper limit $\eta \leq 1$. However, a thermoelectric generator works like a heat engine that converts thermal energy into electric power, thus the upper limit for the generator's efficiency, according to the laws of thermodynamics, should be the Carnot efficiency

$$\eta_c = \frac{T_h - T_c}{T_c} \quad (1.13)$$

As per Eq. 1.9, a high ZT thermoelectric material should simultaneously possess high Seebeck coefficient, low electrical resistivity and thermal conductivity. Unfortunately, the inter-relationships among those three parameters often make the improvement in one parameter lead to the deterioration in the other two. How to preferably tune up the thermoelectric properties in a balanced way is the focus of today's thermoelectric research, and also the topic of this dissertation.

1.5 The Early Years of Thermoelectrics

Although the Seebeck effect was once employed for small DC power generation, it was replaced due to the low efficiency after Faraday discovered electromagnetic induction. In 1909 ~ 1911 Altenkirch developed the first correct (macroscopic) theory of thermoelectric energy conversion that included all three parameters: the Seebeck coefficient, electrical resistivity and thermal conductivity.^{12,13} His theory showed a good thermoelectric material should have a large Seebeck coefficient and low electrical resistivity and thermal conductivity at the same time. According to such criteria, metals only meet the requirement for low electrical resistivity but fail in the other two due to

very small Seebeck coefficients and high thermal conductivities. It is hence deemed that metals' efficiency for thermoelectric power generation or refrigeration is too low for any worthwhile practical application.

Because of people's lack of knowledge on semiconductors at that time, the perspectives for thermoelectric research were dim in the first century after the discovery of thermoelectric effects. As a matter of fact, no thermoelectric material worthy of practical applications for energy conversion or refrigeration had been found, and thermoelectricity had been retained mainly in its direct application, i.e., fabricating metallic thermocouples for temperature measurement. Shown in Figure 1.1, two dissimilar metals are joined together, and the temperature difference between two junctions is obtained by measuring the magnitude of the voltage established. The dependence of such voltage against temperature depends on the combination of the metals in use and can typically range from one to tens of μV 's per K. After calibration, metallic thermocouples present satisfactory measurement accuracy over a wide temperature region. Since the thermocouple only reads the voltage and thus the temperature difference between two junctions, in many cases one junction is placed at a known temperature so that the temperature at the other junction can be deduced.

1.6 Thermoelectrics in the Early and Middle 20th Century

The 20th century witnessed the boom of solid state physics and, especially semiconductor physics, which eventually promoted the research and development of

thermoelectric materials. Having conducted an enormous amount of research on crystals throughout the 1920s, Ioffe, who established Physical-Technical Institute (PTI) of the USSR, began to focus on semiconductors for potentially promising thermoelectric materials in the 1930s.¹⁴ As the first semiconductor thermoelectric material of his and his group's interests, PbS was employed to make the first useful thermoelectric generator that could power a radio station in the World War II. After the war and in the 1950s, PTI successfully synthesized a series of thermoelectric materials such as PbTe, ZnSb and, most notably, the ternary alloy (Bi, Sb)₂Te₃, which was first introduced in 1953 and later historically reached maximum $ZT \sim 1$ after optimizations in compositions and synthesis techniques.¹⁵ Possessing a ZT peak around 300 K, (Bi, Sb)₂Te₃ alloy has been employed primarily for thermoelectric refrigeration since the 1950s.¹⁶ It is also the most successful thermoelectric material that has been commercialized.

Besides all the new effective thermoelectric materials found in PTI, Ioffe made remarkable contributions to both macroscopic and microscopic thermoelectric theories.¹⁷ Ioffe was the first one to use Z as defined in Eq. 1.8 to characterize thermoelectric materials. Considering the α^2 term in the expression for Z , the optimization of the Seebeck coefficient is of great importance. He deliberately selected elements of high atomic number for new thermoelectric material syntheses. He also proposed that the charge carrier concentration at room temperature for a good thermoelectric material should be between $(0.5\sim 1.0) \times 10^{19} \text{cm}^{-3}$, which means the best thermoelectric should be a degenerate semiconductor or a semimetal. Not only did Ioffe's and his group's discoveries of new materials make thermoelectric leap from laboratories into practical

applications, but also his theories have constituted the basis of thermoelectricity in the following half century.

1.1 Basic Principles for Developing Thermoelectric Materials

Now it is postulated that an ideal thermoelectric material should have a Seebeck coefficient of $100 \sim 300 \mu\text{V/K}$ as well as appropriate carrier concentration as mentioned above ($\sim 10^{19} \text{ cm}^{-3}$) that enables it to possess a thermoelectrically favorable electrical resistivity between $10^{-4} \sim 10^{-2} \Omega\cdot\text{cm}$. Figure 1.4 shows a schematic relationship between ZT and the carrier concentration.⁶ Increasing carrier concentration n would increase electrical conductivity σ but adversely decrease the Seebeck coefficient α . Because these two quantities compete against each other, the electrical power factor $\alpha^2\sigma$ does not vary monotonically with n but, as the upper panel of Figure 1.4 shows, reaches the maximum when n is $1 \times 10^{19} \text{ cm}^{-3}$, which is typical of semiconductors.

The lower panel of Figure 1.4 shows the thermal conductivity κ also increases with n and the reasons are elaborated as follows. The thermal conductivity κ consists of contributions from two parts,

$$\kappa = \kappa_e + \kappa_L \quad (1.14)$$

where κ_e is the electronic thermal conductivity and κ_L is lattice thermal conductivity, respectively.

Note

$$\sigma = en\mu \quad (1.15)$$

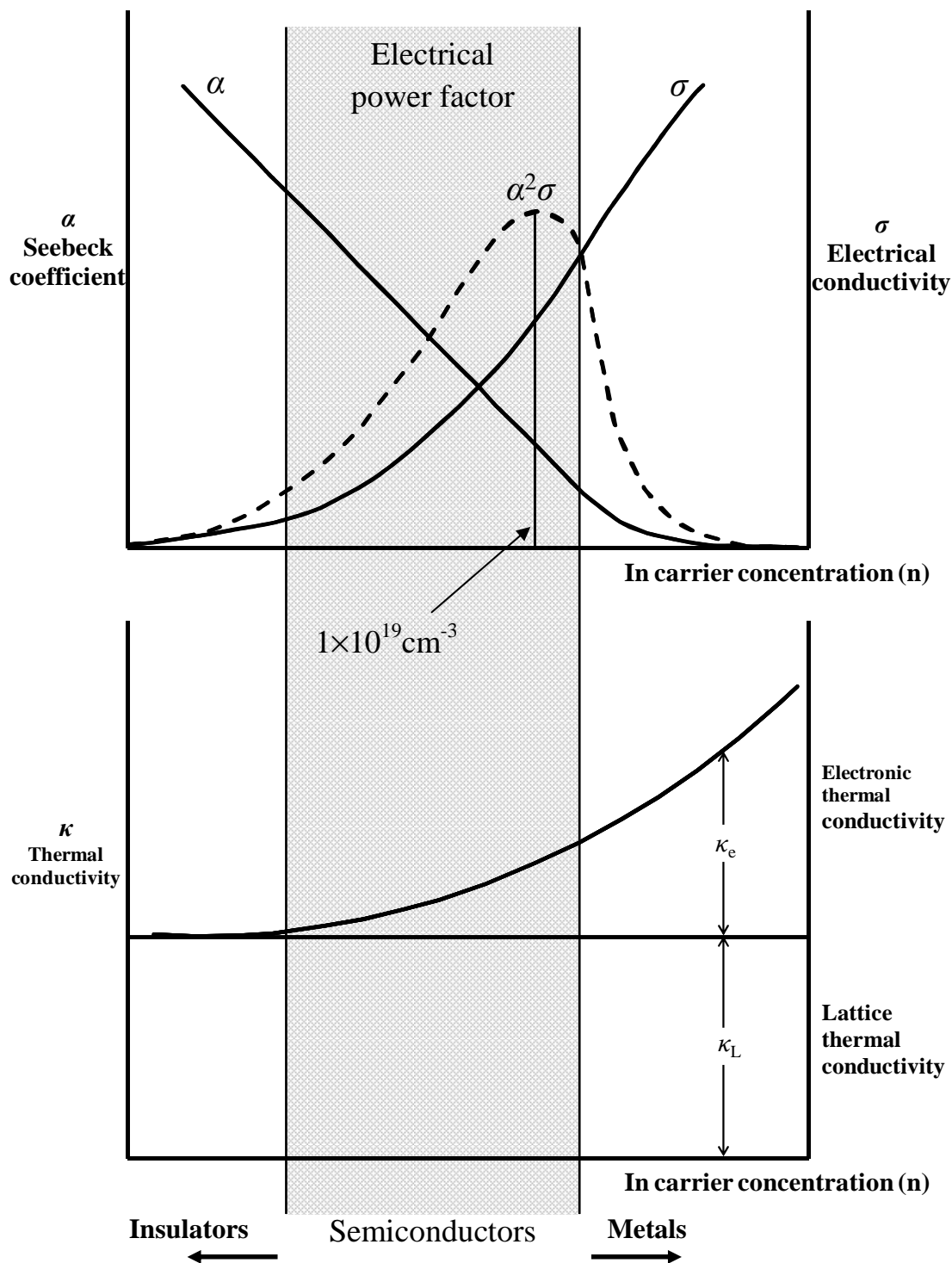


Figure 1.4 Schematic dependence of electrical conductivity, Seebeck coefficient, power factor, and thermal conductivity on concentration of free carrier.⁶

where e is the electron charge, n the carrier concentration and μ the carrier mobility. Although κ_l may be independent of n in Figure 1.4, the increase in n would in most cases result in an increase in σ according to Eq. 1.15 and therefore leads to the increase in κ_e according to the Wiedemann-Franz relationship

$$\kappa_e = L\sigma T \quad (1.16)$$

where L , the Lorenz number, is usually taken as $2.44 \times 10^{-8} \text{ W}\Omega/\text{K}^2$ for free electrons and T is the temperature.

In summary, a material's thermal conductivity increases with carrier concentration while its electrical power factor may reach a maximum at a certain point. A good thermoelectric material should balance the electrical power factor and the thermal conductivity so that the ratio of these two parameters could be maximized. According to the carrier concentration dependent behaviors of α , σ and κ , semiconductors have, when compared with insulators and metals, moderate values in all three parameters such as the Seebeck coefficient, electrical and thermal conductivities. Accordingly, in Figure 1.4 the peak of electrical power factor falls in the region of semiconductors while the electronic part of thermal conductivity is relatively low. Therefore, overall semiconductors can achieve much better thermoelectric performances than insulators and metals.

1.7 State-of-the-art Thermoelectric Materials

Nowadays, most established thermoelectric materials are semiconductors. There exist two kinds of thermoelectric materials in terms of the charge type of the free carriers.

One is p-type and the other is n-type. The majority carriers of p-type thermoelectric materials are holes while those of n-type materials are electrons. So these two types of thermoelectric materials have positive and negative Seebeck coefficients, respectively. The dimensionless figure of merit ZT 's of some established state-of-the-art thermoelectric materials as a function of temperature are shown in Figure 1.5 regardless of the carrier charge type of the materials.^{18,19} According to the temperature regions where their ZT peaks appear, those established thermoelectric materials can be divided into three groups: the low-temperature (< 500 K), mid-temperature (500 ~ 900 K) and high-temperature (> 900 K) thermoelectric materials. Within more than ten thermoelectric materials in such a broad temperature range in Figure 1.5, however, $ZT = 1$ is an upper limit for most of them with only a few exceptions.

As per Eq. 1.13, the bigger the relative temperature difference across the thermoelectric material, the higher efficiency could be. Since the cold end of a thermoelectric material is often placed at room temperature, the temperature difference across the low-temperature thermoelectric materials is about 200 K at most. Thus, low-temperature thermoelectric materials are not so competitive in power generation applications, especially for those whose ZT 's peak below room temperature such as BiSb and CsBi₄Te₆. Accordingly, low-temperature thermoelectric materials are often employed in small amount of waste heat recovery and refrigeration. With the ZT peak around 400 K, Bi₂Te₃ is a typical low-temperature thermoelectric material. In order to best tune the carrier concentration and at the same time lower the lattice thermal conductivity, it is alloyed with Sb₂Te₃ so that the composition of the p-type Bi₂Te₃ system is close

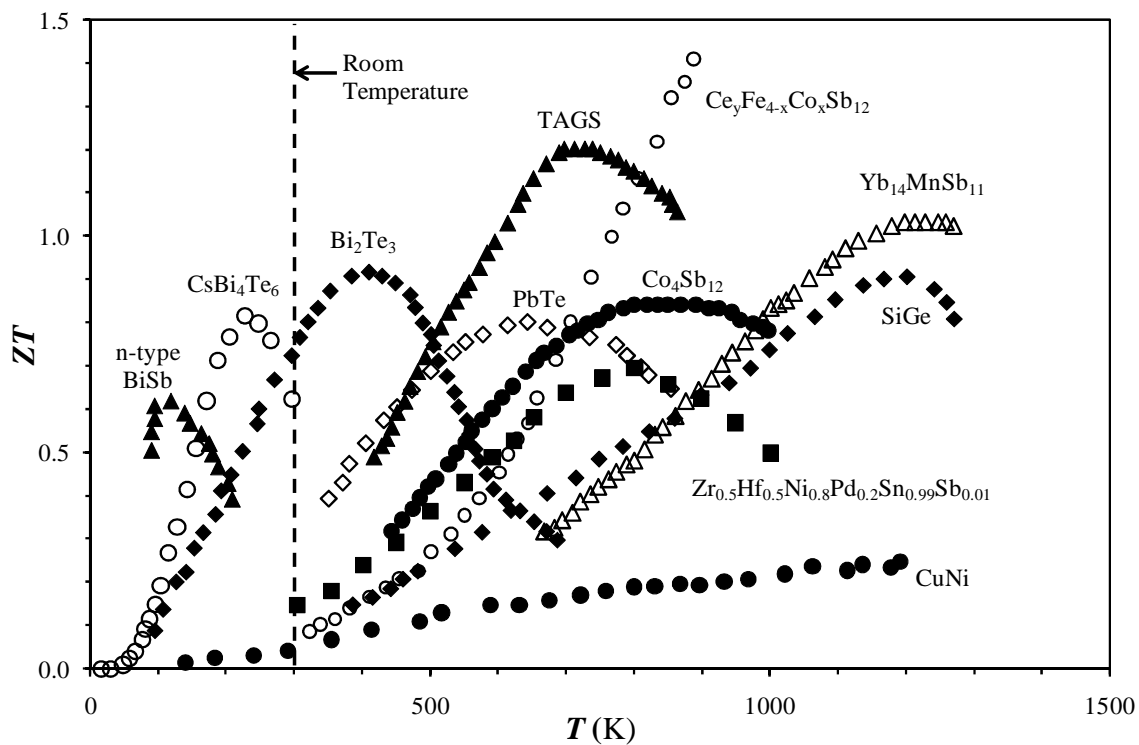


Figure 1.5 The dimensionless figure-of-merit ZT of established state-of-the-art thermoelectric materials as a function of temperature T .^{18,19}

to $(\text{Sb}_{0.8}\text{Bi}_{0.2})_2\text{Te}_3$ while that of n-type one is about $\text{Bi}_2(\text{Te}_{0.8}\text{Se}_{0.2})_3$.⁶ Having been long commercialized, both p- and n-type Bi_2Te_3 based alloys have so far been the best thermoelectric materials in this temperature region ever since they were first synthesized in the 1950s^{20,21}, and they are still receiving a lot of attention in recent years.²²⁻²⁵

There are several classes of well-established mid-temperature thermoelectric materials. One family of them such as PbTe , GeTe and SnTe ²⁶⁻³⁰ are based on group-IV tellurides. Figure 1.5 shows most of them have ZT values smaller than 1 except that $(\text{GeTe})_{0.85}(\text{AgSbTe}_2)_{0.15}$, or TAGS, has a reported $ZT > 1.2$.⁴ The skutterudites such as $\text{Co}_4\text{Sb}_{12}$ and $\text{Fe}_4\text{Sb}_{12}$ make up another group of promising mid-temperature thermoelectric material because of their high Seebeck coefficient and electrical conductivity. However, their intrinsic high lattice thermal conductivities inhibit their ZT values, for example, $ZT < 1$ for $\text{Co}_4\text{Sb}_{12}$ (see Figure 1.5). To lower the thermal conductivity without deteriorating the electrical conductivity too much, the remedy is to fill two voids in the skutterudite lattice with foreign atoms which are loosely bound. Those foreign atoms selected are usually rare-earth elements with heavy atomic masses, and they become rattlers in the lattice to selectively scatter heat conducting phonons more than electrons. Such an approach results in, for instance, $ZT > 1$ for La-, Yb-, Er- and In-filled $\text{Co}_4\text{Sb}_{12}$ and even higher ZT for $\text{Ce}_y\text{Fe}_{4-x}\text{Co}_x\text{Sb}_{12}$ which is synthesized by Ce-filling after substitution of Co for Fe in $\text{Fe}_4\text{Sb}_{12}$.³¹⁻³⁷ Half-Heusler alloys are a group of ternary intermetallic compounds with a general formula MNiSn in which $\text{M} = \text{Zr}, \text{Hf}, \text{or Ni}$.³⁸ Like skutterudites, high thermal conductivities leave half-Heusler compounds a lot of room for improvement although they demonstrate excellent electrical transport properties.

Their thermoelectric performance can be preferably tuned up by appropriate annealing and/or doping.^{39 - 41} Figure 1.5 demonstrates their perspectives as promising mid-temperature thermoelectric materials for $\text{Zr}_{0.5}\text{Hf}_{0.5}\text{Ni}_{0.8}\text{Pd}_{0.2}\text{Sn}_{0.99}\text{Sb}_{0.01}$.⁴²

High-temperature thermoelectric materials can find their applications in deep space probes and forming the hot end segment in a segmented thermoelectric converter that incorporates mid- and low-temperature materials in order to fully utilize the temperature gradient between the hot and cold ends. In the high temperature regime up to 1200 K, SiGe has been the most commonly used thermoelectric material for over 20 years.⁴³ SiGe has diamond structure lattice, which enables it to withstand high temperature. Nevertheless, the consequent high lattice thermal conductivity adversely results in relatively low $ZT < 1$ as shown in Figure 1.5. Although in recent years the operative temperatures of a few n-type materials have gone beyond 1000 K, those of p-type materials remained below 1000 K. Such an imbalance limits the efficiency of thermoelectric devices and persisted until the emerging of Zintl phase compound $\text{Yb}_{14}\text{MnSb}_{11}$, whose ZT is ~ 1.0 at 1200 K,⁴⁴ a value almost twice that of p-type SiGe. Unlike SiGe, Zintl phase compounds have very complex crystal and band structures⁴⁵, leading to low lattice thermal conductivity and leaving room for future improvements.⁴⁶

1.8 The Trends in Thermoelectric Research

The correlations among the Seebeck coefficient α , electrical resistivity ρ and thermal conductivities κ make it difficult for one to refine only one or two of them in Eq.

1.9 without deteriorating the others. Such correlations are presented in Figure 1.4 and Eq. 1.14 ~ 1.16, that is, increasing σ , the numerator in Eq. 1.9, often leads to a decrease in α , which is another numerator, and leads to an increase in κ , the denominator. Compared with ρ and κ , however, α is relatively not as sensitive as the other two thermoelectric properties. Therefore, with emphasis on the reduction of the lattice thermal conductivity, G. A. Slack proposed the concept “phonon-glass electron-crystals” or PGEC, which means an ideal thermoelectric material should conduct heat as poorly as a glass but conduct electricity as good as a crystal.⁴

There are three general strategies to implement this concept.¹⁸ The first one is to take advantage of the disorder in the unit cell to scatter phonons that conduct heat. Such kinds of disorder can be produced by creating rattling structures or point defects such as interstitials, vacancies or by alloying.⁴ The filling of rare-earth atoms into the lattice voids in skutterudites is a successful example of the “rattling” concept on cage structure materials. A typical example of alloying is the long history of Bi_2Te_3 's alloying with other binary tellurides in order to reducing lattice thermal conductivity without sacrificing electrical conductivity.⁴⁷⁻⁵⁰

The second strategy is to construct complex crystal structures to separate the electron-crystal from the phonon-glass. Some complex structures may contain substructures that present a different preference for the transport of electrons and phonons. Zintl phase compounds are small-bandgap semiconductors with complex crystal structures that contained both ionically and covalently bonded atoms. Electrons are donated by ionic cations to covalently bound anionic species so that the charge-carrier

species would have higher mobility within the covalent bonding than the ionic bonding, leading to higher electrical conductivity in the covalent substructure and lower thermal conductivity in the ionic cation substructure. The ionic cation substructure can be further altered without disrupting the covalent substructure to fulfill the concept of the PGEC approach by means of doping and site disorders.⁴⁵

The third strategy is to scatter phonons at interfaces, leading to the use of multiphase composites mixed on the nanometer scale. As the particle size approaches the nanometer scale, the dimensionality decreases from conventional three-dimensional (3D) crystalline to two-dimensional (2D) quantum well to one-dimensional (1D) quantum wire and finally to zero-dimensional (0D) quantum dot, and the schematic change in electronic density of state (DOS) is shown in Figure 1.6.⁵¹ Figure 1.7 shows the bandgap of a Bi nanowire changes from that of a semimetal to a semiconductor as the nanowire diameter d_w decreases.⁵¹ Not only would nanoscale constituents introduce quantum-confinement effects to enhance the Seebeck coefficient, they also can introduce numerous interfaces that reduce thermal conductivity more than electrical conductivity because of the different scattering lengths of phonons and electrons. Figure 1.8 is a quantum-dot superlattice (QDSL) of composition PbTe/ PbSe_{0.98}Te_{0.02} on top of PbTe buffer layer deposited on BaF₂ substrate. An ordered array of PbSe quantum-dot structures exists between PbTe layers because of the lattice mismatch between PbTe and PbSe. A high ZT ~1.6 at 300 K was achieved in this QDSL.⁵²

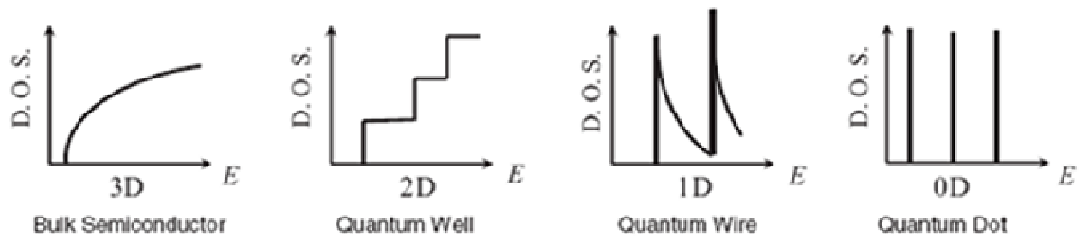


Figure 1.6 Electronic density of states (DOS) changes as the dimensionality is decreased from 3D bulk crystalline to 2D quantum well, to 1D quantum wire and 0D quantum dot.⁵¹

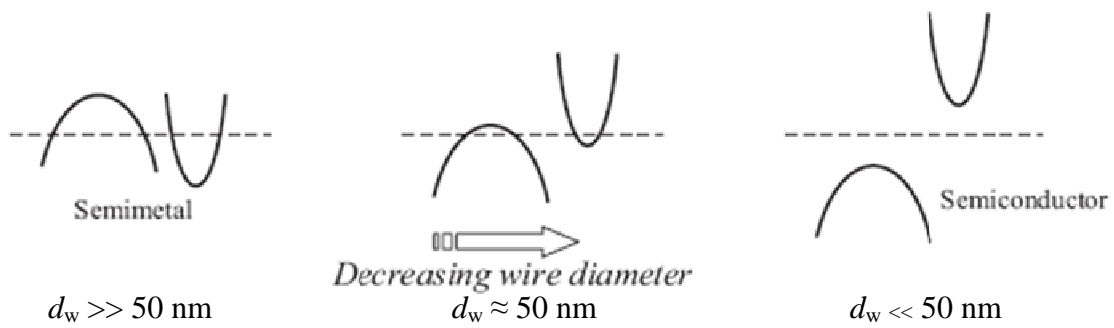


Figure 1.7 The schematic bandgap of Bi nanowire transition from semimetal to semiconductor as the diameter d_w of the nanowire is decreased.⁵¹

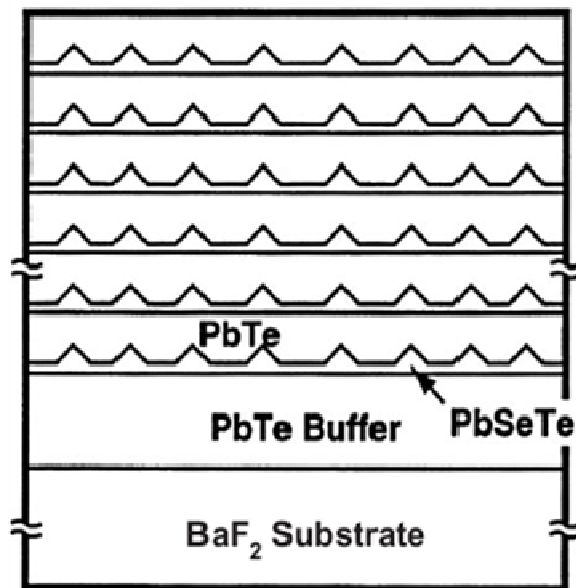


Figure 1.8 The schematic drawing of PbTe/ PbSe_{0.98}Te_{0.02} quantum-dot superlattice.⁵²

1.9 Thermoelectric Modules and Applications

The thermoelectric energy conversion concept is utilized in thermoelectric elements and modules. One p-type and one n-type thermoelectric material make two legs of a thermoelectric element for power generation or refrigeration shown in Figure 1.9 (a) and (b), respectively. The upper ends of such two legs are connected by metals so that they are electrically connected in series but thermally connected in parallel. For thermoelectric generation, the current I flows out from the p-leg, through the load and into the n-leg while heat is absorbed from the heat source on the top of the thermoelectric element and rejected heat sink at the bottom. For thermoelectric refrigeration, heat absorption occurs on the top and heat rejection occurs at the bottom when the current I flows in the direction shown in Figure 1.9 (b).

Note that the Seebeck coefficients of today's best thermoelectric materials are on the order of several hundreds of μV 's per Kelvin, thus a real thermoelectric module has to have a large number of thermoelectric elements in order to satisfy the requirement for a sufficient output voltage. Figure 1.9 (c) is an example of such a module for power generation.¹⁸ Tens of thermoelectric elements are electrically connected in series by the metal interconnects on top and bottom so that the output voltages of all the thermoelectric elements are summed up. They are then sandwiched between two electrically insulating substrates that have good thermal conductivity. All the elements are thus thermally connected in parallel. Such thermoelectric modules can be connected in series or in parallel to further increase the output voltage or current. Because of the very limited

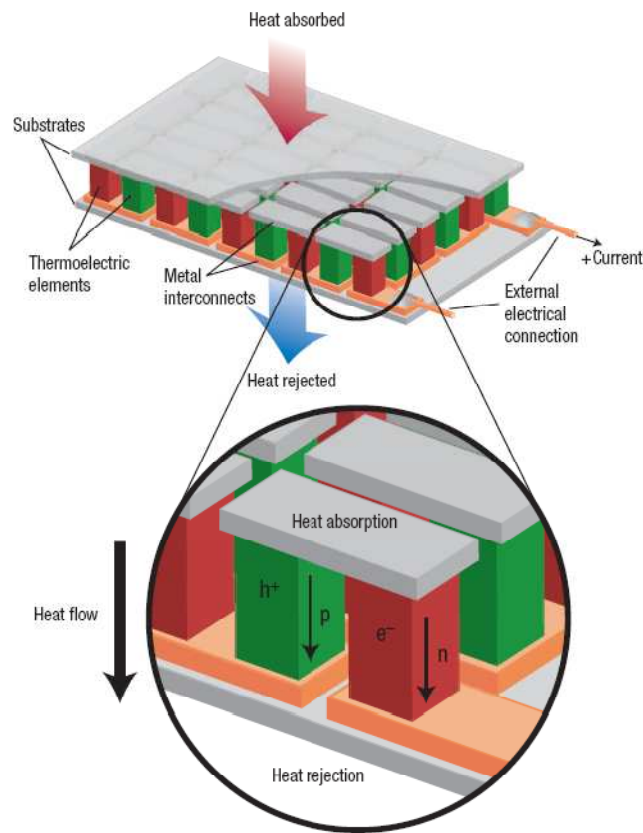
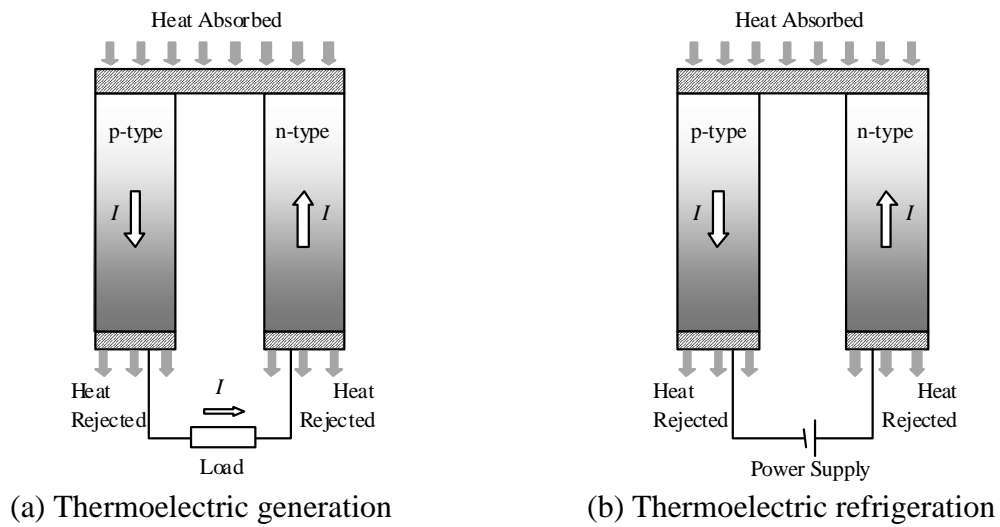


Figure 1.9 Thermoelectric elements made of p- and n-type legs: (a) power generation, (b) refrigeration, (c) a thermoelectric module consisting tens of such thermoelectric elements for power generation.

cooling ability of a single thermoelectric element, a similar configuration is adopted for thermoelectric modules in refrigeration applications.

Compared with other alternative energy conversion technologies such as nuclear power, hydroelectricity and fuel cells, thermoelectrics is advantageous for being compact, responsive and all solid-state without any moving part and hazardous working fluids. A bio-thermoelectric pacemaker driven by the temperature difference between the human body and its surroundings can be safely implanted into the human body and work for thirty maintenance-free years. However, the low efficiency of thermoelectrics has long constrained its applications mainly in niche applications where efficiency is less important than the energy availability and device reliability. For example, SiGe was employed in the NASA's radioisotope thermoelectric generators (RTGs) for deep-space missions beyond Mars, where the sunlight is unavailable.

The rising fossil oil price in the past decade has economically justified more applications of thermoelectrics in daily life. For example, the conversion of an automobile's waste heat, which accounts for about 2/3 of the power generated from combustion, from the exhaust or engine into electric energy using thermoelectric device has become worthwhile even at a relatively low conversion efficiency.³ Being the most sustainable and worldwide available energy source, solar energy also faces the problem of lowering the cost per unit power generated when competing with the fossil oil. The advantage of thermoelectric devices' easy tandem with other energy conversion approaches has helped developed solar thermoelectric energy conversion, in which the photovoltaic cells convert the energy of photons in the ultraviolet range (200 ~ 800 nm in

wavelength) of the solar spectrum while the thermoelectric devices cover the infrared range (800 ~ 3000 nm in wavelength).⁵³ Such solar-thermoelectric hybrid technology improves the conversion efficiency of solar energy into electricity and thus lowers the cost per unit power generated.

As to the application of another thermoelectric effect, the Peltier effect, the emerging market exists in the demand for solid-state refrigeration such as the cooling of CPU chips, infrared detectors and laser diodes.⁵⁴ The requirements for Small-scale and localized spot cooling are of first priority in such kind of application, and they are just what thermoelectric refrigeration features.

2. HYDROTHERMAL TREATMENT WITH SINGLE ALKALI METAL SALTS

2.1 Motivations

As in the concept of “Phonon-Glass Electron-Crystal” (PGEC) succinctly summarized by G. A. Slack,⁴ an ideal thermoelectric material should be endowed simultaneously with high Seebeck coefficient α , low electrical resistivity ρ and high thermal conductivity κ so that ZT defined in Eq. 1.9 can be maximized. Unfortunately, the correlations among these three thermoelectric properties determine that even the optimization of one of them often leads to deteriorations of the others, so that it is almost impossible for such an ideal PGEC thermoelectric material to exist in nature.

As mentioned in the previous chapter, in recent years there have been a variety of approaches or efforts to improve the performance of thermoelectric materials.⁵⁵⁻⁵⁸ One school of thought is that bulk materials should contain nanoscale constituents, or so-called “bulk-nano composite.”^{51, 59} In such composites the size effect and quantum confinement effect play an important role. For example, the nanocrystalline p-type BiSbTe bulk sample made by hot pressing nano-powders that were ball-milled from crystalline ingots was recently reported to have the ZT of ~ 1.4 ,⁶⁰ for which the improvement, compared with the $ZT \sim 1$ in the commercial ingot, resulted from the simultaneous reductions in both electrical resistivity and thermal conductivity. Another important school of thought is to decouple the otherwise inter-related quantities α , ρ and κ . For instance, in complex crystal systems composed of building modules with different

compositions, structural symmetries and thermoelectric functions, the electrical and thermal transports can be, to some extent, decoupled and tuned individually. The novel misfit-layered cobalt oxides and Zintl-phase compounds provide examples of such control.^{45,61-63}

Thus comes up the question whether the idea of “decoupling” can be somehow applied in the existing state-of-the-art thermoelectric materials such as Bi_2Te_3 , CoSb_3 and PbTe , etc. These polycrystalline samples are characterized by numerous grain boundaries. Although the grain boundary scattering of both heat-carrying phonons and electrons has proven effective in lowering the thermal conductivity, it also adversely decreases the electrical conductivity. Without considering a possible change in Seebeck coefficient, then whether or not the final ZT can be improved depends on the ratio of the gain in κ to the loss in σ . Therefore, it would be very crucial that there exists a thermoelectrically favorable grain boundary that scatters phonons more effectively than electrons so that ZT can eventually profit from more significant decreases in κ than in σ . So if such a thermoelectrically favorable grain boundary does exist, a novel approach called “grain boundary engineering” can be developed in order to improve the performance of polycrystalline thermoelectric materials by fabricating and controlling such grain boundaries.

Before proceeding, some attributes of this thermoelectrically favorable grain boundary can be speculated. The grains and the grain boundaries make the whole polycrystalline sample a composite. Within the framework of the effective medium approximation model⁶⁴, which is commonly used as a theoretical tool to analyze the

transport property of a composite, the ZT of a composite system can not exceed that of the best performing constituent of the composite, if there is no contribution from the interface/grain boundary^{64, 65}. Accordingly, it can be concluded that the thermally favorable grain boundary phase itself would be a better thermoelectric material than the grains if ZT of the polycrystalline sample is increased due to the existence of such a phase, and should be separated out for investigation. However, if the sample is a nanocomposite material that contains nanoscale constituents, or, in other word, nanoscale heterogeneity, the role of the interface becomes increasingly important with the diminishing characteristic length scale of one or more constituents and the interface effect can be a dominant factor given a typical value of 10^{19} particles and interfaces per cm^3 . Therefore, the contribution from the interface/grain boundary has to be taken into consideration, and the macroscopic composite approach should be restricted from the theoretical point of view. In a nanocomposite material, a PGEC system, if any, is achieved through the interface/boundary effect due to the introduction of nanoscale heterogeneity. Therefore, one can speculate that if this thermoelectrically favorable grain boundary does exist, it should be in nanoscale, making the polycrystalline bulk sample a nanocomposite material.

This chapter will present a proof-of-principle study of such a thermoelectrically favorable grain boundary in the polycrystalline p-type Bi_2Te_3 system via an alkali metal salt hydrothermal nano-coating treatment approach. Further applications of “grain-boundary engineering” to improve ZT and other thermoelectric properties will be discussed in following chapters.

2.2 Synthesis and Characterization

Figure 2.1 illustrates the procedure of sample synthesis procedure. A commercial p-type $\text{Bi}_{0.4}\text{Sb}_{1.6}\text{Te}_3$ ingot with a nominal composition $\text{Bi}_{0.4}\text{Sb}_{1.6}\text{Te}_3$ manufactured by Marlow Industries, Inc. was ground into powder and sifted into three categories in terms of particle size: $\leq 20 \mu\text{m}$, $20 \sim 32 \mu\text{m}$ and $32 \sim 45 \mu\text{m}$. About 2 grams of powders were loaded into a 45 ml capacity autoclave, mixed with 38 ml of alkali metal salt aqueous solution made by dissolving a mixture of 7.5 mmol $X\text{OH}$ and 2.5 mmol $X\text{BH}_4$, where $X = \text{Na}, \text{K}$ or Rb . The autoclave was sealed and heated at 150°C for 48 hours. The resultant products were washed thoroughly and dried under ambient conditions, followed by hot-pressing in a half inch die at 300°C and 200 MPa for 1 hour to form a pellet. In order to be concise and to distinguish the different material treatments, the samples treated by Na-salt-, K-salt- and Rb-salt-solutions are hereafter named as the Na-, K- and Rb-treated samples, respectively. A pellet directly hot pressed from untreated powders was named the Bulk Reference sample for comparison with the alkali salt treated samples.

Since both electrical and thermal conductivities are also dependent on porosity in polycrystalline samples, the densities of the as-pressed samples were measured by the Archimedes method and further confirmed by the gas pycnometry. All the densified pellets bear a very close packing density of $6.4 \pm 0.1 \text{ g/cm}^3$. The uniformity in density assures these samples were comparable with each other. All pellets were cut along the diameter direction into approximately $2 \times 2 \times 8 \text{ mm}^3$ bars for measurements of α , ρ and κ .

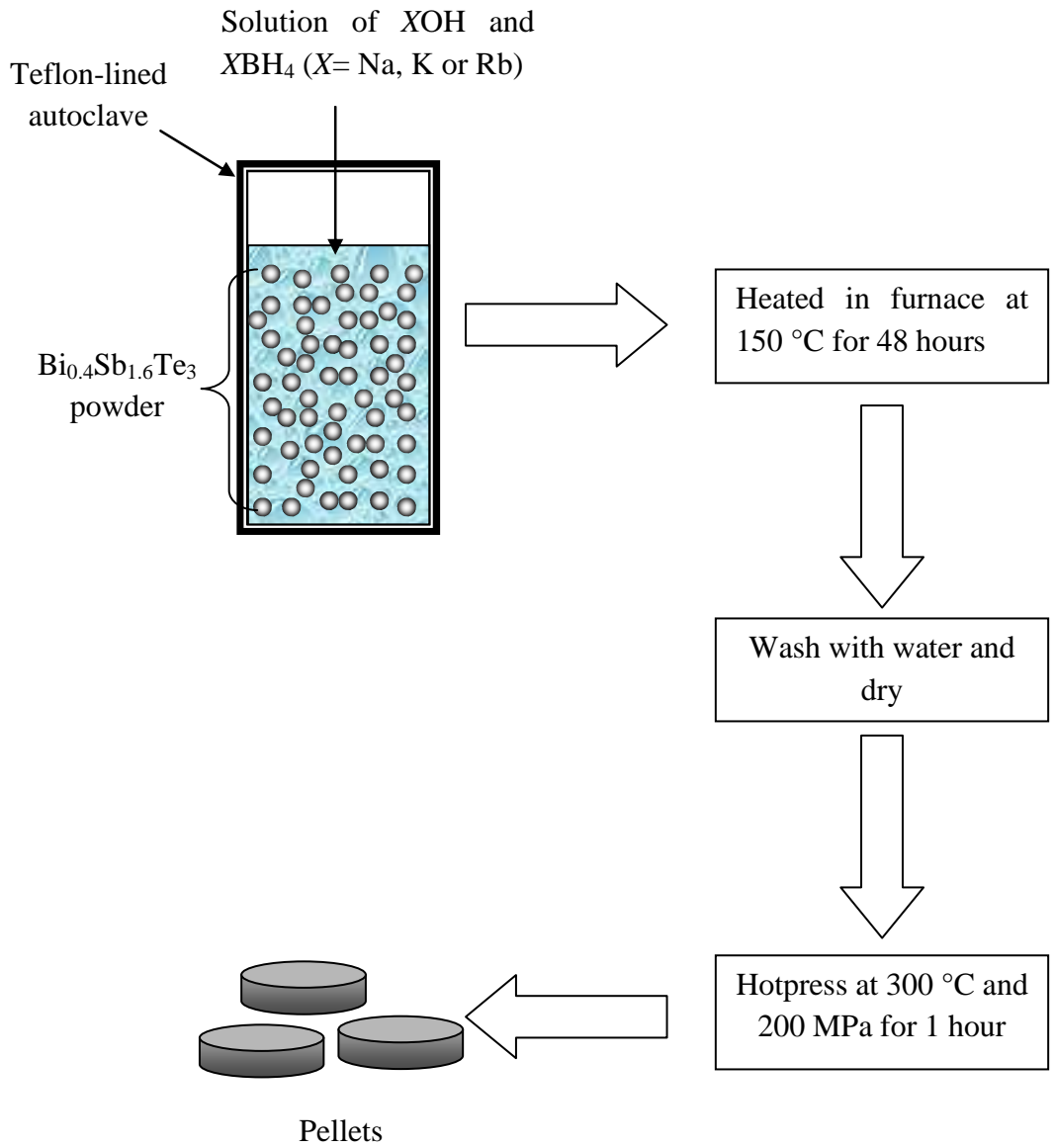


Figure 2.1 The diagram of p-type polycrystalline $\text{Bi}_{0.4}\text{Sb}_{1.6}\text{Te}_3$ sample preparation procedures.

α and ρ from 10 K up to room temperature were measured with a custom designed apparatus.⁶⁶ An Ulvac ZEM-2 high temperature system was used to measure α and ρ from 300 K to 450 K in a helium atmosphere.⁶⁷ κ from 10 K to room temperature was measured on a custom designed apparatus using a conventional four-probe steady state technique.⁶⁸ The high temperature κ from 300 K to 450 K was calculated from

$$\kappa = dDC_v \quad (2.1)$$

where d is the sample's density, D , the thermal diffusivity and C_v , the constant volume specific heat.

D was measured with a Netzsch LFA 457 laser flash⁶⁹ using the transient method from room temperature to 450 K, and C_v was measured on a Netzsch differential scanning calorimetry (DSC) 404 Pegasus⁷⁰ by assuming $C_v \approx C_p$ for solids⁷¹, where C_p is the constant pressure specific heat. The Bi_2Te_3 ingot is anisotropic in thermoelectric properties.⁷²⁻⁷⁴ The hot-pressed polycrystalline samples exhibited anisotropy, as shown in Figure 2.2, between the high temperature thermal diffusivity data measured parallel and perpendicular to the diameter of the pellet. Such anisotropy resulted from the texture formed when p- $\text{Bi}_{0.4}\text{Sb}_{1.6}\text{Te}_3$ powders were hot-pressed into pellet.⁷⁵⁻⁷⁷ Since α and ρ of high temperature (≥ 300 K) were all measured along the diameter of the pellet and the measurement of high temperature D , however, was performed in the direction perpendicular to the pellet, the pellet must, as shown in Figure 2.3, be cut into bars, turned 90°, then realigned to form a new pellet with J-B Weld that could be found in any hardware store.⁷⁸ Based on the D measured after such realignment, the high temperature κ

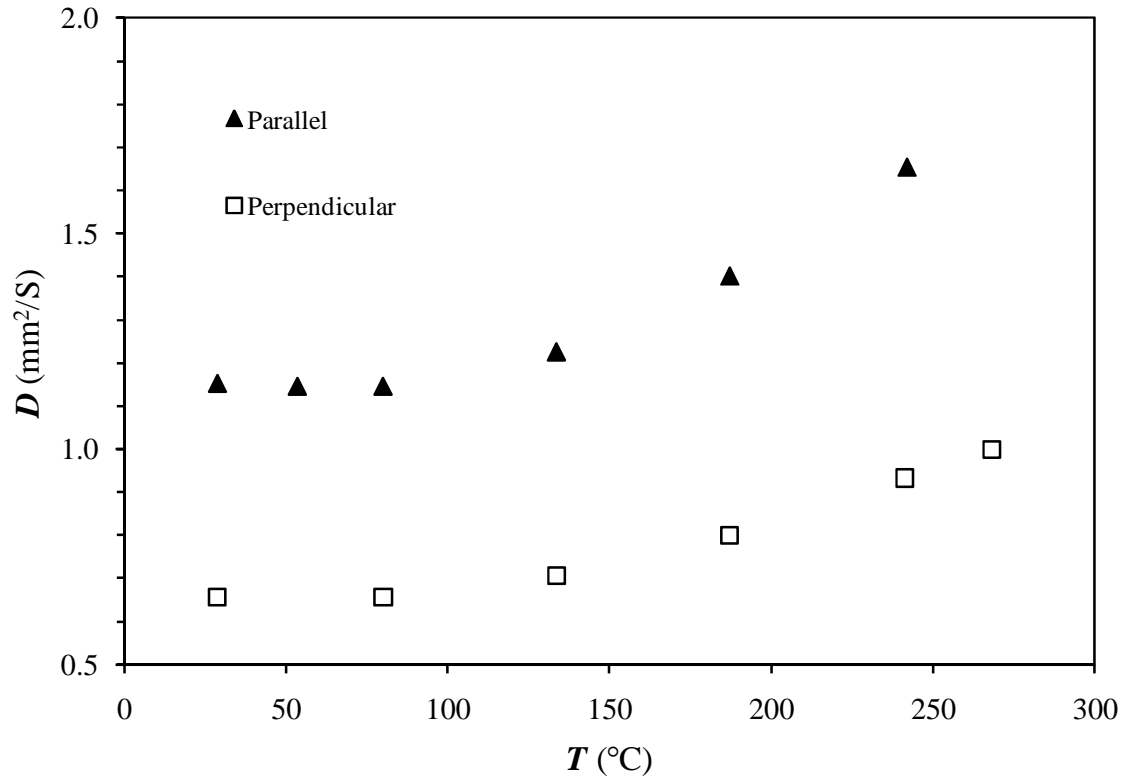
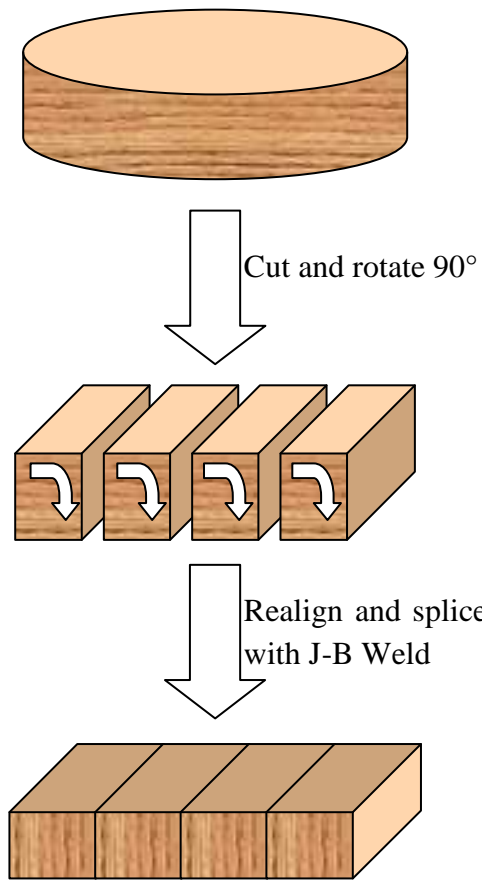
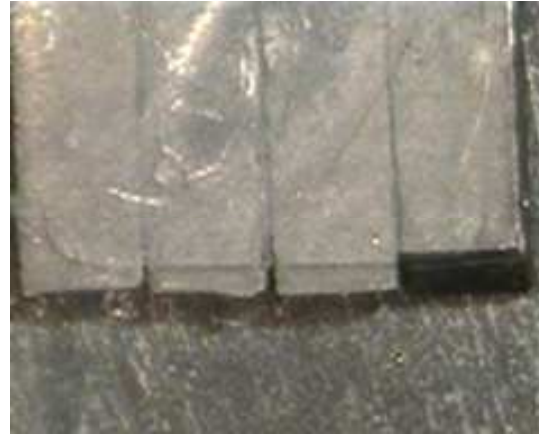


Figure 2.2 The anisotropy of thermal diffusivity D of p-type $\text{Bi}_{0.4}\text{Sb}_{1.6}\text{Te}_3$ pellet due to the texture formed during hot-press. D measured parallel to the diameter direction of the pellet is higher than perpendicular to the diameter direction.



(a)



(b)

Figure 2.3 (a) The diagram of realignment of p-type $\text{Bi}_{0.4}\text{Sb}_{1.6}\text{Te}_3$ bars cut from the pellet and (b) actual pictures of such realigned bars.

calculated from Eq. 2.1 was in the same direction as α and ρ were measured, ensuring ZT was correctly deduced from Eq. 1.9.

Room temperature Hall coefficient R_H measurements were performed on a Quantum Design PPMS (Physical Properties Measurement System)⁷⁹ using a 5-wire configuration with magnetic field sweeping between ± 1 Tesla. The Hall mobility μ_H and carrier concentration n were subsequently calculated from the equations:

$$\mu_H = \frac{R_H}{\rho} \quad (2.2)$$

and

$$n = -\frac{1}{eR_H} \quad (2.3)$$

respectively, where ρ is the electrical resistivity and e is the electron charge.

2.3 The Effects of Particle Size on Thermoelectric Properties

It is taken for granted that besides the treatment method, the particle size would have an influence on the sample's thermoelectric properties because the smaller the particle size, the larger the number of grain boundaries there could be in the hot-pressed sample. In order to verify this hypothesis, the thermoelectric properties were measured on three pellets that were hydrothermally treated with the same Na salt recipe but prepared from powders of different particle sizes, 32 ~ 45 μm , 20 ~ 32 μm and ≤ 20 μm , respectively, and the results are shown in Figures 2.4 ~ 2.7.

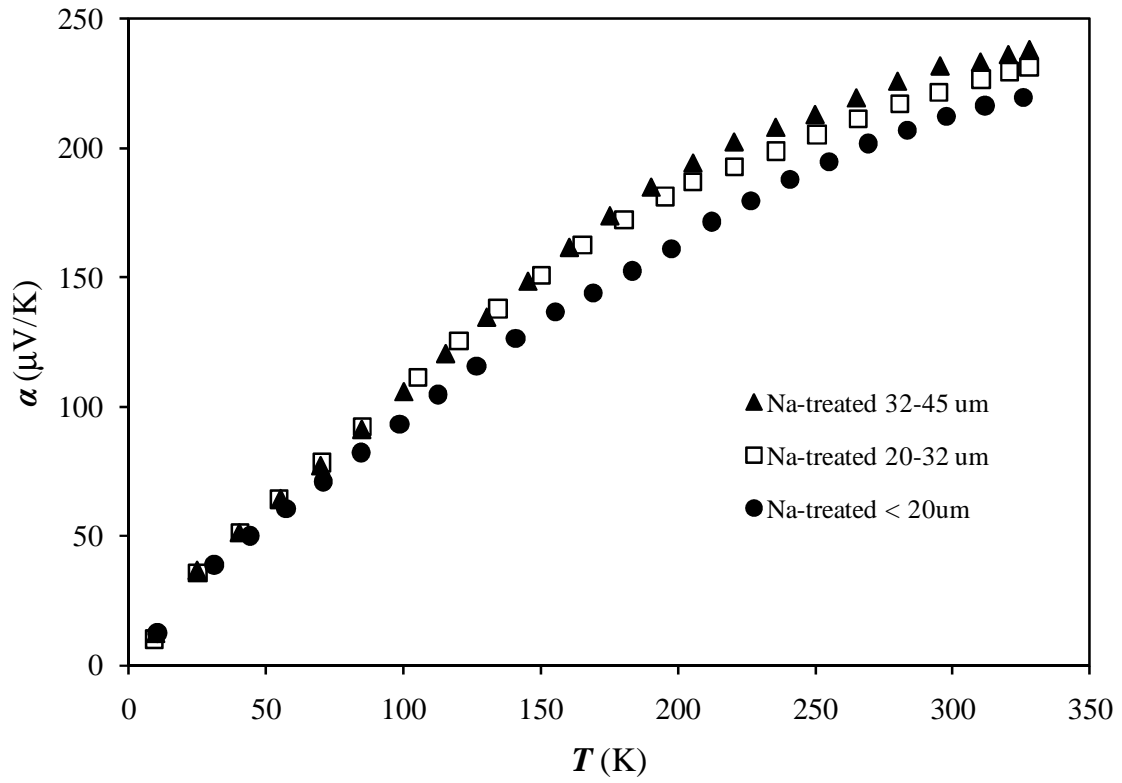


Figure 2.4 The Seebeck coefficient α as a function of temperature T for hydrothermally Na-treated p-type $\text{Bi}_{0.4}\text{Sb}_{1.6}\text{Te}_3$ polycrystalline samples prepared with powder of particle sizes $<20 \mu\text{m}$, $20 \sim 32 \mu\text{m}$ and $32 \sim 45 \mu\text{m}$, respectively.

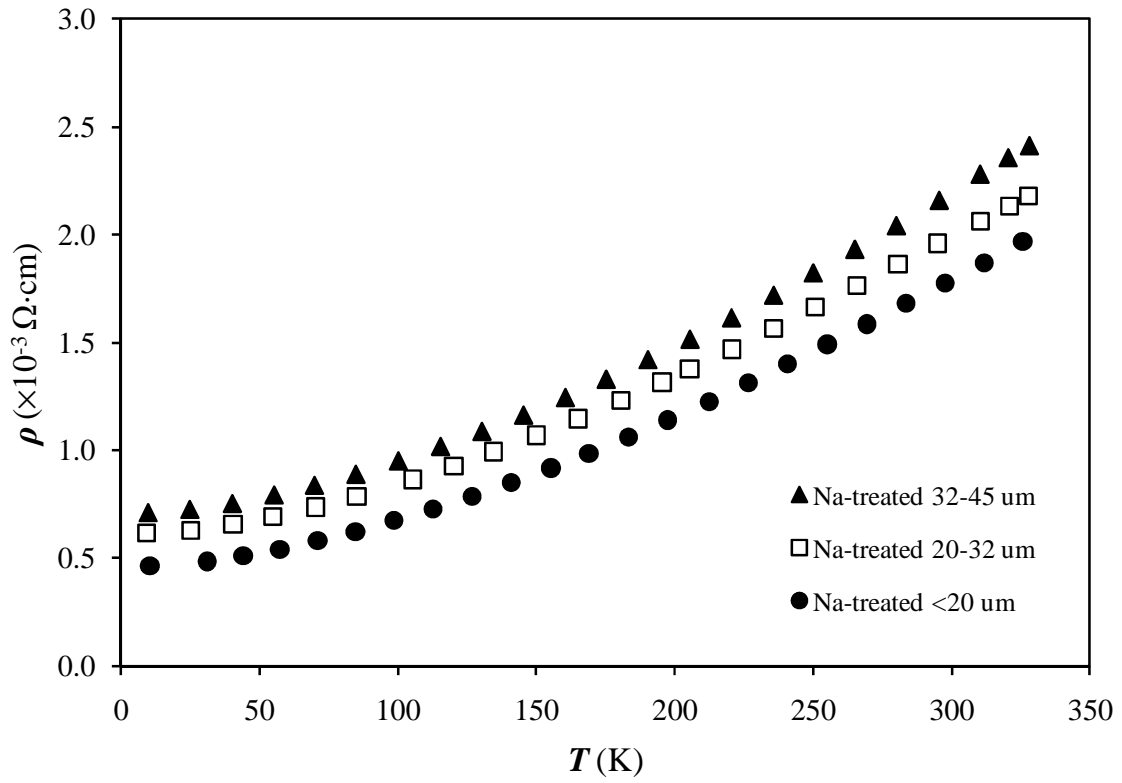


Figure 2.5 The electrical resistivity ρ as a function of temperature T for hydrothermally Na-treated p-type $\text{Bi}_{0.4}\text{Sb}_{1.6}\text{Te}_3$ polycrystalline samples prepared with powder of particle sizes $<20 \mu\text{m}$, $20 \sim 32 \mu\text{m}$ and $32 \sim 45 \mu\text{m}$, respectively.

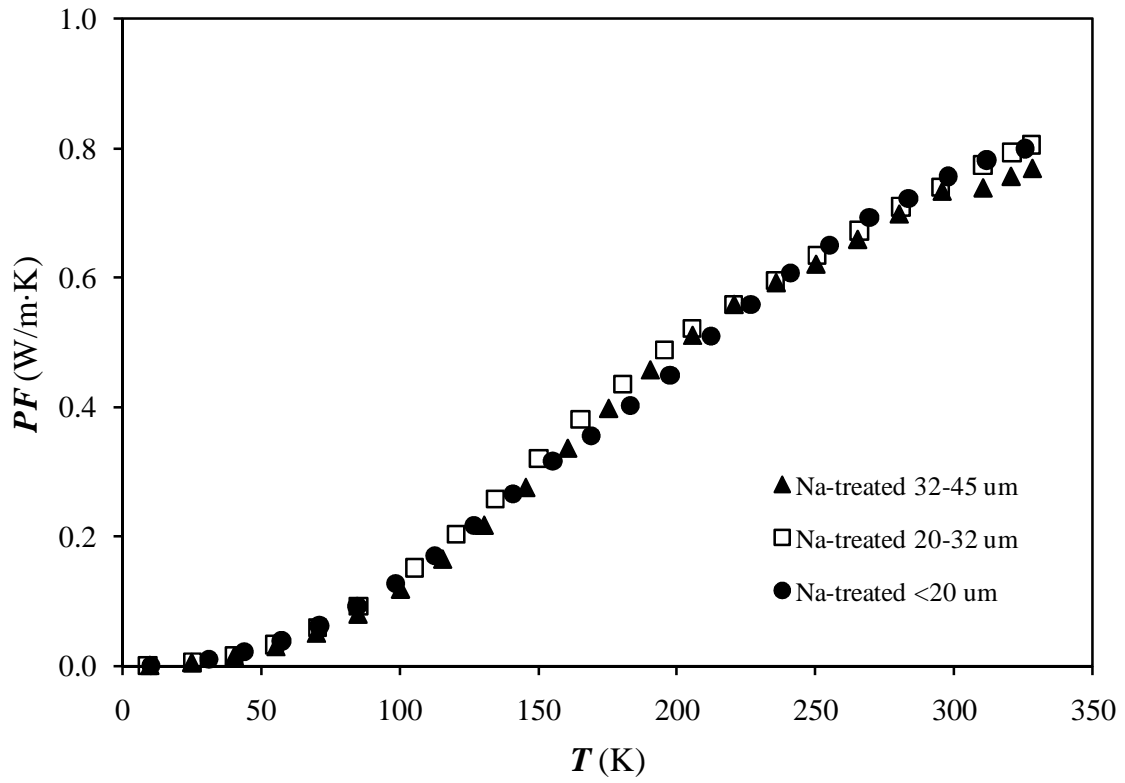


Figure 2.6 The power factor PF as a function of temperature T for hydrothermally Na-treated p-type $\text{Bi}_{0.4}\text{Sb}_{1.6}\text{Te}_3$ polycrystalline samples prepared with powder of particle sizes $<20 \mu\text{m}$, $20 \sim 32 \mu\text{m}$ and $32 \sim 45 \mu\text{m}$, respectively.

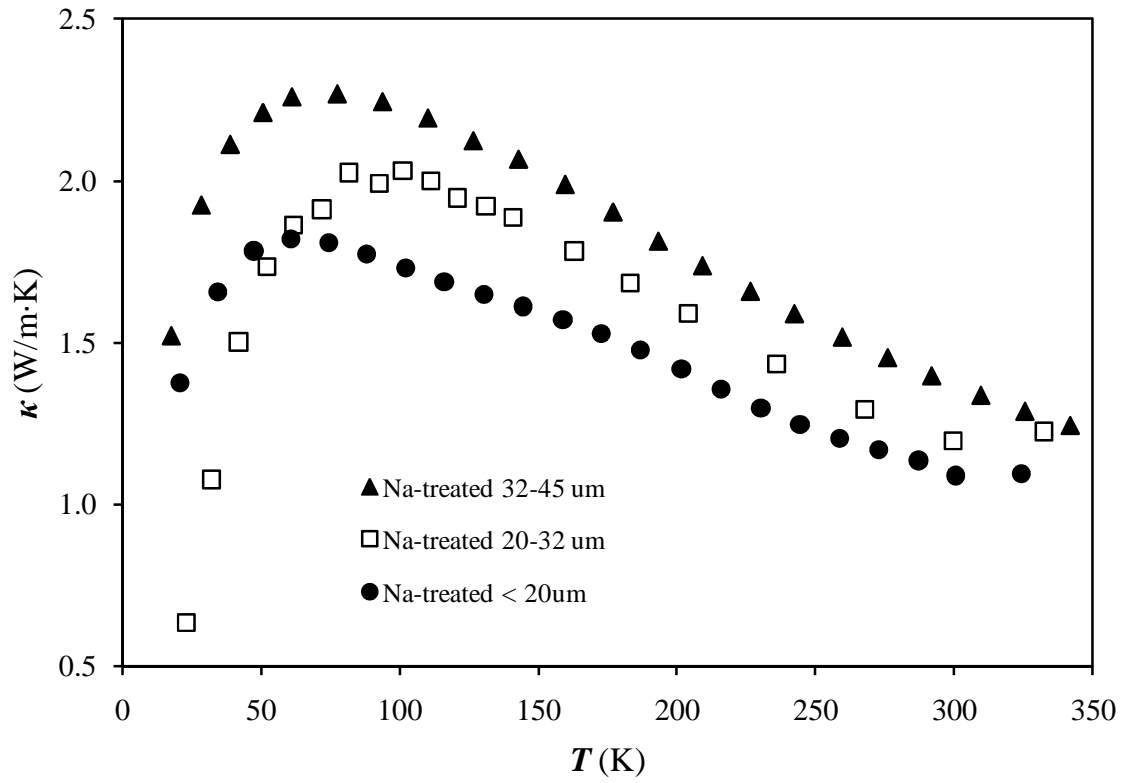


Figure 2.7 The thermal conductivity κ as a function of temperature T for hydrothermally Na-treated p-type $\text{Bi}_{0.4}\text{Sb}_{1.6}\text{Te}_3$ polycrystalline samples prepared with powder of particle sizes $<20 \mu\text{m}$, $20 \sim 32 \mu\text{m}$ and $32 \sim 45 \mu\text{m}$, respectively.

The differences between the three pellets in Figure 2.4 are small, but a result is that a larger particle size results in a slightly greater Seebeck coefficient. However, the electrical resistivity curves shown in Figure 2.5 demonstrate an opposite tendency, in which a smaller particle size leads to a smaller resistivity. Although the scattering of electrons on grain boundaries have negative influences on ρ , the increase in the number of grain boundaries in the sample of smaller particle size does not deteriorate, but improves ρ . An explanation to this seemingly abnormal phenomenon will be given later in Chapter 5. The curves of PF of three specimens are nearly on top of each other in Figure 2.6, implying that the positive and negative effects of large particle size on α and ρ are cancelling each other. Looking back at Figures 2.4 and 2.5, one may notice that particle size causes bigger differences in ρ than in α . It is reasonable because ρ is largely correlated with grain boundary scattering while α is dependent on the material's band structure and composition which are not so subject to the treatment as is ρ .

The fact that a larger particle size causes a higher κ as demonstrated in Figure 2.7 shows that the grain boundary scattering is a determinant factor for κ . Finally, the pellet made of the powers $\leq 20 \mu\text{m}$, i.e., the smallest particle size, has the highest ZT in Figure 2.9. This verifies that not only whether but also how the number of grain boundaries due to different particle sizes affects the sample's thermoelectric performance. The results from K-treated and Rb-treated samples also show a decreased particle size leads to an increased ZT although, to keep the dissertation more succinct, the data are not herein included.

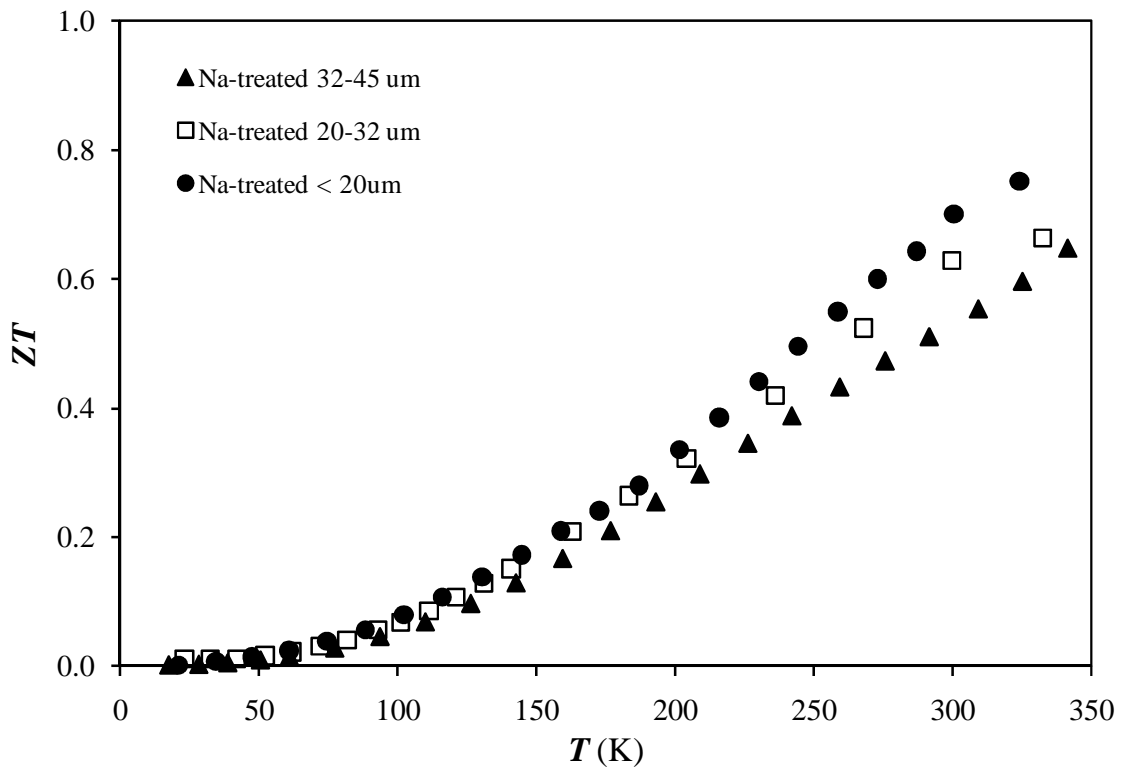


Figure 2.8 The dimensionless figure of merit ZT as a function of temperature T for hydrothermally Na-treated p-type $\text{Bi}_{0.4}\text{Sb}_{1.6}\text{Te}_3$ polycrystalline samples prepared with powder of particle sizes $<20 \mu\text{m}$, $20 \sim 32 \mu\text{m}$ and $32 \sim 45 \mu\text{m}$, respectively.

With the relationship between ZT and particle size established, samples prepared from powders $\leq 20 \mu\text{m}$ (635 mesh) were chosen to be the main focus of research and thus received most extensive investigations mainly because they provide the most grain boundaries and have the highest ZT , while samples of other two particle sizes were also investigated.

2.4 Effects of Different Alkali Metal Salts⁸⁰

Figures 2.9 ~ 2.11 present α , ρ and PF from 10 K to 450 K of as-treated and untreated samples prepared with $\leq 20 \mu\text{m}$ powders but treated with Rb, K and Na salts, respectively. Shown in Figure 2.10, the increase in the Seebeck coefficient for the Rb-treated sample is appreciable yet small while compared with the other three samples, which have almost exactly the same value in α at each temperature whether they were hydrothermally treated or not. This is an encouraging result since the present hydrothermal treatment not only preserved α but also, in some cases (Rb treated), increased α , which, as compared with ρ and κ , is the most robust parameter to tune. To check if the increase of the Seebeck coefficient is at the expense of an increase in the electrical resistivity, the electrical resistivity ρ as a function of temperature T before and after hydrothermal treatment is plotted in Figure 2.10, which shows another inspiring result that all the hydrothermally treated samples exhibits a slightly lower electrical resistivity than the Bulk Reference, with the K- and Rb- treated samples having the lowest ρ .

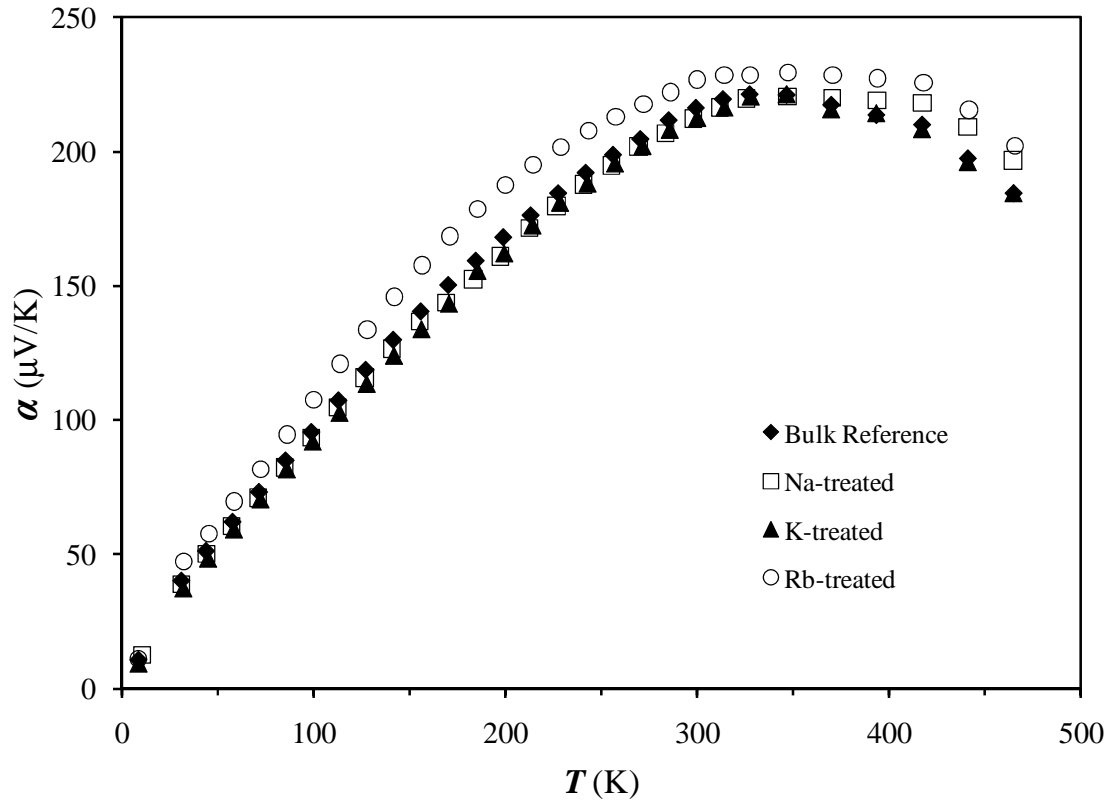


Figure 2.9 The Seebeck coefficient α as a function of temperature T for p-type $\text{Bi}_{0.4}\text{Sb}_{1.6}\text{Te}_3$ polycrystalline samples hydrothermally treated with Na, K and Rb metal salts, respectively, and untreated Bulk Reference, all of which are prepared with powder of particle size $<20 \mu\text{m}$.

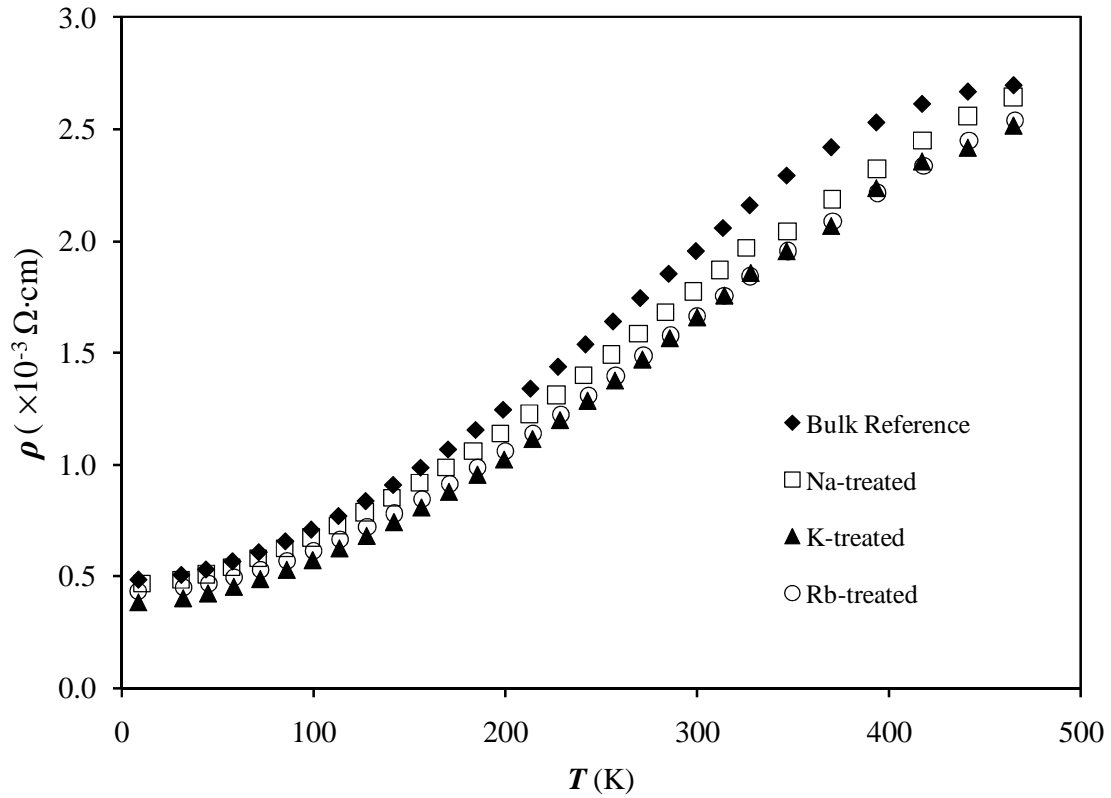


Figure 2.10 The electrical resistivity ρ as a function of temperature T for p-type $\text{Bi}_{0.4}\text{Sb}_{1.6}\text{Te}_3$ polycrystalline samples hydrothermally treated with Na, K and Rb salts, respectively, and untreated Bulk Reference, all of which are prepared with powder of particle size $<20 \mu\text{m}$.

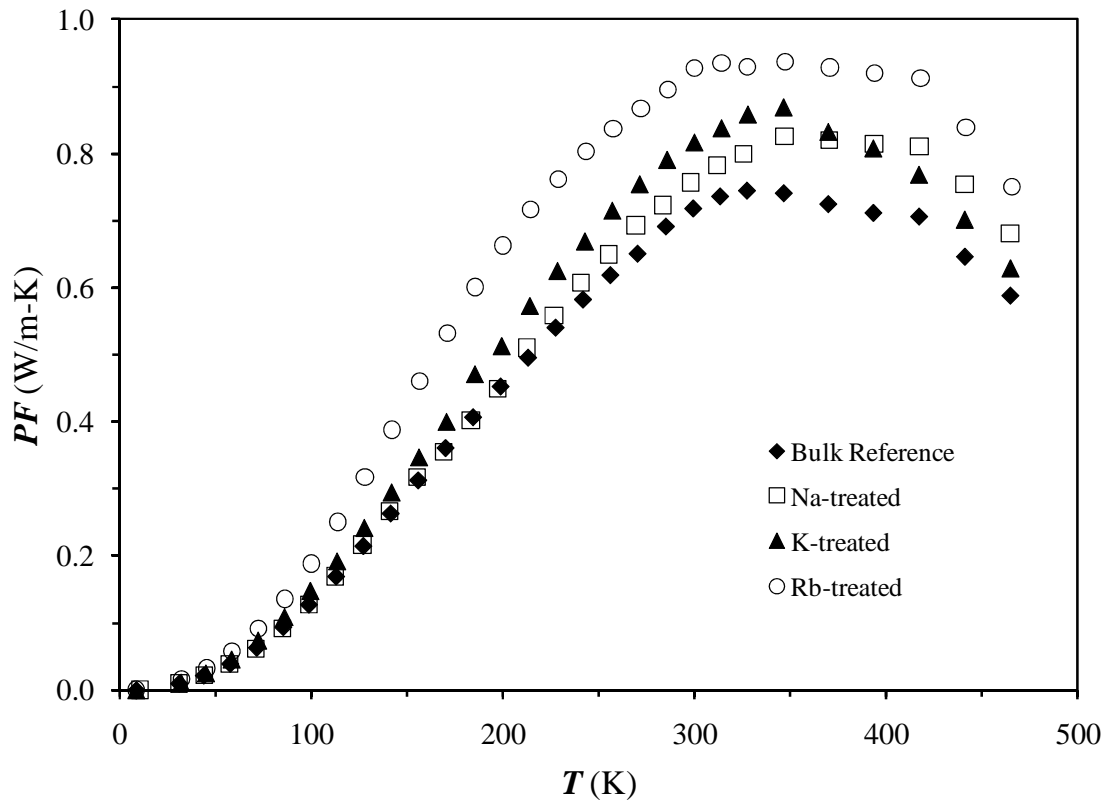


Figure 2.11 The power factor PF as a function of temperature T for p-type $\text{Bi}_{0.4}\text{Sb}_{1.6}\text{Te}_3$ polycrystalline samples hydrothermally treated with Na, K and Rb salts, respectively, and untreated Bulk Reference, all of which are prepared with powder of particle size $<20 \mu\text{m}$.

Derived from Eq. 1.9, the PF is undoubtedly increased for all three treated samples as compared with the Bulk Reference in Figure 2.11, for both α and ρ are improved or at least retained after hydrothermal treatment of alkali metal salt. Since the Rb-treatment simultaneously increases α and decreased ρ the most, the improvement in the PF is the greatest for the Rb-treated sample. The PF 's of the K- and the Na- treated samples were improved solely due to the decrease in ρ because neither the K- nor the Na-treatment has positive effects on α .

Above mentioned results have so far led to an optimistic conclusion that all hydrothermal treatments with different alkali metal salts would improve the PF , a quantity characterizing a thermoelectric material's electrical properties while κ is a measure of the thermal transport properties. The dimensionless figure of merit ZT is simply the ratio of the PF to κ . Thus, the final increase in the ZT relies on either an increase in the PF or a decrease in κ , or both. However, it has been found many times that it is a tradeoff that the increase in the PF is often negated, or, which is even worse, exceeded by the increase in thermal conductivity.

This concern is suppressed by the thermal conductivity vs. temperature data in Figure 2.12, which makes the expectation come true that the PF is improved without sacrificing κ . On the contrary, all three treated samples have lower κ values than the Bulk Reference. Na-treatment achieves the best result causing the thermal conductivity to be approximately 15% lower than the Bulk Reference at 300 K, the typical operating temperature for commercial Bi_2Te_3 . The Na-treated sample exhibits an overall lower κ than the K-treatment although the difference becomes marginal above 200 K until they

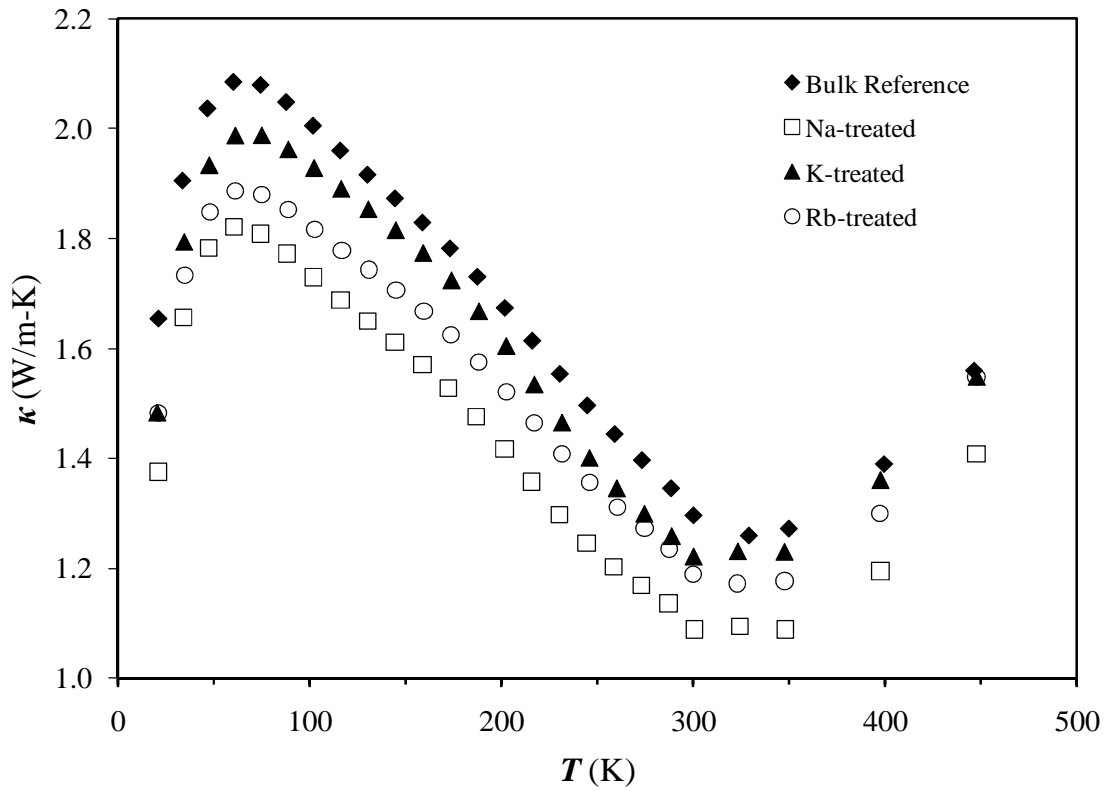


Figure 2.12 The thermal conductivity κ as a function of temperature T for p-type $\text{Bi}_{0.4}\text{Sb}_{1.6}\text{Te}_3$ polycrystalline samples hydrothermally treated with Na, K and Rb salts, respectively, and untreated Bulk Reference, all of which are prepared with powder of particle size $<20 \mu\text{m}$.

almost overlap around and above 300 K. However, the thermal conductivities of the treated samples are significantly lower than that of the Bulk Reference by as much as about 20% at $T = 350\text{K}$. The lattice thermal conductivity κ_L calculated using Eq. 1.14 ~ 1.16 as a function of temperature T is displayed in Figure 2.13. Once again, the Bulk Reference has the highest κ_L , and the Na-treated sample showed the lowest κ_L while those of the K- and Rb-treated samples are close to each other.

With all thermoelectric properties measured, ZT curves from 10 K to 450 K for all samples are deduced and plotted in Figure 2.14. The Rb-treated sample has the highest ZT of ~ 0.8 at 323 K followed by Na- and K- treated ones. To analyze the different ways in which these three hydrothermal treatments with different alkali metal salts enhanced ZT , the values of the thermal conductivity κ , the lattice thermal conductivity κ_L , the power factor α^2/ρ and the dimensionless figure of merit ZT at 323 K of these three treated samples are normalized with respect to those of the Bulk Reference and then plotted in Figure 2.15. Therefore, it is concluded that Rb-treatment mainly affects the power factor (both the Seebeck coefficient and the electrical resistivity) to improve ZT while Na-treatment aims at thermal conductivity.

To help elucidate the observed changes in the electrical resistivity and the Seebeck coefficient, Hall coefficient measurements were performed on all the samples at 310 K. The calculated carrier concentration and Hall mobility data are listed in Table 2.1. It is found that all four samples, regardless of treatment or not, have very close mobility values at the measured temperature, whereas the carrier concentrations of all three

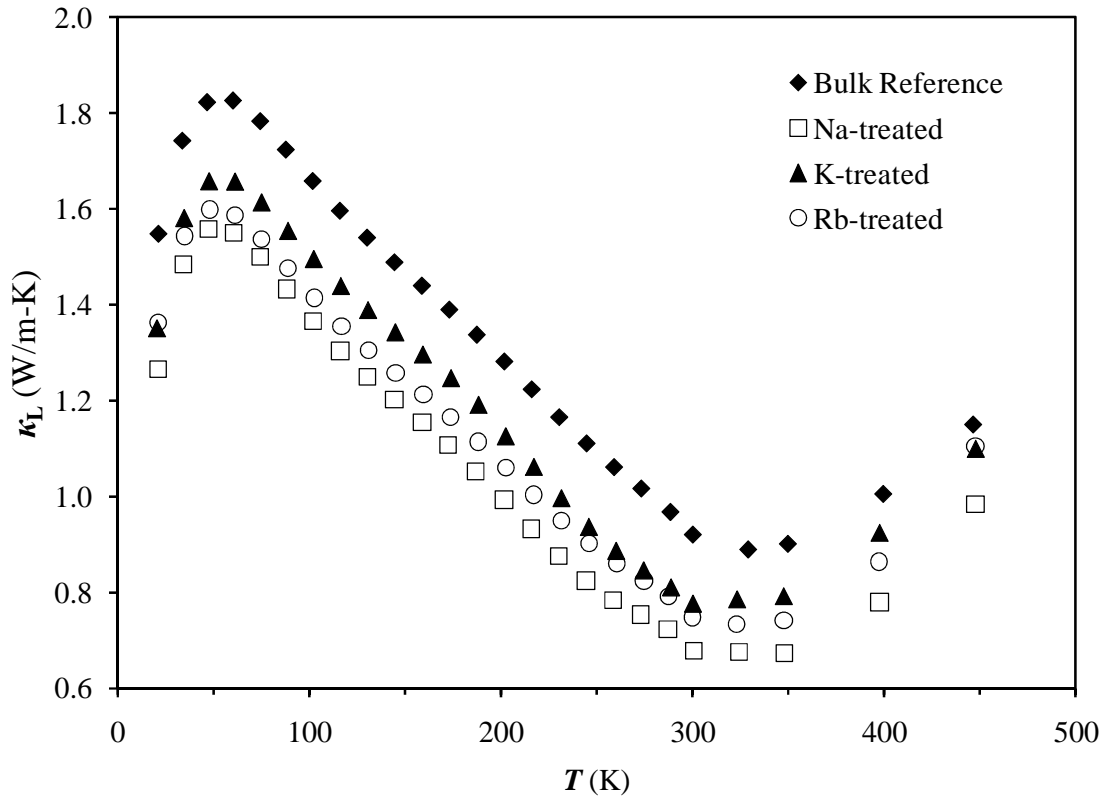


Figure 2.13 The lattice thermal conductivity κ_L as a function of temperature T for p-type $\text{Bi}_{0.4}\text{Sb}_{1.6}\text{Te}_3$ polycrystalline samples hydrothermally treated with Na, K and Rb salts, respectively, and untreated Bulk Reference, all of which are prepared with powder of particle size $<20 \mu\text{m}$.

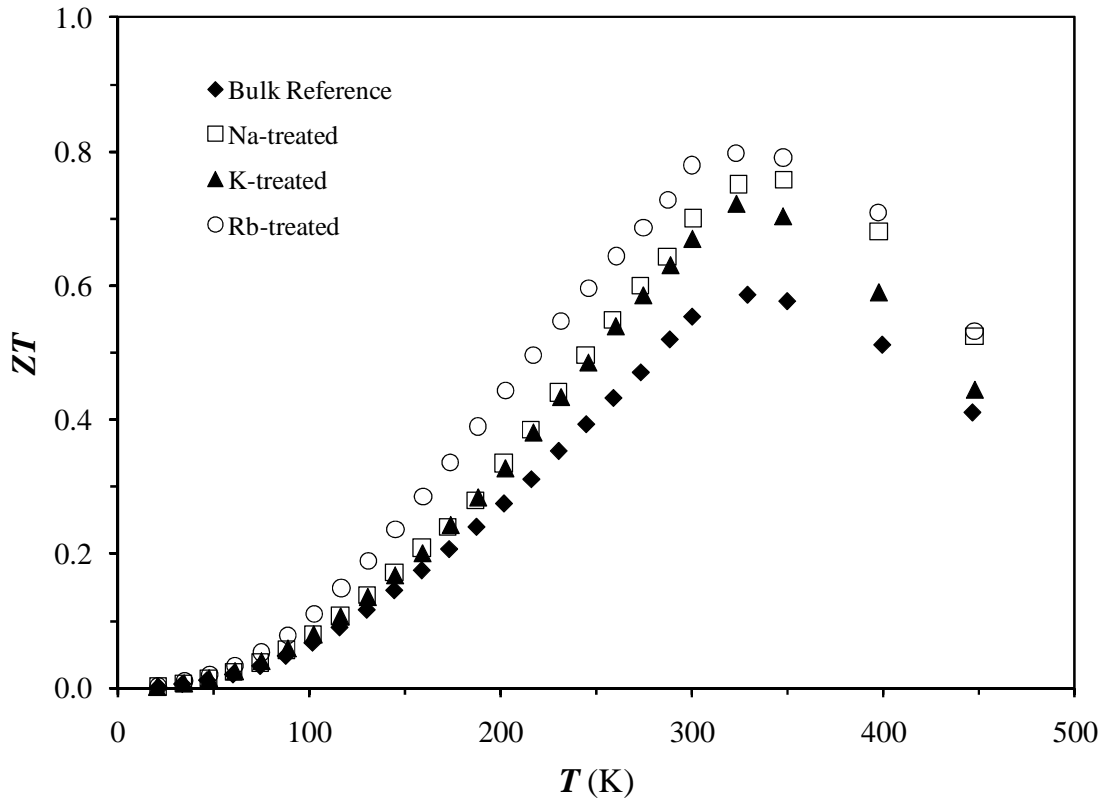


Figure 2.14 The dimensionless figure of merit ZT as a function of temperature T for p-type $\text{Bi}_{0.4}\text{Sb}_{1.6}\text{Te}_3$ polycrystalline samples hydrothermally treated with Na, K and Rb salts, respectively, and untreated Bulk Reference, all of which are prepared with powder of particle size $<20\ \mu\text{m}$.

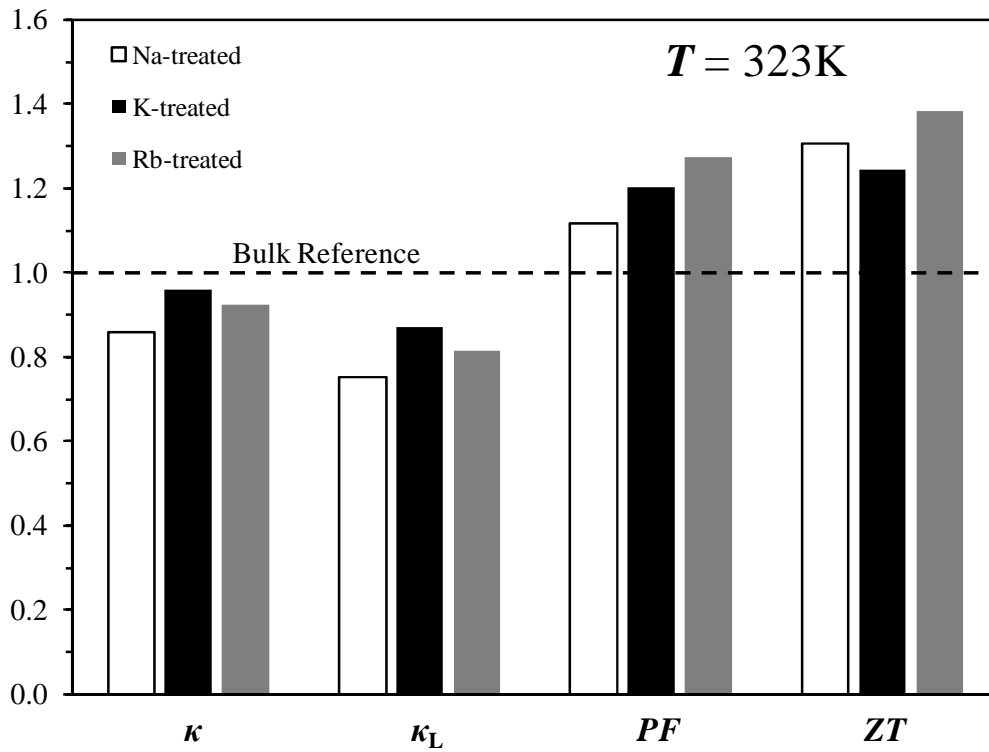


Figure 2.15 Itemized contributions at temperature $T = 323\text{K}$ from the thermal conductivity κ , the lattice thermal conductivity κ_L and the power factor PF to the enhancements in the dimensionless figure of merit ZT of p-type $\text{Bi}_{0.4}\text{Sb}_{1.6}\text{Te}_3$ polycrystalline samples hydrothermally treated with Na, K and Rb salts, respectively, all of which are prepared with powder of particle size $<20\ \mu\text{m}$. Such contributions are normalized with respect to the untreated Bulk Reference.

hydrothermally treated samples were appreciably higher than that of the Bulk Reference. This implies that the current alkali metal hydrothermal treatment introduced extra charge carriers into the system. As shown clearly from the data in Table 2.1, the introduction of extra carriers into the system does not deteriorate the Seebeck coefficient. Since the Seebeck coefficient value is proportional to the effective mass m^* and/or inversely proportional to the carrier concentration n , one possible explanation here is that the new charge carriers have relatively large effective mass. Therefore the inter-related electrical resistivity and Seebeck coefficient are decoupled.

Table 2.1 The electrical transport properties at 310K of p-type $\text{Bi}_{0.4}\text{Sb}_{1.6}\text{Te}_3$ polycrystalline samples. They are hydrothermally treated with Na, K and Rb salts, respectively, and untreated Bulk Reference. All samples are synthesized with powder <20 μm .

	n ($\times 10^{19} \text{ cm}^{-3}$)	μ_{H} ($\text{m}^2/\text{V}\cdot\text{s}$)	α ($\mu\text{V}/\text{K}$)	ρ ($\times 10^{-3} \Omega\cdot\text{cm}$)
Bulk Reference	2.05	0.015	219	2.03
Na-treated	2.25	0.015	217	1.86
K-treated	2.26	0.016	215	1.73
Rb-treated	2.26	0.016	228	1.73

2.5 Conclusion

Compared with untreated Bulk Reference, the effects of alkali metal salt hydrothermal treatments on the thermoelectric properties were distinct as follows:

1. All hydrothermal treatments barely touched α , but lower ρ , κ and κ_L .
2. Therefore, both PF and ZT were improved in all treated samples.
3. Na-treatment reduced κ and κ_L the most ($\approx 20\%$).
4. The Rb-treatment lowered ρ the most and slightly increased α . Therefore, it resulted in the highest PF .
5. The improvements caused by K-treatment in κ and PF were not as significant as Na- and Rb-treatments, respectively.

It has also been shown that such effects caused by hydrothermal treatments became more and more pronounced as the particle size of the sample decreases. Therefore, the highest ZT was achieved in the sample prepared by powder $< 20 \mu\text{m}$.

3. SURFACE LAYER ON THE GRAIN BOUNDARY AFTER THE HYDROTHERMAL TREATMENT

3.1 Introduction

The preliminary study on the hydrothermal treatment with different alkali metal salts has proven that this approach is capable of decoupling to some extent the otherwise interrelated three thermoelectric properties, α , ρ and κ , of p-type Bi_2Te_3 alloys. Following the discovery of the phenomena, in-depth investigations should be conducted to unveil what happened after the hydrothermal treatment, and such investigations would be very instructive to follow-up research not only on p-type Bi_2Te_3 system but also possibly on other thermoelectric materials.

X-ray Diffraction (XRD) and Scanning Electron Microscopy (SEM) are two common approaches that are used to investigate samples in the micrometer and nanometer range. The XRD was performed on a Scintag 2000 X-ray diffractometer, and the SEM was performed on a Hitachi H7600T electron microscope with options of Transmission Electron Microscopy (TEM) and Selected Area Electron Diffraction (SAED), and was also performed on a Hitachi HD2000 electron microscope for Element Mapping Energy Dispersive Spectroscopy (EDS) with the Oxford INCA Energy 200 EDS detector.

In addition to these two traditional methods, several other analyses were performed in efforts to ascertain the changes, either structural or compositional, caused by alkali metal salt hydrothermal treatment. Therefore, thermogravimetry analysis (TGA)

was performed on a TA SDT-2960 Instrument, and Raman and Fourier transform infrared (FTIR) absorption spectroscopy measurements were also carried out.

3.2 Composition of Surface Layers

The comparison in appearance of $\text{Bi}_{0.4}\text{Sb}_{1.6}\text{Te}_3$ powder before and after hydrothermal treatment is demonstrated in Figures 3.1 (a) ~ (d) that are taken with FESEM (Field Emission Scanning Electron Microscopy). Before the treatment, the boundaries among the grains are clear and sharp under the electron microscope, as shown in Figure 3.1 (a). After the treatment, it shows in Figure 3.1 (b), which is in the same scale as the former, that the surfaces of the grains are not as clean as before so that the boundaries become unclear. In Figures 3.1 (c) and (d) that are in smaller scales, a fluffy surface of the particle is present.

On a hydrothermally Na-treated p- $\text{Bi}_{0.4}\text{Sb}_{1.6}\text{Te}_3$ commercial ingot from Marlow Industries, a thin surface of approximately 2 μm is found with SEM as shown in Figures 3.2 (a) and (b). The SEM image in Figure 3.2 (a) was obtained in backscattering mode, which renders light colors for areas where there are light elements and dark colors for heavy elements. Thus, the contrast in color between the surface layer and the body of the ingot implies the surface layer is comprised of light elements, which are very likely the resultants of reaction from the hydrothermal treatment.

The EDS analysis in the selected area in the surface layer in Figure 3.3 shows in the table that a small amount of Na exists in the surface layer in addition to Bi, Sb and Te,

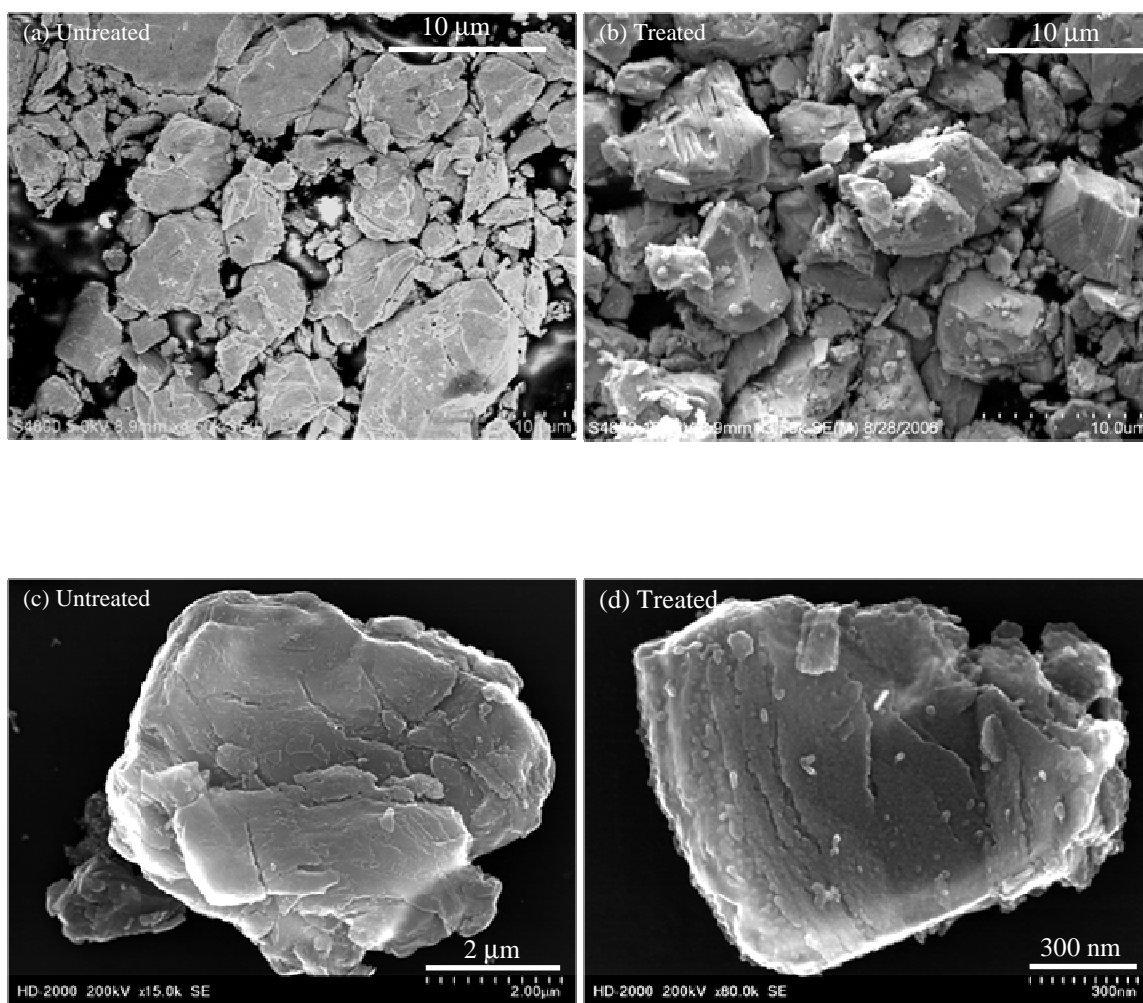


Figure 3.1 The FESEM pictures of p-type $\text{Bi}_{0.4}\text{Sb}_{1.6}\text{Te}_3$ grains (a) with and (b) without the hydrothermal treatment, while (c) and (d) show clearer details in smaller scales about the fluffy surface after the treatment.

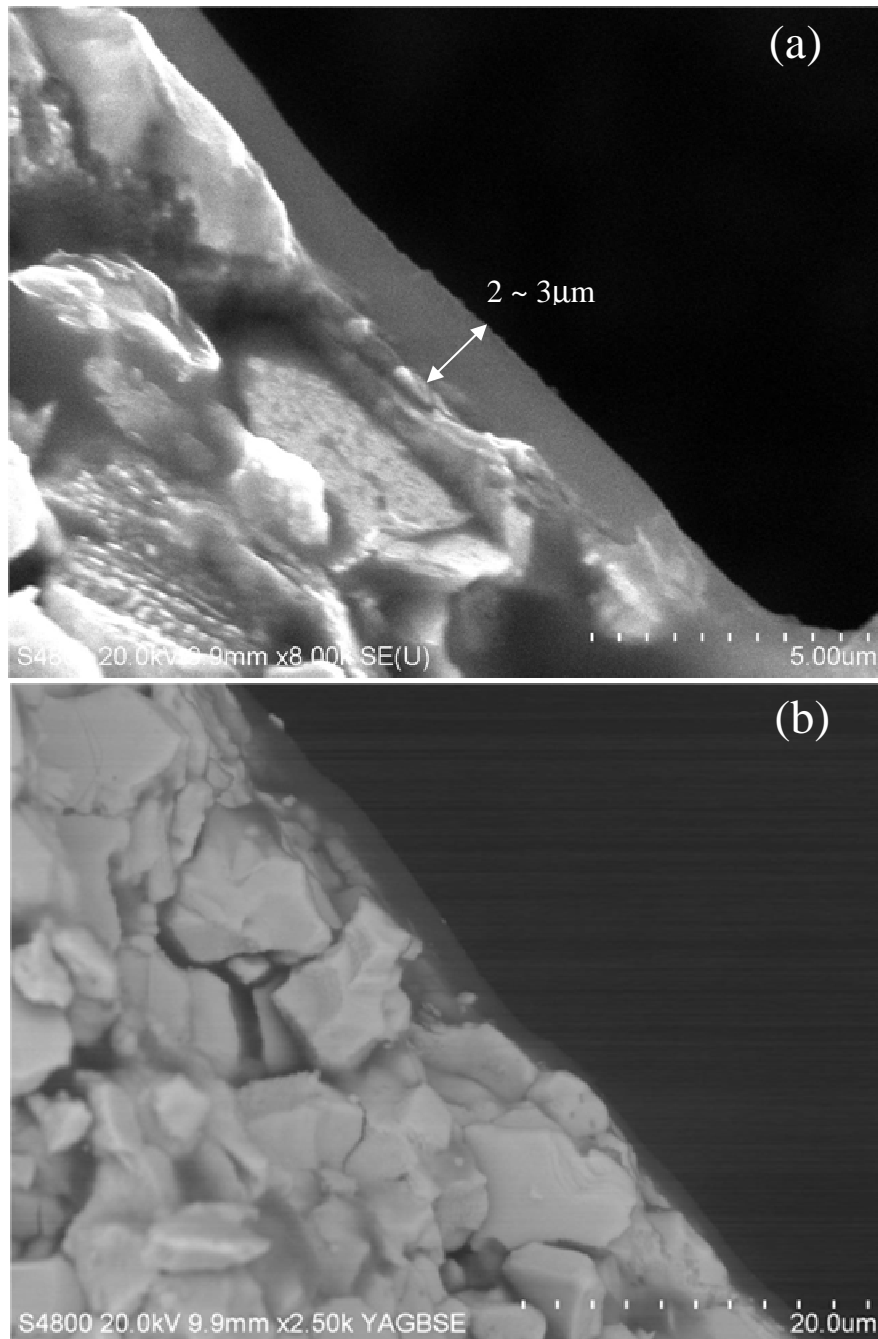
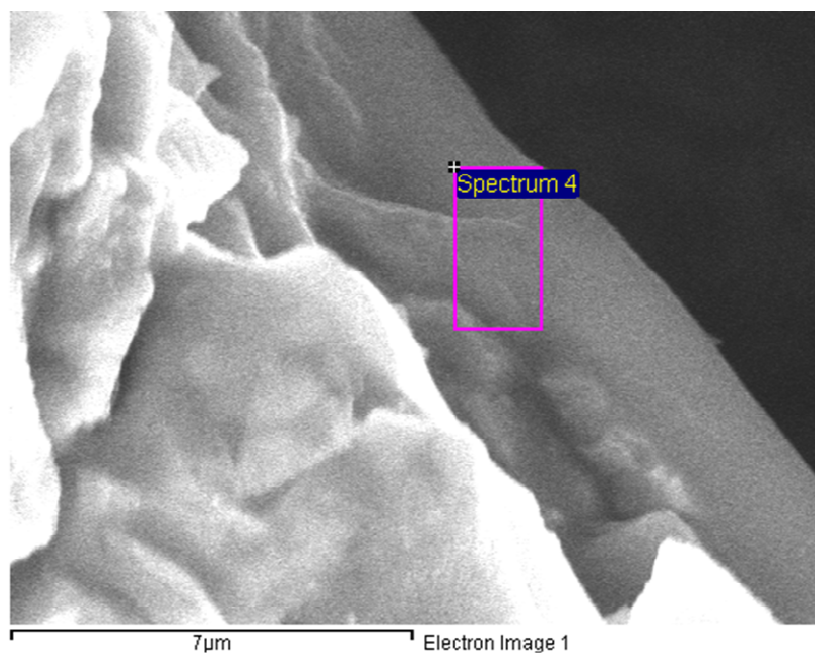


Figure 3.2 SEM pictures of commercial p-type $\text{Bi}_{0.4}\text{Sb}_{1.6}\text{Te}_3$ ingot after hydrothermal treatment. (a) shows a thin surface layer formed on the ingot while (b), taken in backscattering mode, shows this layer is comprised of light elements.



Element	Weight%	Atomic%
C	66.92	75.10
O	27.04	22.78
Na	2.38	1.40
Cl	1.21	0.46
Sb	0.07	0.01
Te	2.17	0.23
Bi	0.11	0.01
Total	100	100

Figure 3.3 The EDS analysis of the surface layer formed on the hydrothermally treated p-type $\text{Bi}_{0.4}\text{Sb}_{1.6}\text{Te}_3$ ingot. The composition data in the table shows the existence of Na in the selected area of the surface layer.

which are the main compositions of the raw ingot.

This type of surface is also observed on polycrystalline $\text{Bi}_{0.4}\text{Sb}_{1.6}\text{Te}_3$ samples after hydrothermal treatment. A small Na-treated particle of interest was selected for the TEM and mapping EDS analysis. The TEM picture of Figure 3.4 (a) shows that an as-treated grain is encapsulated by a translucent thin layer of several tens of nanometers. The layer is virtually transparent, indicating that it has very low electron density or mainly consists of light elements. The EDS element mapping as shown in Figures 3.4 (b) (c), (d) and (e) portray how elements Na, Sb, Te and Bi are distributed on and near the surface of the particle. These pictures show that Na covers all the particle and spreads into the translucent thin surface layer while Sb, Te and Bi, which are the main constituents of the raw grain, mostly stay in the grain and are very scarce in the surface layer. The table besides Figure 3.4 (a) lists the percent weight and atomic ratios of each element found by EDS. Although the numbers in the table are for reference only, but not for any quantitative analysis, they do prove the existence of a small amount of Na in the surface layer after the hydrothermal treatment. The table does not list any data about B. First, EDS is not a good approach to detect light elements like B. Second, according to the phase diagram, the creation of bonding of B with other elements in the sample requires a much higher temperature than it is in the process of hydrothermal treatment and hot-press. Therefore, B, if any, must exist in the form of BH_4 in the sample. However, its existence has not been proven by the FTIR spectroscopy as shown in Figure 3.11. With the same method, similar thin and translucent surface layers containing Rb or K are also observed to encapsulate the $\text{Bi}_{0.4}\text{Sb}_{1.6}\text{Te}_3$ grains after the Rb- and K-treatments, respectively.

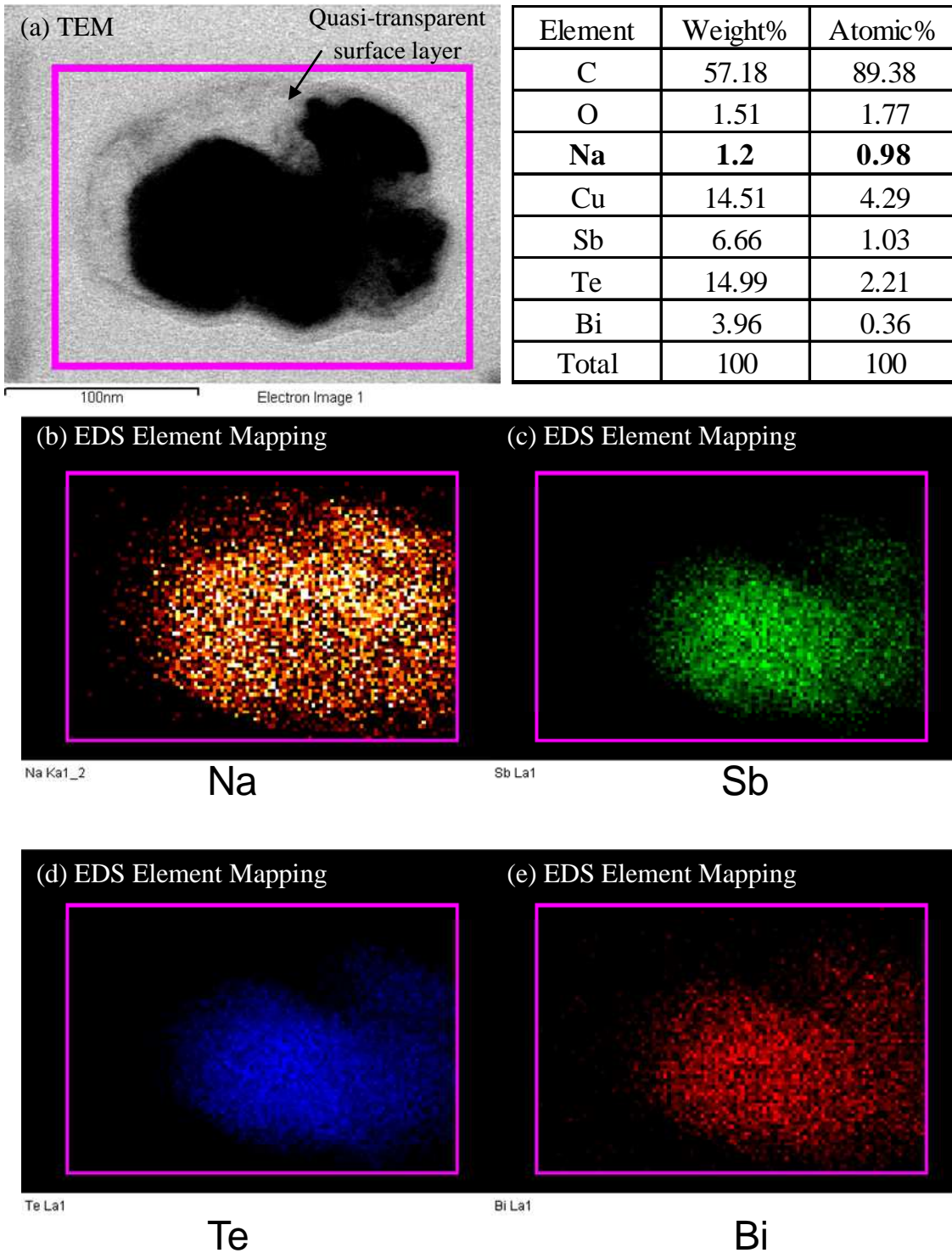


Figure 3.4 The EDS analysis of a Na-hydrothermally treated p-type $\text{Bi}_{0.4}\text{Sb}_{1.6}\text{Te}_3$ grain. (a) shows the grain is encapsulated by a quasi-transparent layer and the compositions in the selected area is listed in the table aside. Figures (b) ~ (e) are the element mapping showing the distribution of Na, Sb, Te and Bi, respectively, in the area.

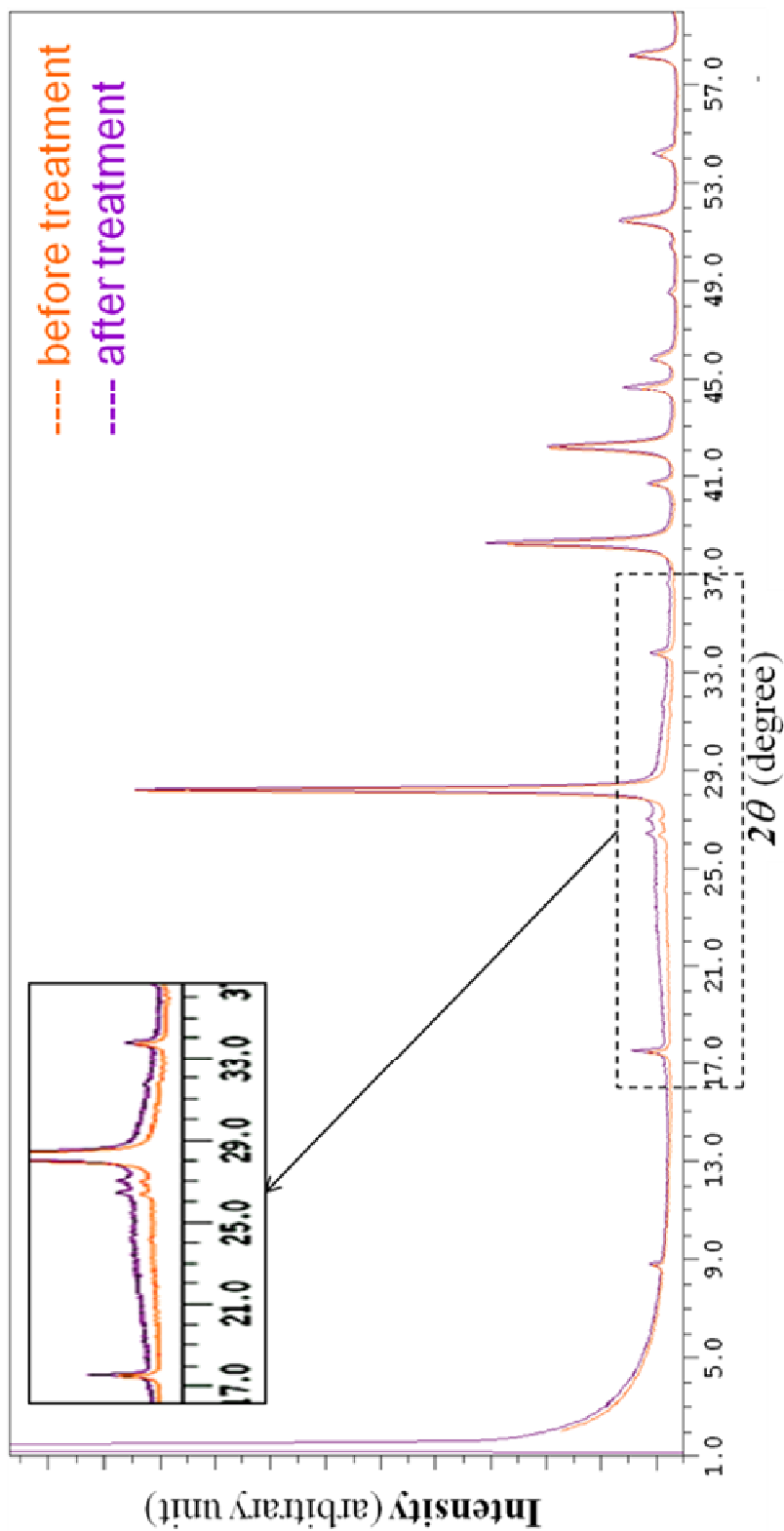


Figure 3.5 The XRD patterns of p-type $\text{Bi}_{0.4}\text{Sb}_{1.6}\text{Te}_3$ powders before and after hydrothermal treatment. The insert shows a broad hump in the background centered at 27° for treated sample.

3.3 Structure of Surface Layers

Figure 3.5 shows the comparison in the high resolution powder XRD patterns of p-type $\text{Bi}_{0.4}\text{Sb}_{1.6}\text{Te}_3$ samples before and after hydrothermal treatment. There are no extra peaks or appreciable peak shifts in the figure for the hydrothermally treated sample. It seems that the surface layer observed under the SEM is not detectable by powder XRD. Recalling the small percent of weight and atomic ratios of Na listed in the table in Figure 3.4, one may attribute the XRD's being unable to detect any crystalline phase of the surface layer to its rather small amount, if any at all. However, there may exist another explanation that the powder XRD patterns before and after hydrothermal treatment are almost identical because the surface layer observed is possibly a non-crystalline or amorphous phase. Looking closely at the inset in Figure 3.5, one may also notice that there is a broad hump in the background centered at about 27° for the hydrothermally treated powder. In addition, the correlation length is calculated to be 3.5 \AA using the Bragg's law. This hydrothermally treated sample's broad hump shown in the powder XRD pattern constitutes evidence supporting the second scenario discussed above.

Figures 3.6 (a) and (b) show the LEED (low energy electron diffraction) pattern of untreated sample and the SAED pattern of treated sample, respectively. The untreated particle exhibits hexagonal patterns in Figure 3.6 (a) while in Figure 3.6 (b) the treated grains, in addition to the hexagonal patterns, a couple of halos are apparent, which strengthens the assumption that the surface layer of interest is probably a non-crystalline or amorphous phase.

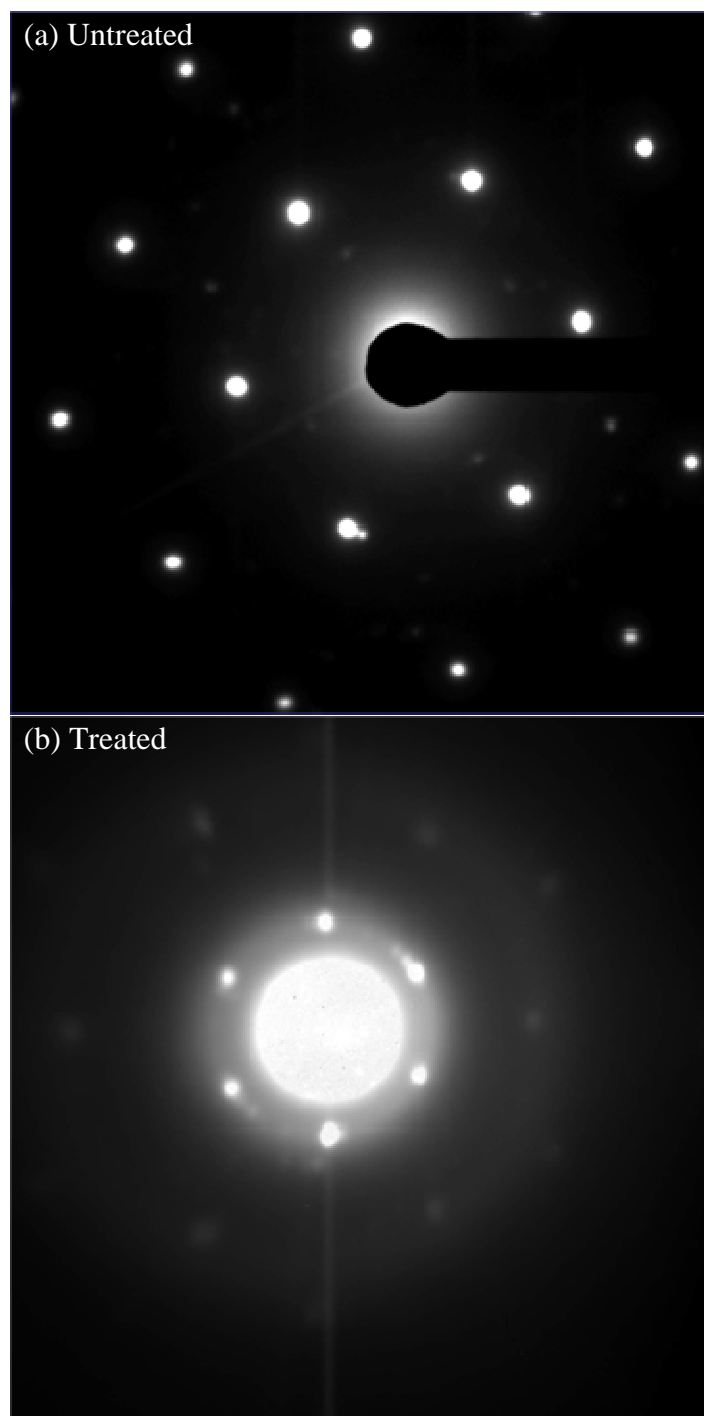


Figure 3.6 (a) the LEED pattern of untreated p-type $\text{Bi}_{0.4}\text{Sb}_{1.6}\text{Te}_3$ grains. (b) the SAED pattern of treated p-type $\text{Bi}_{0.4}\text{Sb}_{1.6}\text{Te}_3$ grains.

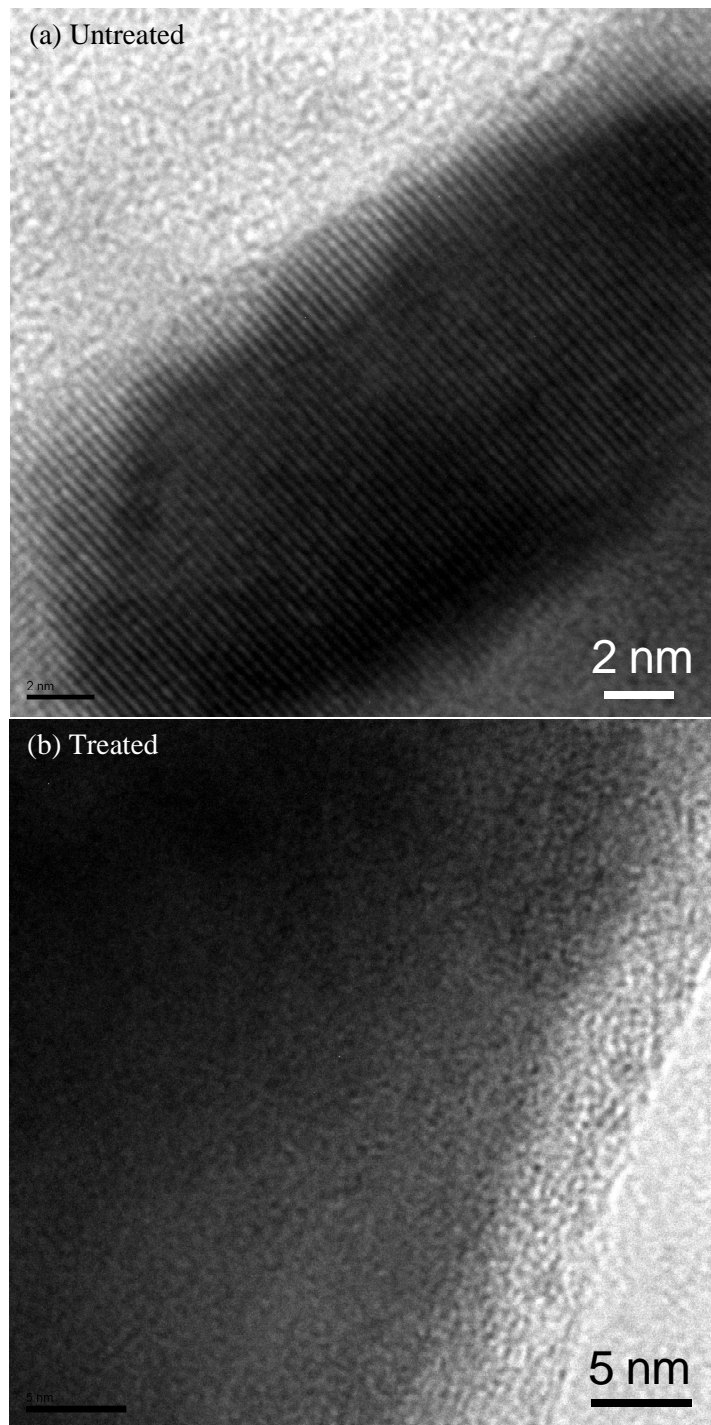


Figure 3.7 The HRTEM images of p-type $\text{Bi}_{0.4}\text{Sb}_{1.6}\text{Te}_3$ grains (a) before and (b) after the hydrothermal treatment.

High-resolution TEM (HRTEM) has also been performed to determine the crystallinity of the surface layer. Before the hydrothermal treatment, the $\text{Bi}_{0.4}\text{Sb}_{1.6}\text{Te}_3$ grain in Figure 3.7 (a) clearly exhibits well-aligned crystal planes, which is typical of a single crystalline feature. For the grain after the treatment as shown in Figure 3.7 (b), however, no distinct crystalline feature is observed either in the surface layer (light-colored area) or in the grain (dark-colored area). The grain's demonstrating no crystallinity is plausible if one recalls that the grain is encapsulated by the surface layer in Figure 3.4.

In order to produce specimens comprised of higher percentage surface layers encapsulating the $\text{Bi}_{0.4}\text{Sb}_{1.6}\text{Te}_3$ grains, hydrothermally treated powders underwent ultrasonic vibration for approximately 15 minutes', which resulted in the peeling-off of the surface layer from the grain in the SEM picture shown in Figure 3.8. When the SAED analysis was conducted on the fragments of the surface layers that were peeled off, a pattern of square symmetry, which could be characteristic of a cubic single crystal, was observed in Figure 3.9 as well as the halos. Although the non-crystalline or amorphous features are present in the same picture, the surface layer somehow demonstrates a new phase of cubic single crystal structure, which is completely different from the hexagonal lattice structure of original Bi_2Te_3 . However, the crystallinity of such surface layers may still be very slight if one considers the almost identical power XRD patterns shown in Figure 3.5.

Additionally, the ease of peeling-off of the surface layer from the grains after ultrasonic vibration provides a speculation that after the hydrothermal treatment a similar

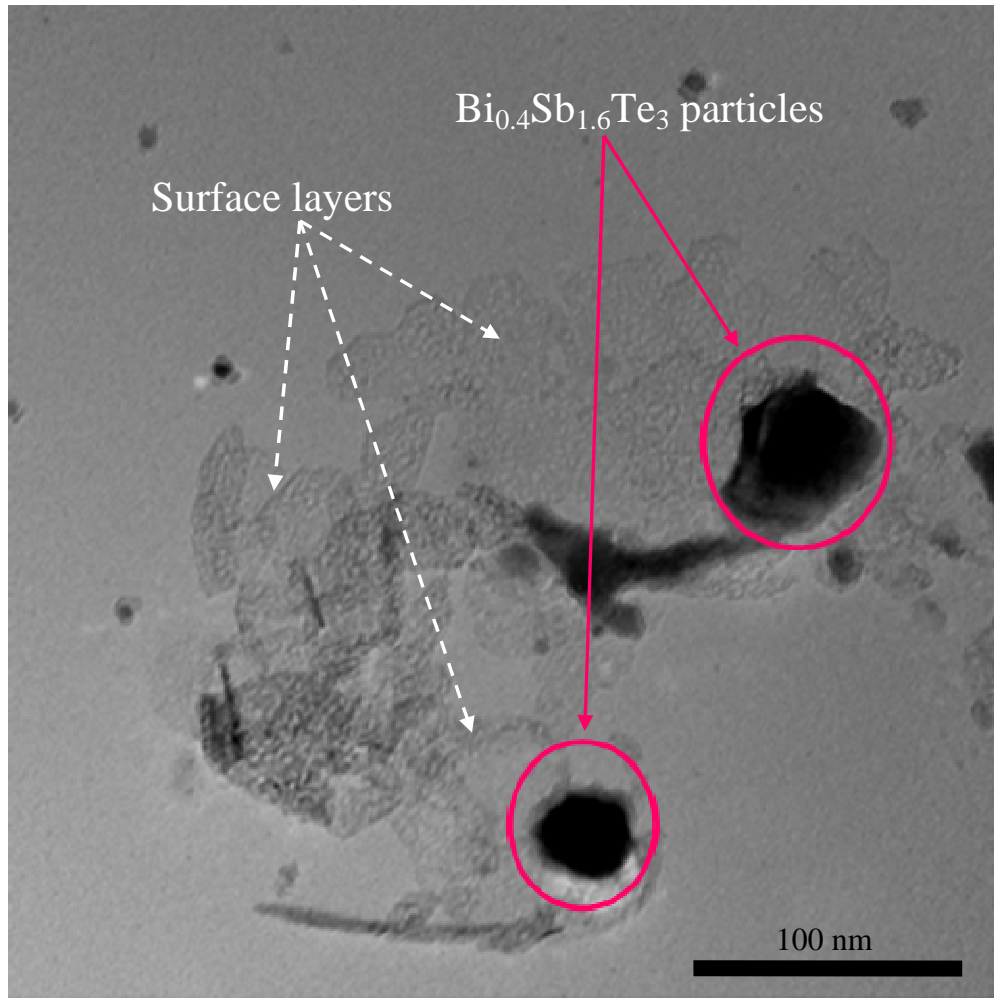


Figure 3.8 The easy peeling of the surface layer from hydrothermally treated p-type $\text{Bi}_{0.4}\text{Sb}_{1.6}\text{Te}_3$ grains after ultrasonic vibration.

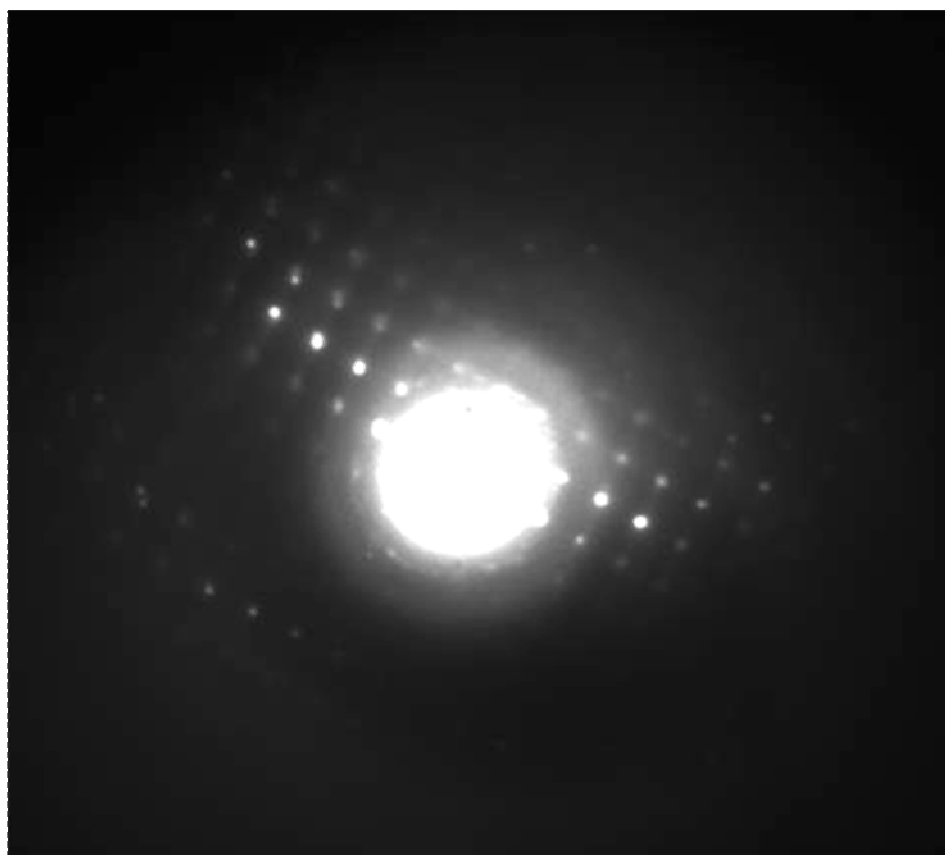
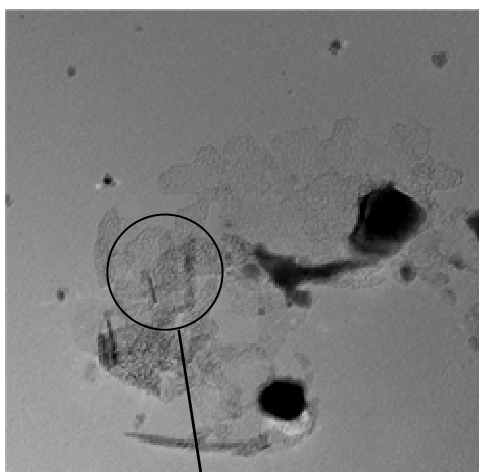


Figure 3.9 The SAED image of the surface layers peeled off from hydrothermally treated p-type $\text{Bi}_{0.4}\text{Sb}_{1.6}\text{Te}_3$ grains after ultrasonic vibration.

layer might be able to form on the grains of other polycrystalline thermoelectric materials to hopefully improve their thermoelectric performances. Such an idea was transferred to p-type polycrystalline PbTe system not long after its successful application on p-type Bi₂Te₃, and the effectiveness of hydrothermal treatment on enhancing the *ZT* has been proven as well although it is achieved in another way.⁸¹

3.4 Possibility of Alkali Atoms' Intercalation into the Bi₂Te₃ Matrix

The Bi₂Te₃ lattice is a rhombohedral crystal structure that belongs to the space group D_{3d}⁵ (*R* $\bar{3}m$) with five atoms in the trigonal unit cell. A hexagonal unit cell that contains three formula cells can be taken as shown in Figure 3.10 with lattice constants $a = 4.395 \text{ \AA}$ and $c = 30.440 \text{ \AA}$.⁸²⁻⁸⁶

The hexagonal unit cell can be simply visualized as the stacking of quintuple layers of atoms along the *c*-axis. There are fifteen layers in three groups of five-layer stacks of Te(1)–Bi–Te(2)–Bi–Te(1), where Te (1) and Te (2) denote two types of Te atoms in the unit cell. The bonds between Te(1)–Bi and Bi–Te(2) are of ionic-covalent type whereas those between Te(1)–Te(1) are of Van der Waals type.⁸⁷ The distance between Te(1)–Te(1) planes is 2.456 Å. In solid solutions of Bi₂Te₃–Sb₂Te₃, for example, the p-type Bi_{0.4}Sb_{1.6}Te₃, Sb atoms substitute in Bi sites without radically changing the structure of the hexagonal unit cell although some of the five-layer stacks become Te(1)–Sb–Te(2)–Bi–Te(1).⁶ In either case, the weak Van der Waals bonds between Te(1)–Te(1) are responsible for the easy cleavage of Bi₂Te₃ or Bi₂Te₃–Sb₂Te₃ solid solutions along the

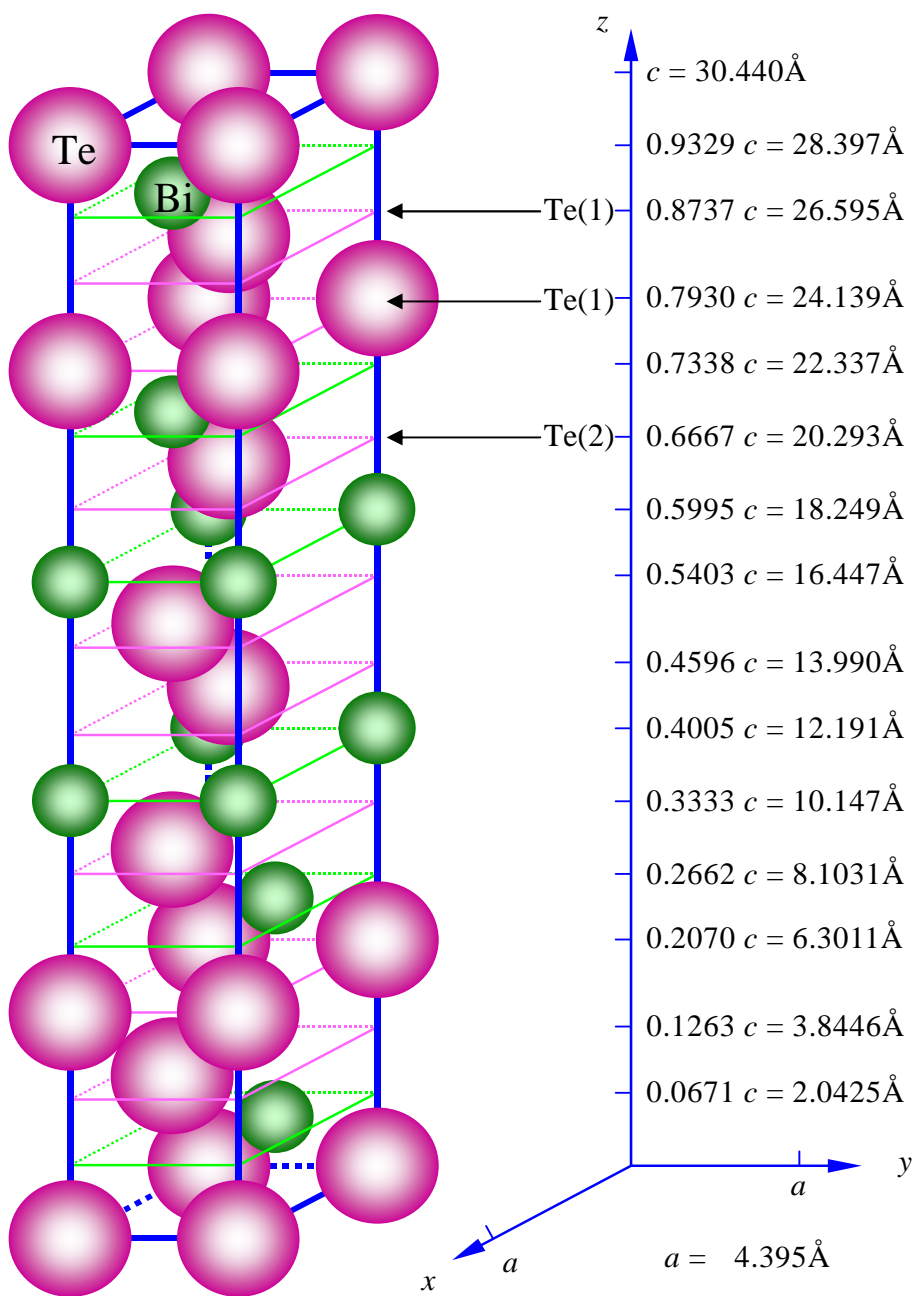


Figure 3.10 The lattice structure of Bi_2Te_3 .

planes perpendicular to the c -axis. Also, because of the weak Van der Waals bonds, Te(1)-Te(1) gaps are inclined to accommodate foreign atoms.⁸⁸⁻⁹² In other words, if alkali metal atoms are found after the hydrothermal treatment, which has been proven by the EDS, they are very likely to be bonded to the Bi₂Te₃ matrix in form of intercalation into Te(1)-Te(1) gaps.

The powder XRD pattern shown in Figure 3.5 possesses a big hump in the background centered at 27° for hydrothermally treated sample and this hump has a correlation length of approximately 3.5 Å, which is wider than the Te(1)-Te(1) gaps. The increase in the width of Te(1)-Te(1) gaps may be considered as strong evidence for the intercalation,^{90,92} but some other phenomena observed contradict with this argument.

If the Te(1)-Te(1) gaps are filled by alkali metal atoms, the bonds between T(1)-T(1) planes would be somehow affected, leading to new vibration modes among intercalated atoms and among Te(1) atoms. Such kinds of vibration modes can be detected by the infrared spectroscopy. In order to investigate whether the intercalation of alkali metal atoms into Te(1)-Te(1) gaps is the situation after the hydrothermal treatment, FTIR absorption spectra from treated and untreated samples are compared in Figure 3.11. The wave number used ranges from 500 ~ 4000 cm⁻¹, which covers the mid-infrared scope that corresponds to the energy levels of fundamental vibration modes. However, there are no appreciable new peaks or peak shifting when two curves from treated and untreated samples are compared as shown in Figure 3.11. According to the spectroscopic signatures of H₂O molecules, lacking peaks near 2150 cm⁻¹ excludes the existence of water in the sample.⁹³

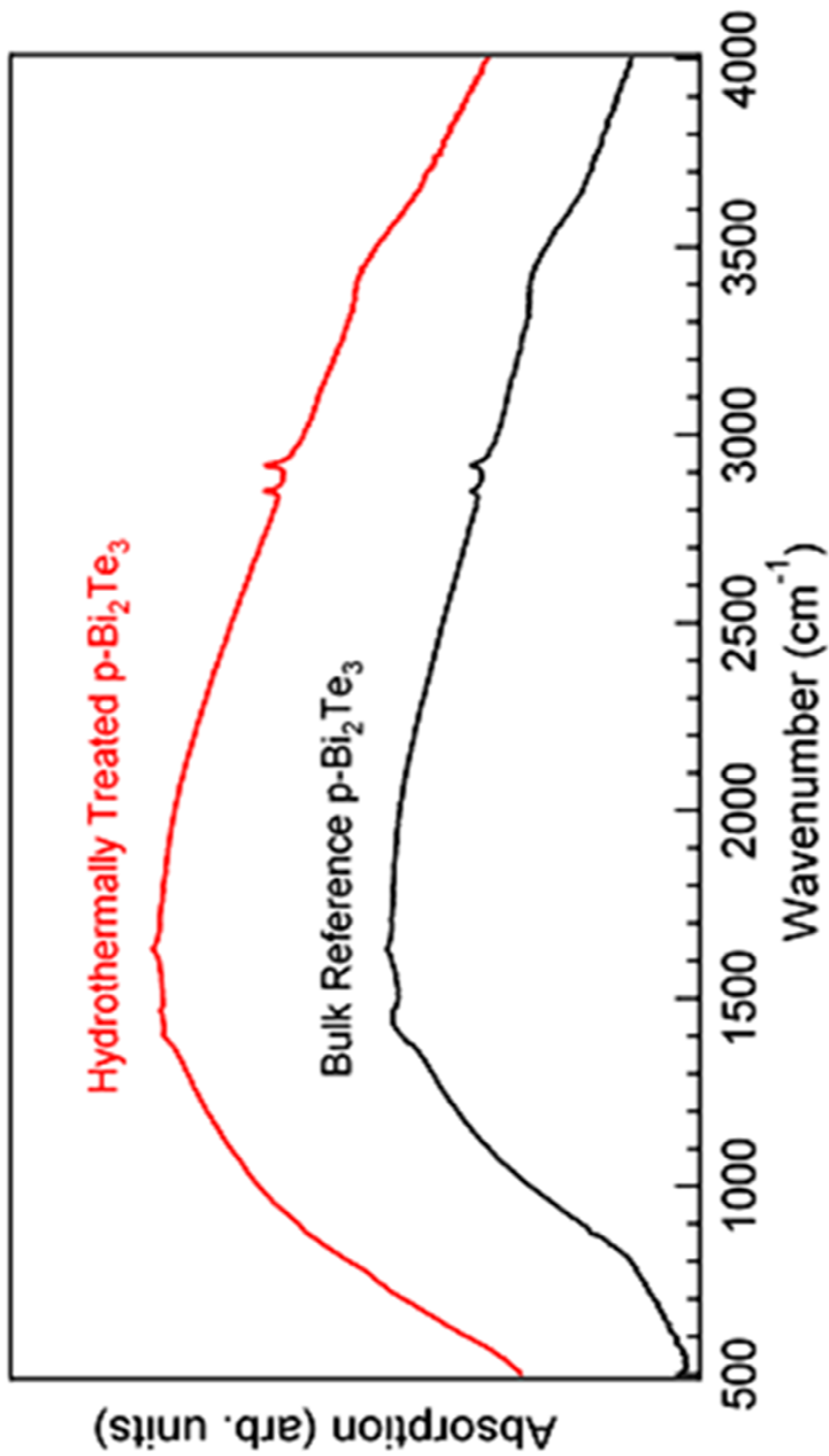


Figure 3.11 The Fourier transform infrared absorption spectra of untreated and hydrothermally treated p-type Bi_{0.4}Sb_{1.6}Te₃ samples.

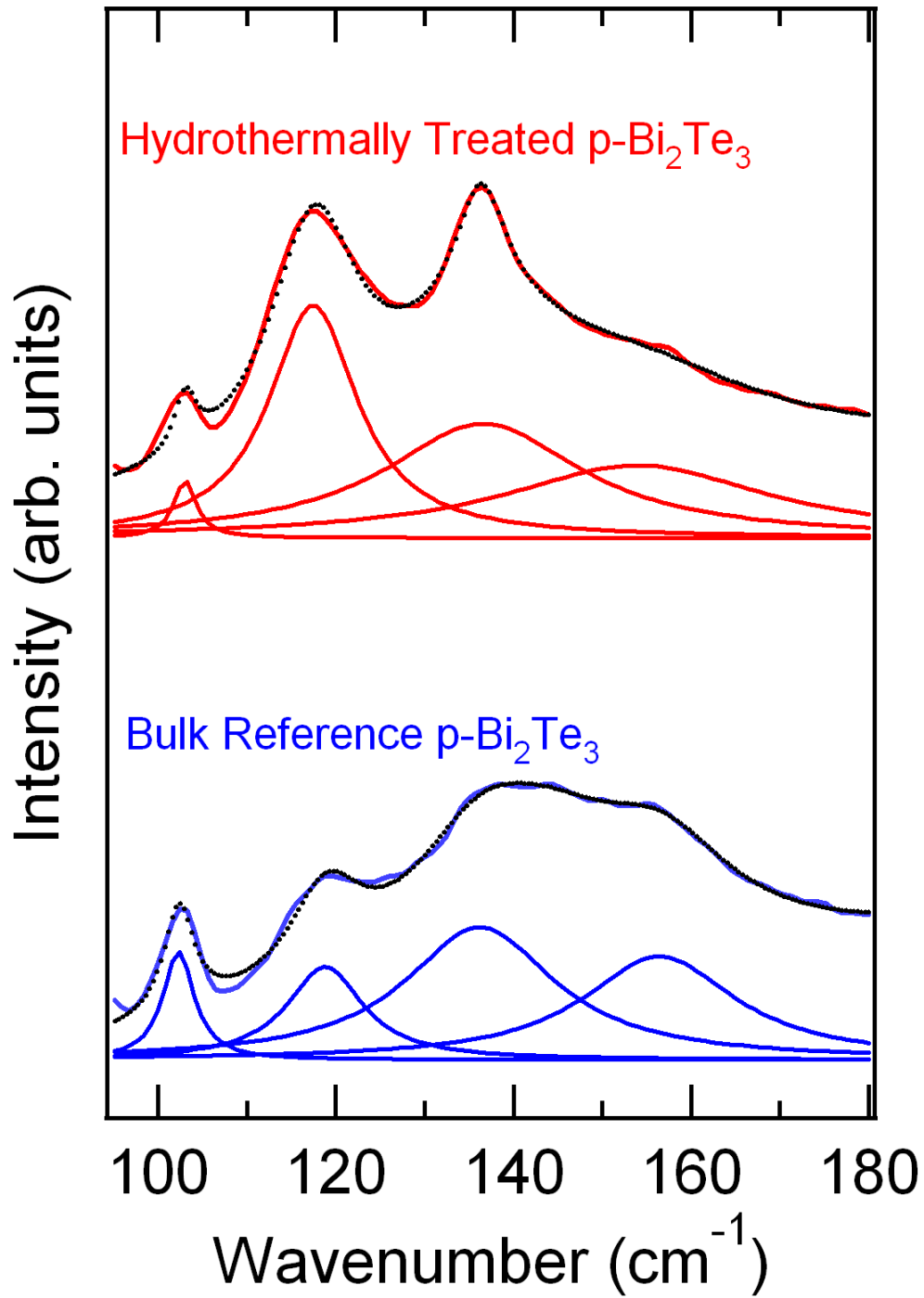


Figure 3.12 The Raman spectra of untreated and hydrothermally treated p-type Bi_{0.4}Sb_{1.6}Te₃ samples.

Raman spectroscopy is another technique that is used to detect vibrational, rotational and other low-frequency phonon modes in materials. Figure 3.12 shows the comparison in Raman spectroscopy of treated and untreated samples. In untreated sample, Raman peaks near 102 cm^{-1} and 134 cm^{-1} , which correspond to E_g^2 and A_{1g}^2 modes, respectively, in pure Bi_2Te_3 ,⁹⁴ are seen as expected. It has been reported that the position of the peak at 134 cm^{-1} is sensitive to the stoichiometric composition in $\text{Bi}_2\text{Te}_3\text{-Sb}_2\text{Te}_3$ system, and it shifts to around 160 cm^{-1} in $\text{Bi}_{0.4}\text{Sb}_{1.6}\text{Te}_3$.⁹⁵ The peak that is close to 120 cm^{-1} is attributed to the phonon frequency of 120 cm^{-1} (A_{1u}) from Bi_2Te_3 .⁹⁵ After hydrothermal treatment, the peaks near 120 cm^{-1} and 134 cm^{-1} become sharper. The reason is not clear yet. One possibility is that the lattice is aligned better after the hydrothermal treatment. Although the shapes and the amplitudes of the untreated sample are not the same as the treated one, no new peak or shifting has been observed in treated sample, which, combining with the FTIR analysis data, does not provide proofs in favor of proposed intercalation of alkali atoms into Te(1)-Te(1) planes in the Bi_2T_3 matrix.

3.5 TGA analysis

Figure 3.13 shows the percent weight loss of $\text{Bi}_{0.4}\text{Sb}_{1.6}\text{Te}_3$ polycrystalline samples during TGA analysis from room temperature to $600\text{ }^\circ\text{C}$. If one refers to the curve of the untreated Bulk Reference, the whole process of weight loss can be divided into two stages, below and above $420\text{ }^\circ\text{C}$, respectively. Since Bi_2Te_3 is a typical low temperature thermoelectric material, all three samples lose weight much faster when temperature goes above $420\text{ }^\circ\text{C}$ because they begin to decompose, especially for Sb in the samples, which

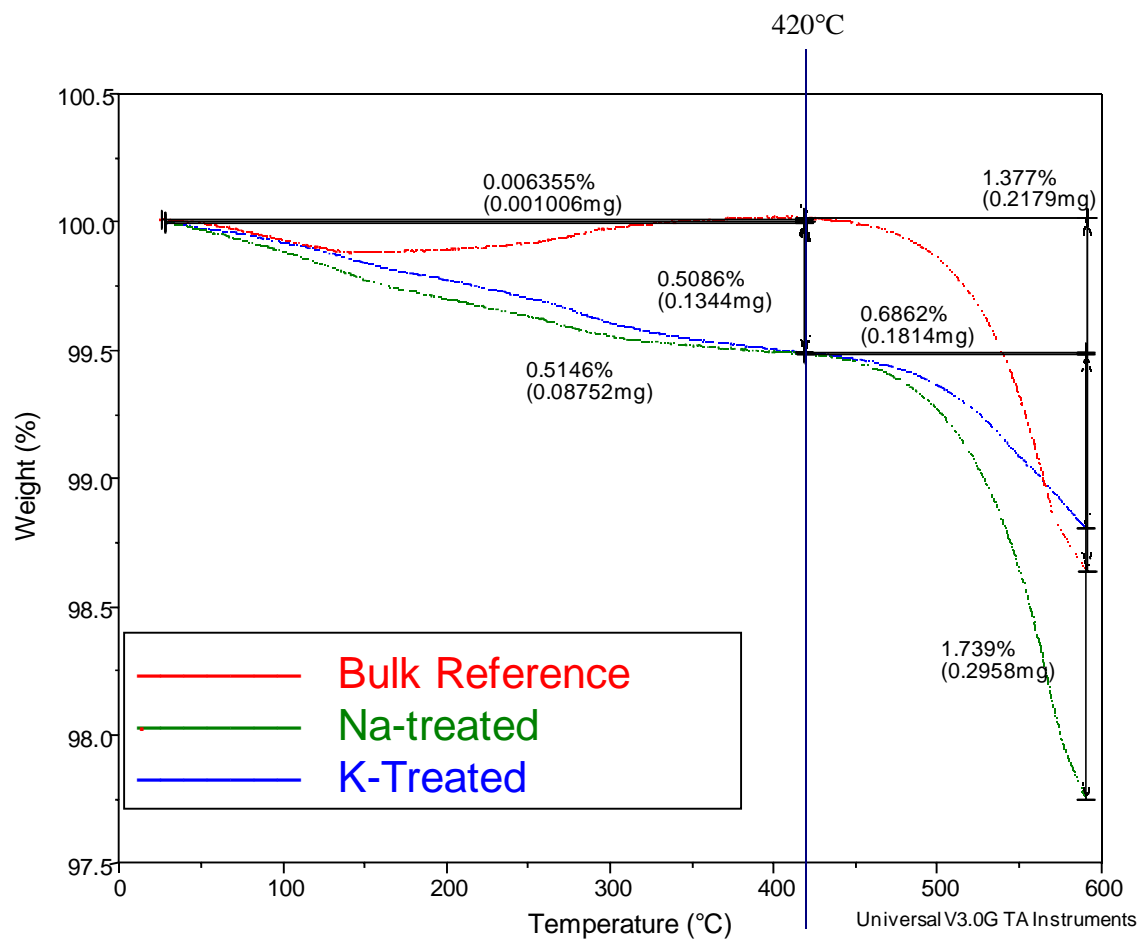


Figure 3.13 The TGA analysis of untreated, Na- and K-treated p-type $\text{Bi}_{0.4}\text{Sb}_{1.6}\text{Te}_3$ polycrystalline samples.

is easy to vaporize. Below 420 °C, the Bulk Reference is pretty stable and the weight loss is close to zero (0.006%). On the contrary, both Na- and K-treated samples undergo a loss of about 0.5%, which is two orders of magnitude larger than that of the Bulk Reference although this is only a very small fraction of the total sample mass.

Therefore, the TGA data of treated samples below 420 °C may be attributed to the decomposition of the grain boundary layer observed with SEM, and thus can be taken as a proof for the existence of this layer. Moreover, the TGA data shows what a small amount this layer accounts for in term of mass. This may cause difficulties in detecting this layer with good resolution by other techniques, some of which have been tried and shown above.

3.6 Conclusion

A surface layer has been found to form on the p-type $\text{Bi}_{0.4}\text{Sb}_{1.6}\text{Te}_3$ samples after the hydrothermal treatment with the SEM. Other techniques such as XRD, EDS, HRTEM, FTIR, Raman spectroscopy and TGA, have been employed in subsequent investigations, which show that this layer does not have typical single crystalline structure, mainly consists of light elements, and only constitute a very small amount of mass in the sample. However, the detailed structure and composition of this surface layer remain unclear and requires follow-up efforts.

4. HYDROTHERMAL TREATMENT WITH COMBINED ALKALI METAL SALTS

4.1 Introduction

Most existing thermoelectric materials are in the form of polycrystals that contain numerous grain boundaries. Polycrystalline materials are by nature advantageous over single crystals in terms of a lower κ . However, the presence of grain boundaries also degrades the electrical conductivity. As part of the effort to address the problem, the data presented in Chapters 2 and 3 have demonstrated that the hydrothermal treatment using alkali metal salts XBH_4 ($X=$ Na, K or Rb) coated a thin layer on the p-type $Bi_{0.4}Sb_{1.6}Te_3$ grains, where it becomes a thermoelectrically favored grain boundary upon hot-pressing. Compared with the untreated samples, the ZT of as-treated polycrystalline p- Bi_2Te_3 is improved by somewhat decoupling α , ρ and κ in such a way that:

1. Na-treatment lowers κ the most.
2. Rb-treatment improves the PF the most by decreasing ρ and slightly increasing α .
3. K-treatment is mediocre in term of the improvements in κ and PF .

Such results were obtained on different samples and thus prompted an intriguing question as to whether the decoupling would take place if two alkali metal salt solutions were applied together on the same sample. Particularly, whether the combination of Na- and Rb-treatments, which improved κ and the PF most, respectively, would lead to a resultant ZT as if these two treatments benefit, work independently from, or against each other. The effects of hydrothermal treatment on polycrystalline p-type $Bi_{0.4}Sb_{1.6}Te_3$ by

combining Rb and Na salts with different molar ratios are herein reported in Chapter 4 as follows.

4.2 Sample Synthesis

The samples were prepared basically following the same procedures as the single alkali metal salt treatment discussed in Chapter 2. A commercial p-type $\text{Bi}_{0.4}\text{Sb}_{1.6}\text{Te}_3$ ingot from Marlow Industries, Inc. was crushed and hand-ground into powders. Since it has been proven in Chapter 2 that the hydrothermal treatment has consistently more improvement to ZT as particle size decreases, only powders of particle size $\leq 20\mu\text{m}$ after sifting were selected for subsequent processing and characterization.

A treatment process usually took 2 grams of such powder. The powder was put into a 45 ml capacity Teflon-lined autoclave containing alkali metal salt aqueous solution that dissolved a mmol NaOH, b mmol NaBH_4 , c mmol RbOH and d mmol RbBH_4 while the ratio $R = a:b = c:d$ was kept. In order to find the optimal ratio that enhanced ZT the most, approximately 40 recipes were tried by varying R . The autoclave was then sealed and heated in a furnace at $150\text{ }^\circ\text{C}$ for 24 hours followed by furnace cooling. The powder was then taken out of the autoclave, washed thoroughly with distilled water and ethanol, and dried under ambient conditions. The as-treated powder was then hot-pressed in a half inch die at $330\text{ }^\circ\text{C}$ under 90 MPa for 30 minutes to form a 2 mm thick pellet whose density was $6.4 \pm 0.1\text{g/cm}^3$. In comparison, the density of the original ingot was $6.20 \pm 0.05\text{g/cm}^3$, and the theoretical maximum density of p-type Bi_2Te_3 is 6.78g/cm^3 .

Treated samples were named after the molar ratio of Na to Rb, in another words, $a:b$ or $c:d$, in the starting alkali metal salt aqueous solution. For example, the sample treated with the alkali metal salt solution of $a:b = c:d = 1:2$ was called the 1Na2Rb sample. A pellet made of as-sifted ingot powders without any hydrothermal treatment was hot-pressed as a Bulk Reference.

All the pellets, treated and untreated, were cut along the radial direction into roughly $2 \times 2 \times 8 \text{ mm}^3$ bars, on which the measurements of three thermoelectric properties were performed to finally determine ZT . A bar cut from the original commercial ingot along its growth direction was used as a second comparison to the treated samples.

4.3 Microscopic Images

A small amount of powders taken from as-treated and hot-pressed sample was first analyzed with the Transmission Electron Microscopy (TEM) and the Energy Dispersive Spectroscopy (EDS) on a Hitachi HD2000 electron microscope equipped with Oxford INCA Energy 200 EDS detector.

Similar to the results from the Na-only-treated samples, the TEM image in Figure 4.1 shows that a thin surface layer of tens of nanometers forms that encapsulates the grains. Furthermore, this surface layer is found by EDS to contain both Na and Rb. Counting all other elements detected such as Bi, Sb and Te at Spots A, B and C, i.e., from the center of the grain to the surface, EDS element analysis indicates that the nominal atomic percentages of Na and Rb were 20% and 0%, respectively, at Spot A, then

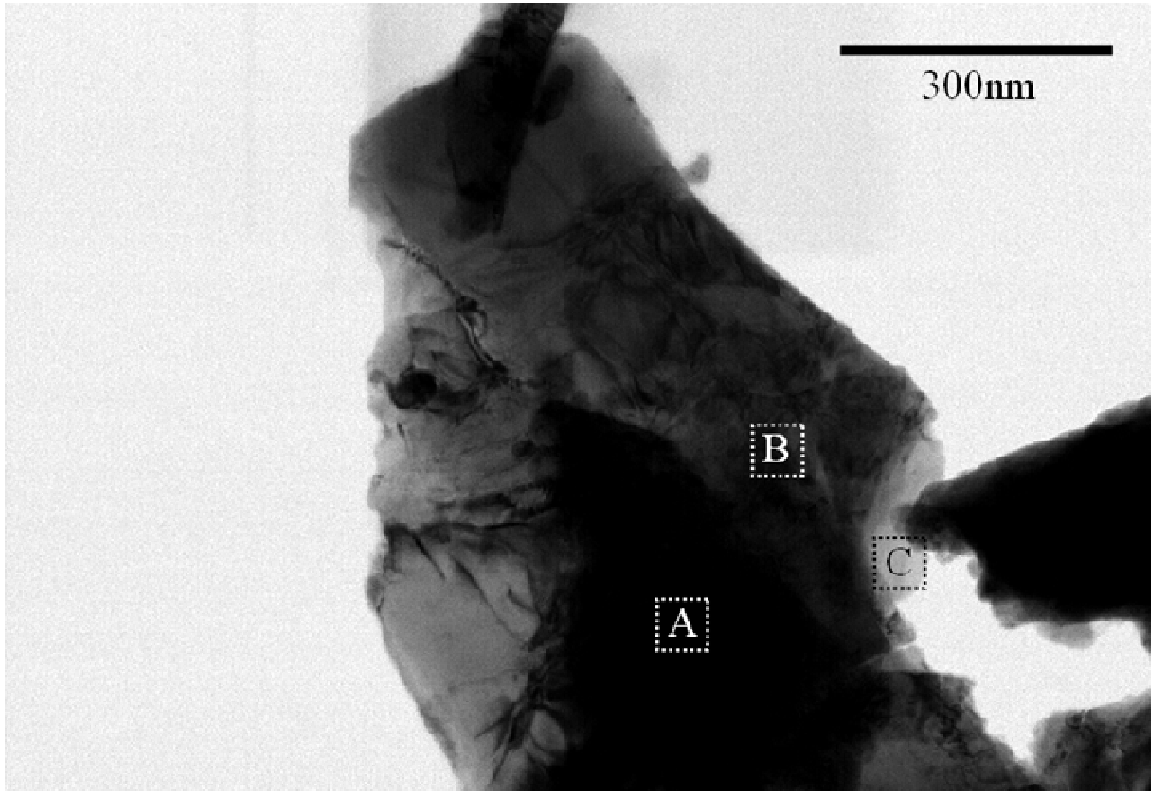


Figure 4.1 A TEM image of combined Na- and Rb-treated Bi_{0.4}Sb_{1.6}Te₃ grain. The surface layer is clearly seen. EDS shows the nominal atomic percentages of Na and Rb increase from 20% and 0%, to 50% and 0.5%, and finally to 50% and 5% at Spots A, B and C, respectively.

increased to 50% and 0.5% at Spot B, and finally to 50% and 5% at Spot C, suggesting a composition gradient of Na and Rb, which are obviously the resultants from Na-and-Rb-treatment, along the depth direction of the grain.

4.4 The Decoupling of Thermoelectric Properties

The measurements of α , ρ and κ were performed as introduced in Chapter 2. The thermoelectric properties at 300 K of some selected samples are illustrated in Figure 4.2 where the 1Na2Rb-treated one yields the highest ZT . Among all the curves shown in Figure 4.2, the α one is the flattest as the composition varies, except for the Na-only-treated sample, implying the independence or decoupling of α from ρ and κ .

Such decoupling can be more clearly seen by plotting ZT vs. σ/κ in Figure 4.3, where Na-and-Rb-treated samples produce a straight line regardless of the Na to Rb molar ratio. The linearity means that the variations in ZT is solely a result of the change in σ/κ . In another word, the linear zone corresponds to a region where α , ρ and κ are decoupled. Na-only-treated sample's remarkable drop in the α curve shown in Figure 4.2 is the reason for its deviation from the linearity in Figure 4.3. On the contrary, the deviation of Rb-only-treated sample from the linearity originates from its highest α in Figure 4.2 although these two samples have roughly same σ/κ value. When Na- and Rb-treatments are applied together with different molar ratios, they are complementary to each other to form the straight line shown in Figure 4.3. Additionally, by varying the Na

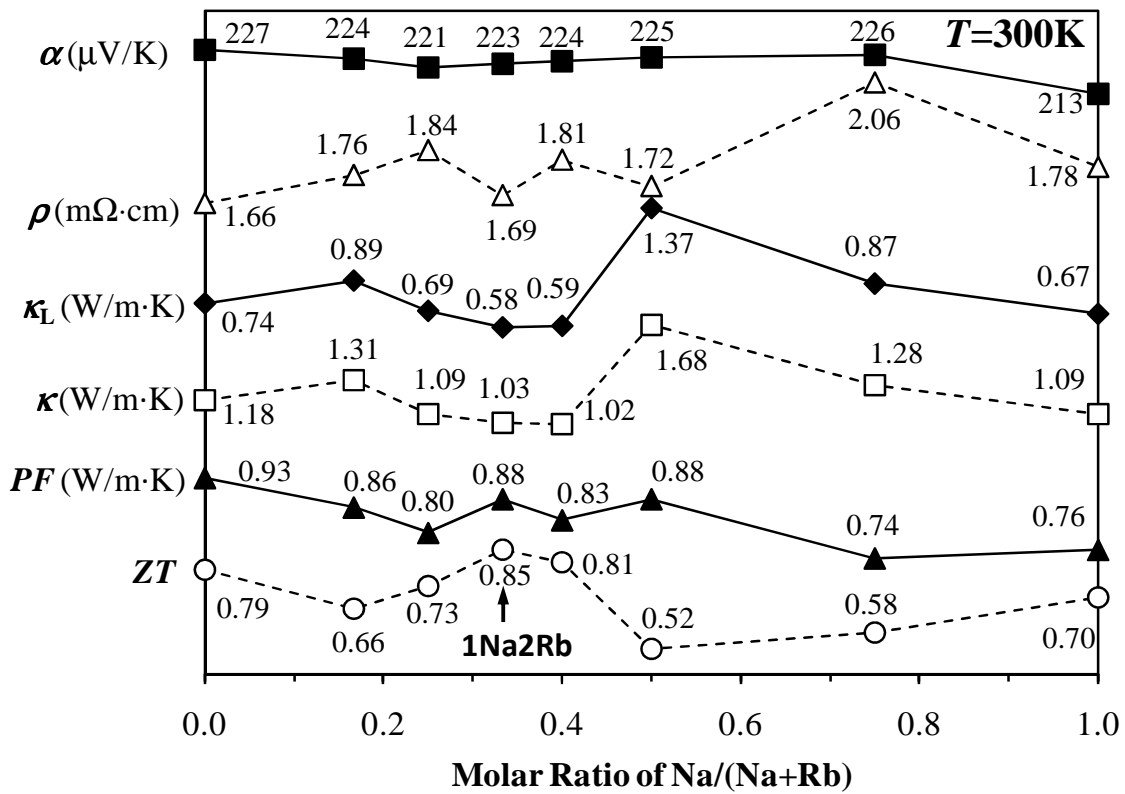


Figure 4.2 The compositional dependences of the Seebeck coefficient α , resistivity ρ , lattice thermal conductivity κ_L , thermal conductivity κ , power factor PF and ZT of Na- and Rb- treated polycrystalline p-Bi₂Te₃ samples at 300K. The molar ratio of Na: Rb=1:2 yields the highest $ZT=0.85$.

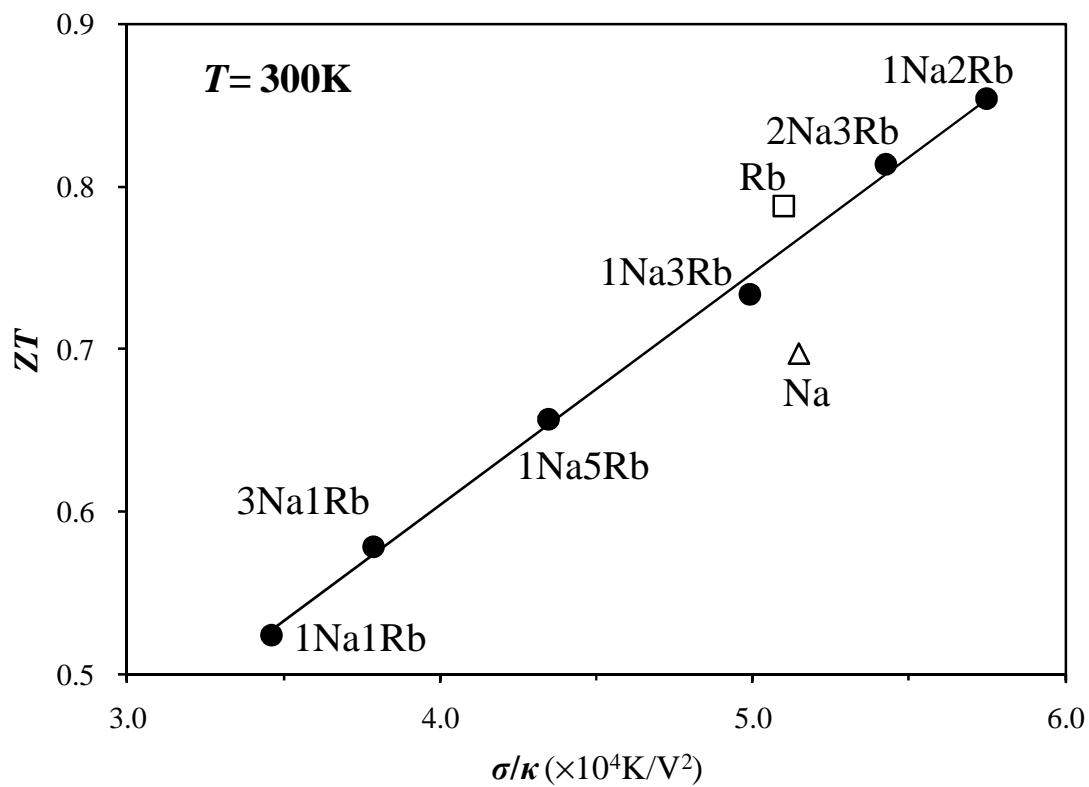


Figure 4.3 At 300K, ZT as a function of σ/κ , the ratio of the electrical to thermal conductivity for hydrothermally treated polycrystalline p-Bi₂Te₃ samples.

to Rb molar ratio, ZT can be improved by more than 60% from 0.52 for 1Na1Rb sample to 0.86 for 1Na2Rb sample.

Relating the linear correlation with the surface layer on the grain boundary observed with the TEM, it is plausible to assume that the boundary engineering approach optimizes the electrical to thermal conductivity ratio by, rather than counting on the complex crystal structure, introducing a thermoelectrically favorable boundary phase. In following paragraphs, the effects of the boundary phase will be investigated in detail with the focus on 1Na2Rb sample that exhibits the highest ZT at 300 K in Figure 4.2.

4.5 Thermoelectric Properties of Na-and-Rb-treated Samples

Figure 4.4 shows that α curves of all as-treated samples are almost on top of each other while they are slightly higher than the Bulk Reference and even higher than the ingot. Compared with the single alkali salt treatment, the combination of Na and Rb salts does not have an appreciable effect on α . As for ρ in Figure 4.5, treated samples are lower than the Bulk Reference but much higher than the ingot, showing the detrimental effects of grain boundary scattering in electrical conductivity. As a result, the ingot has a PF significantly higher than all polycrystalline samples as shown in Figure 4.6. Among all polycrystalline samples, the 1Na5Rb sample is slightly higher than 1Na2Rb at temperatures above 300K.

Consistent with previous data in Chapter 2, Figure 4.6 shows no sign of any negative impacts on the PF for the addition of Na treatment to Rb treatment, keeping the

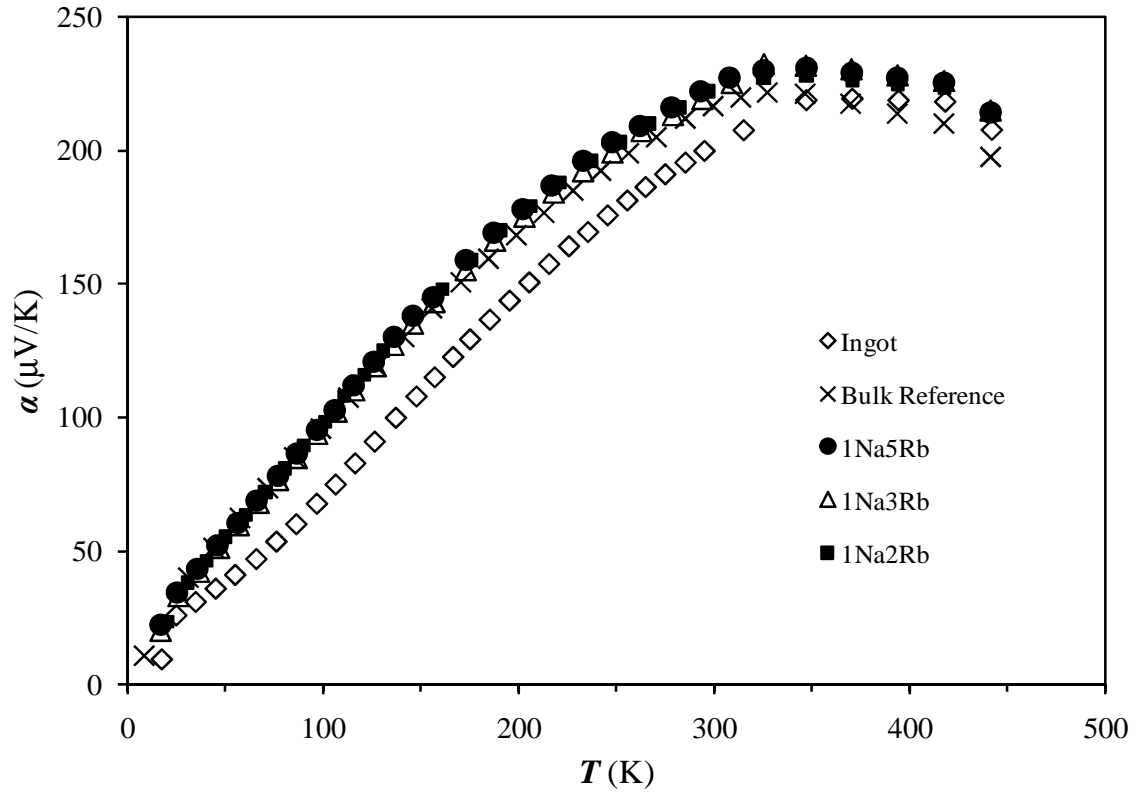


Figure 4.4 The Seebeck coefficient α as a function of temperature T for the as-hydrothermally treated polycrystalline p-type $\text{Bi}_{0.4}\text{Sb}_{1.6}\text{Te}_3$ samples compared with the Ingot and the Bulk Reference.

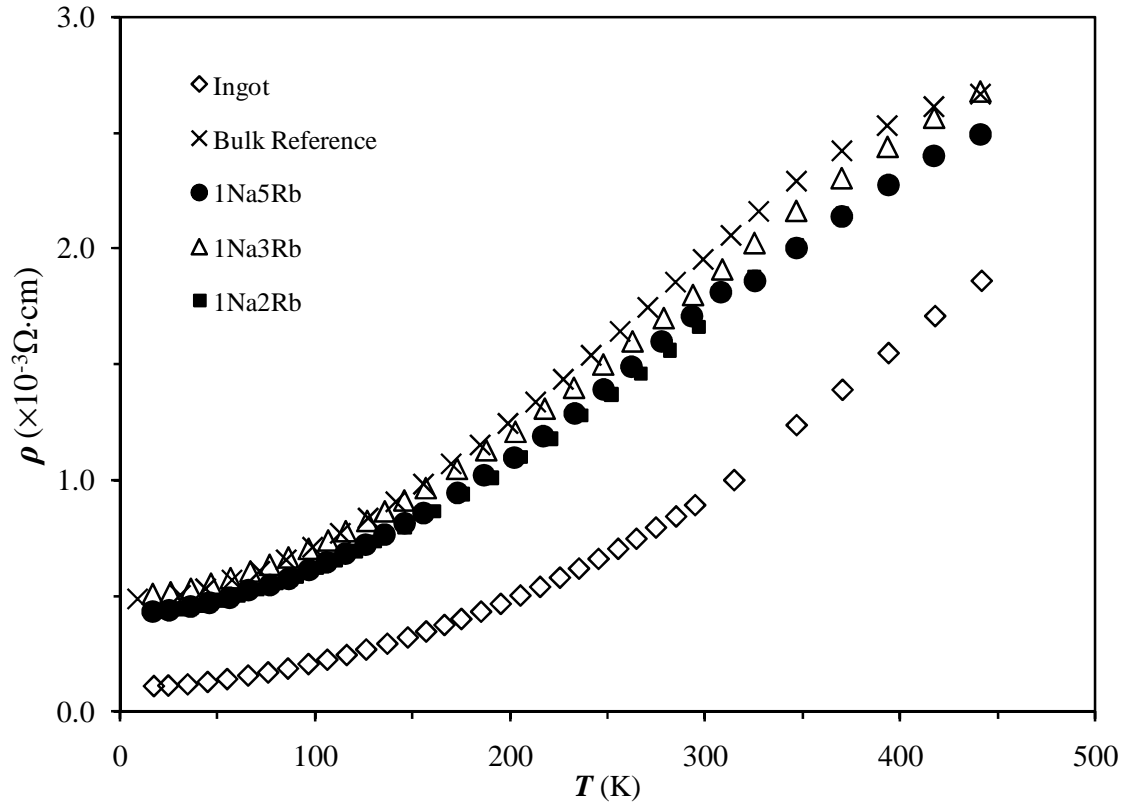


Figure 4.5 The electric resistivity ρ as a function of temperature T for the as-hydrothermally treated polycrystalline p-type $\text{Bi}_{0.4}\text{Sb}_{1.6}\text{Te}_3$ samples compared with the Ingot and the Bulk Reference.

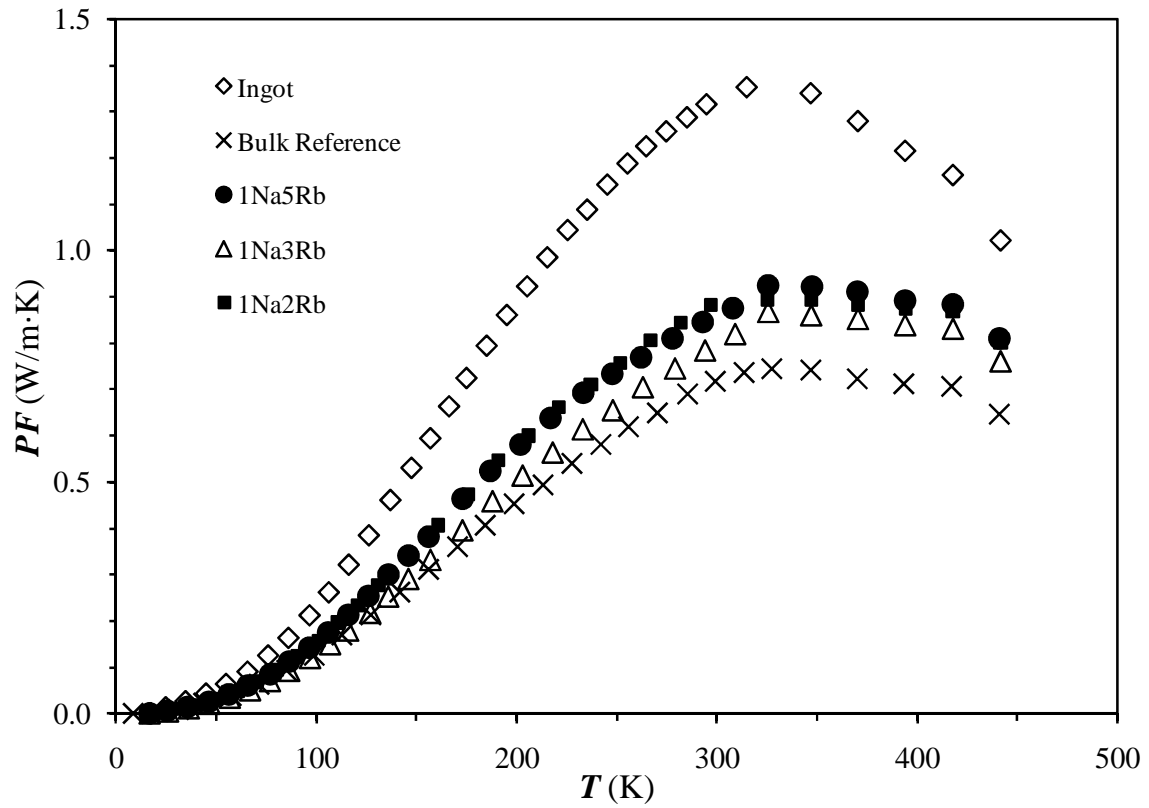


Figure 4.6 The power factor PF as a function of temperature T for the as-hydrothermally treated polycrystalline p-type $\text{Bi}_{0.4}\text{Sb}_{1.6}\text{Te}_3$ samples compared with the Ingot and the Bulk Reference.

PF of the 1Na5Rb sample about the same level as that of Rb-only-treated one. Rb-salt works as if Na-salt does not exist. Recalling Eq. 1.10 where ZT is the ratio of PF to κ , if the Rb-treatment does not interfere with Na treatment's effect on lowering κ , the effects of Na- and Rb- treatments could be considered as decoupled not only at 300K, but throughout the whole temperature region. It would be even better if an optimal ratio of Na to Rb that improves the ZT the most could be found.

Unlike the PF that more characterizes a thermoelectric material's electrical property, κ is a quantity that more describes the thermal transport property. The numerous grain boundaries, due to the scattering of both phonons and electrons, make polycrystalline samples demonstrate overwhelming advantages over the ingot in term of κ as shown in Figure 4.7. For polycrystalline samples, in the temperature region above 200K, 1Na2Rb has the lowest κ , and the tendency is that a higher Na ratio leads to a lower κ . Compared with the minima of κ in the Na-only-treated sample in Figure 2.12, combined Rb-and-Na-treatment further reduces κ for 1Na3Rb and 1Na2Rb samples.

Figure 4.8 shows κ_{lattice} calculated using Eq. 1.14 ~ 1.16. It is clear for polycrystalline samples that κ_{lattice} also has the tendency for temperatures over 300K that the higher Na ratio, the lower the value. Although the ingot has much higher κ , its difference in κ_{lattice} from the Bulk Reference is not as huge, indicating that a large part of κ is contributed by its high carrier concentration and/or mobility, which on the other hand results in its much lower ρ . The comparison with previous Na-only treatment data in Chapter 2 once again demonstrates that not only does the Rb-treatment not weaken but rather enhances Na-treatment's ability to reduce κ and κ_{lattice} .

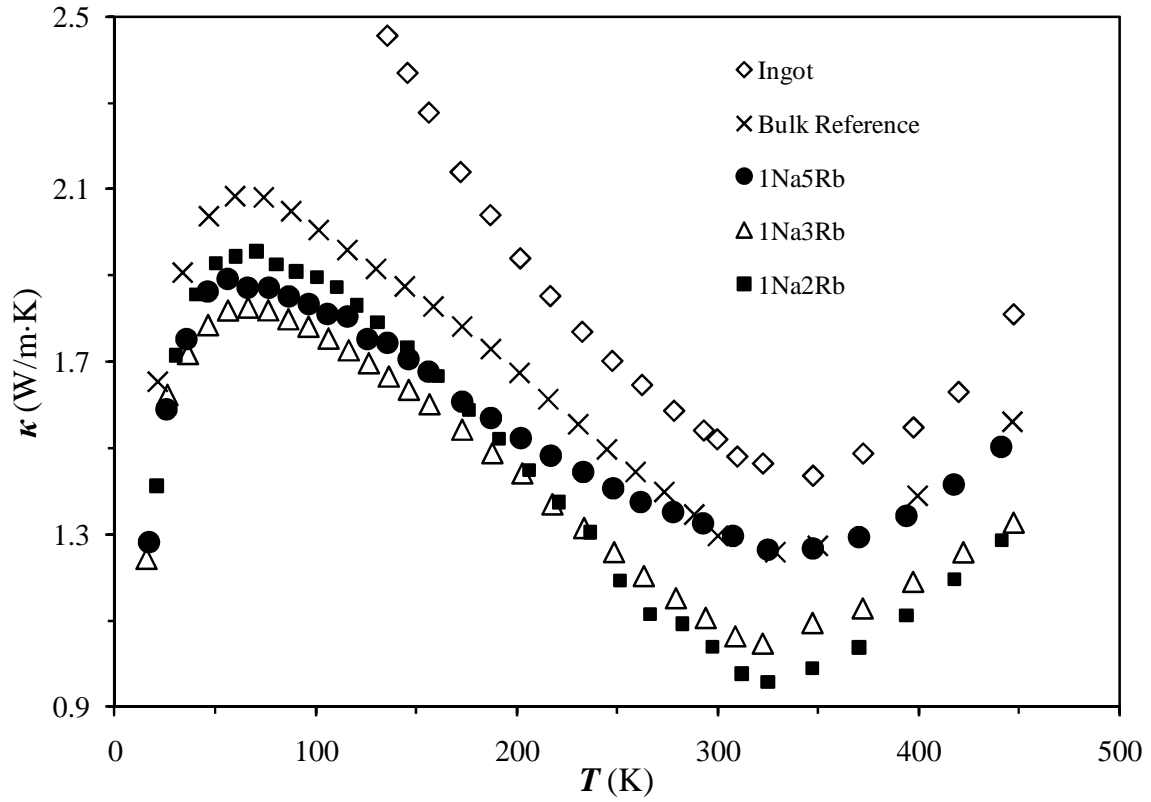


Figure 4.7 The thermal conductivity κ as a function of temperature T for the as-hydrothermally treated polycrystalline p-type $\text{Bi}_{0.4}\text{Sb}_{1.6}\text{Te}_3$ samples compared with the Ingot and the Bulk Reference.

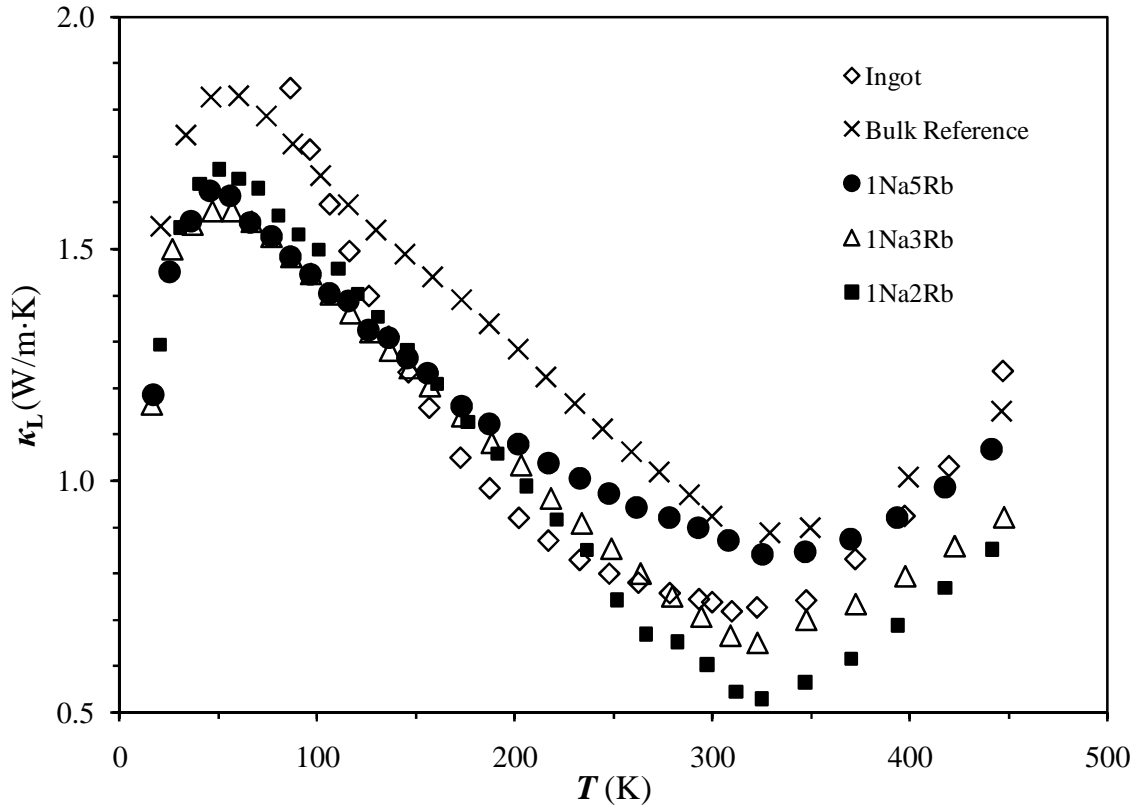


Figure 4.8 The lattice thermal conductivity κ_L as a function of temperature T for the as-hydrothermally treated polycrystalline p-type $\text{Bi}_{0.4}\text{Sb}_{1.6}\text{Te}_3$ samples compared with the Ingot and the Bulk Reference.

As a result shown in Figure 4.9, the ZT of the 1Na2Rb sample, which does not have the highest PF but the lowest κ and κ_{lattice} , peaks at 0.92 at 350K, which is comparable to the original commercial p-type $\text{Bi}_{0.4}\text{Sb}_{1.6}\text{Te}_3$ ingot. Taken into account the ingot's overwhelming superiority in PF over the 1Na2Rb sample, the latter's final breakeven in ZT is attributed to the composite Na- and Rb- treatments' effects on notable reduction in κ . Actually, 1Na2Rb is also the optimal ratio found after more than 40 different recipes were tried.

The data have strengthened the conclusion drawn in Chapter 2 that alkali metal salt hydrothermal treatment can decouple PF and κ for polycrystalline p- Bi_2Te_3 . A close observation under the electron microscope revealed the existence of a transparent Na or Rb rich surface layer surrounding Bi_2Te_3 particles. Therefore, it becomes of interest exactly what the surface layer does to decouple or even enhance the effects of different alkali salts, say Na and Rb, when they are applied simultaneously. Some preliminary investigations have been done in the attempt to find out the underlying mechanisms.

4.6 The Change in n and μ after Hydrothermal Treatment

Figure 4.10 and 4.11 show the behavior of the carrier mobility μ and concentration n , respectively, acquired from Hall measurements performed on the Quantum Design PPMS. The carrier mobility μ of the ingot, which possesses superb electrical properties, is a lot higher than all the polycrystalline samples, treated and untreated, and remains the highest although it decreases rapidly as temperature increases.

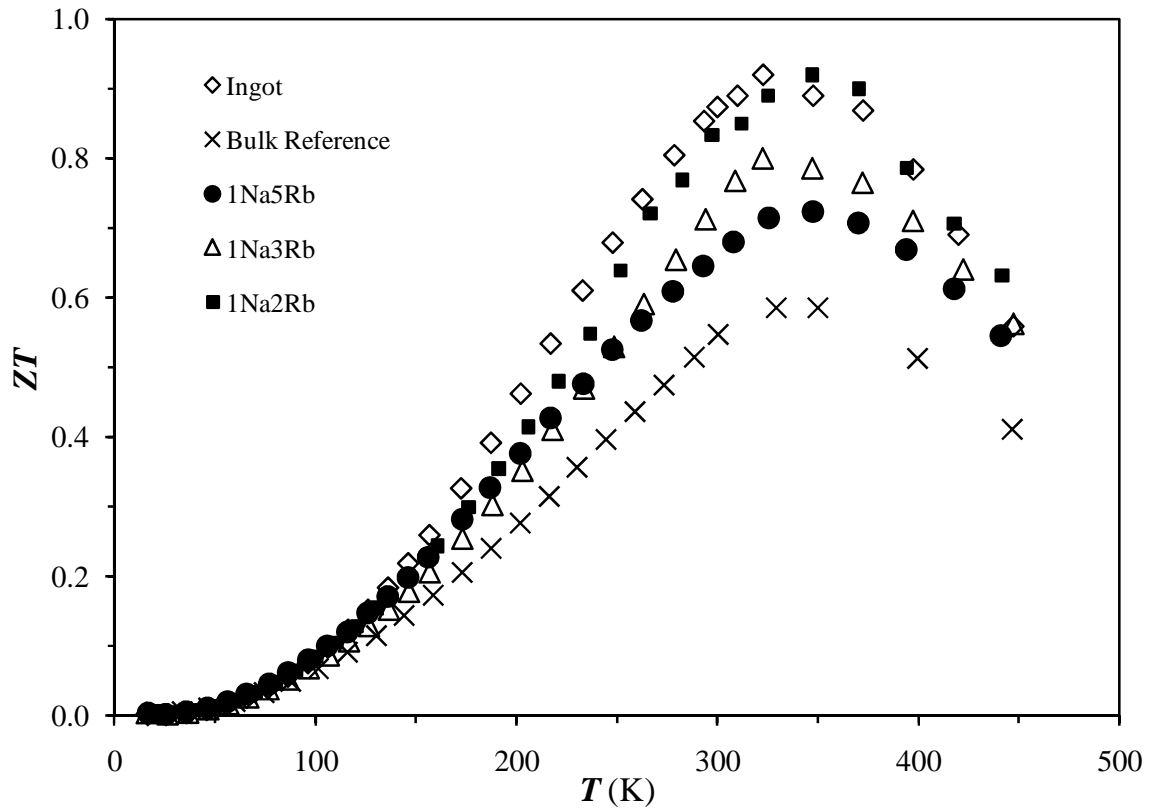


Figure 4.9 The dimensionless figure of merit ZT as a function of temperature T for the as-hydrothermally treated polycrystalline p-type $\text{Bi}_{0.4}\text{Sb}_{1.6}\text{Te}_3$ samples compared with the Ingot and the Bulk Reference.

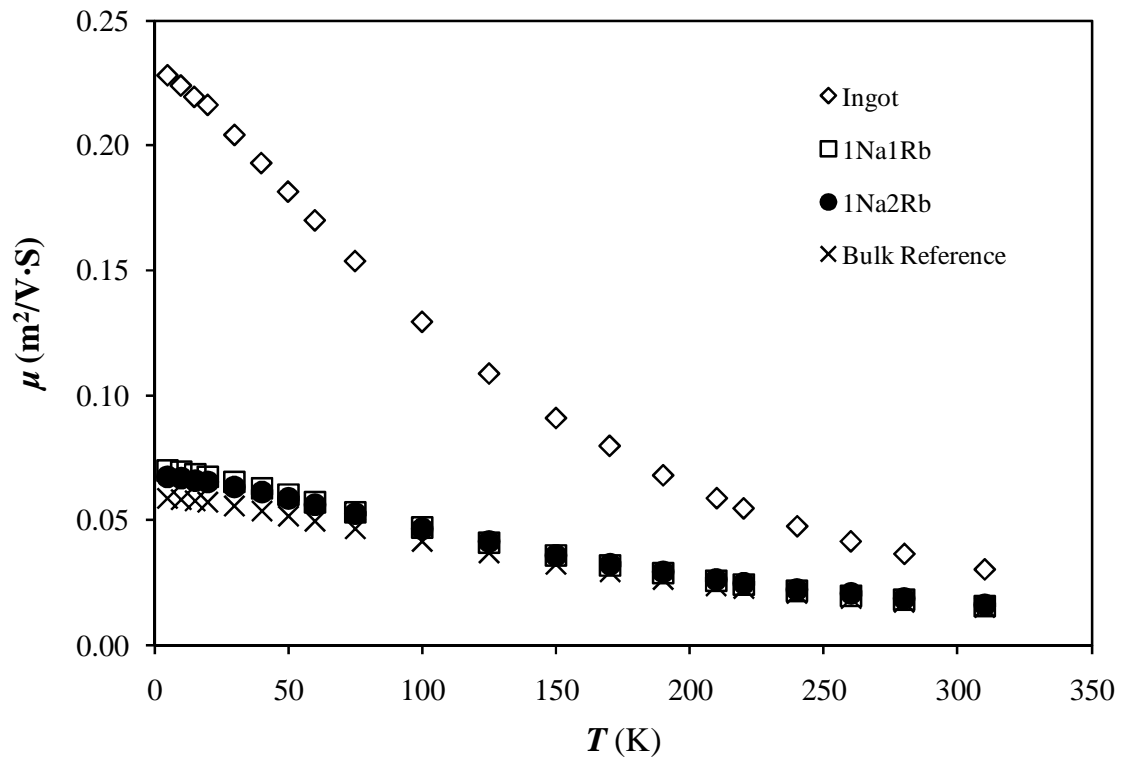


Figure 4.10 The Hall mobility μ as a function of temperature T for the as-hydrothermally treated polycrystalline p-type $\text{Bi}_{0.4}\text{Sb}_{1.6}\text{Te}_3$ samples compared with the Ingot and the Bulk Reference.

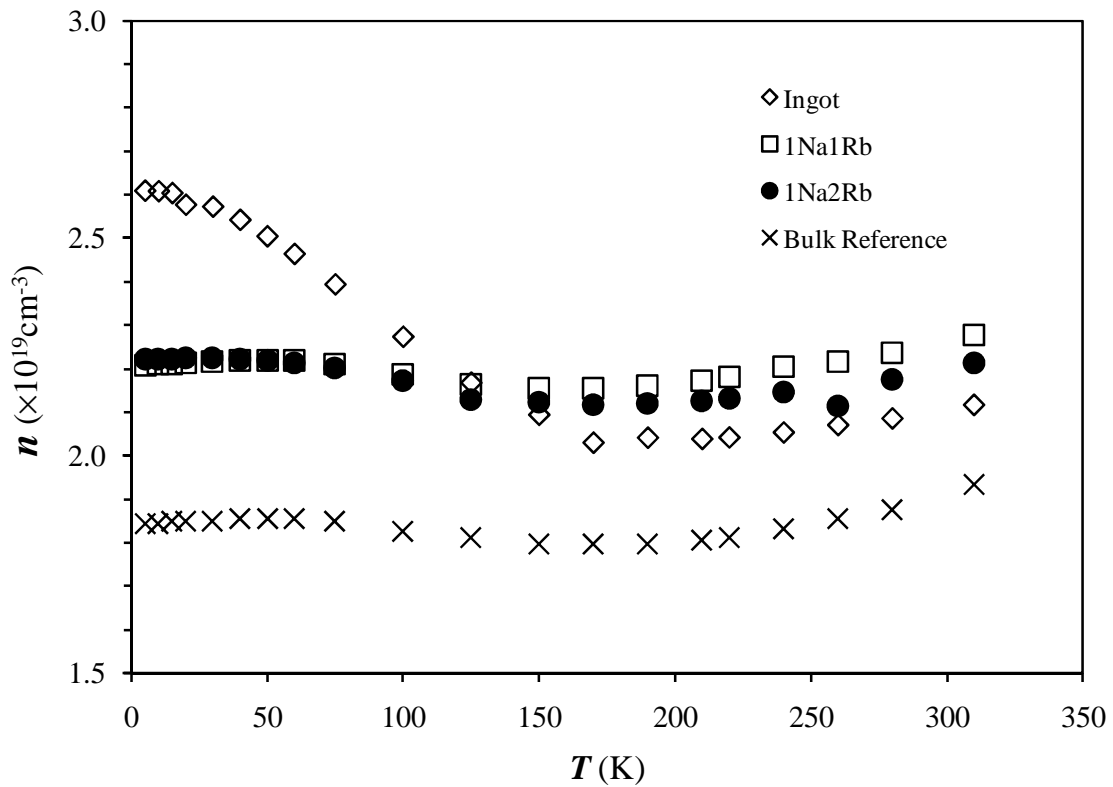


Figure 4.11 The carrier concentration n as a function of temperature T for the as-hydrothermally treated polycrystalline p-type $\text{Bi}_{0.4}\text{Sb}_{1.6}\text{Te}_3$ samples compared with the Ingot and the Bulk Reference.

The μ curves of polycrystalline samples are almost on top of each other, especially when approaching room temperature. However, hydrothermally treated 1Na1Rb and 1Na2Rb both have much higher carrier concentration than the Bulk Reference, and the margin between treated and untreated samples is quite constant over the whole temperature region in Figure 4.11. Above 150 K, those two treated samples even contain larger carrier concentration than the ingot.

The gain for using polycrystalline thermoelectric materials arises from the fact that the grain boundary layer scatters phonons more than electrons. After hydrothermal treatment, although μ remains the same as untreated sample, the increase in n is adequate to compensate the loss of mobility at the grain boundary. Although the composition of the grain boundary layer still remains unclear, the Hall effect measurements have possibly uncovered how this thermoelectrically favorable surface layer, if treated with proper Na to Rb ratio, compete with the commercial ingot.

4.7 Conclusion

In light of the concept of boundary engineering realized through similar hydrothermal treatment techniques as in Chapter 2, but with the combination of Na and Rb salt solutions, the boundary phase has been successfully observed on the surface of p-type Bi_2Te_3 grains, and this surface layer decouples the otherwise inter-related α , ρ , and κ on the same sample, a goal that has been long striven for. The correlation between ZT and σ/κ corroborates that the existence of the grain boundary phase is decoupling the

electrical and thermal transport while retaining the Seebeck coefficient. Unlike approaches in complex crystals, the decoupling is achieved in a way that is potentially applicable to other existing thermoelectric materials.

An optimal molar ratio of Na:Rb = 1:2 has been found to make the polycrystalline sample attain the same ZT as the commercial ingot. Therefore, the hydrothermal treatment enlightens the possible recycling of the large number of p-type $\text{Bi}_{0.4}\text{Sb}_{1.6}\text{Te}_3$ ingot fragments wasted during the mechanical processing of the brittle ingot, which could develop into a more economical and environment-friendly way for manufacturing thermoelectric devices.

5. THE IMPROVEMENT IN COMPATIBILITY FACTOR

5.1 Introduction⁹⁶

A thermoelectric element working between high temperature T_h and low temperature T_c can be postulated to consist of many thin slices of thermoelectric segments as shown in Figure 1. The temperature at each segment is different, and a temperature difference, ΔT_i , is established across the i th thermoelectric segment. As all three thermoelectric properties are temperature dependent, it has its individual α_i , ρ_i , κ_i and, accordingly, ZT_i . The ratio of its efficiency η_i to the Carnot efficiency η_{ci} is called the reduced efficiency, η_{ri} , which is also variable from slice to slice as temperature decreases from T_h at one end to T_c at the other end.

When the total number of thermoelectric slices approaches infinity, ΔT_i approaches zero. The reduced efficiency η_r of each slice is

$$\eta_r = \frac{u \frac{\alpha}{Z} (1 - u \frac{\alpha}{Z})}{u \frac{\alpha}{Z} + \frac{1}{ZT}} \quad (5.1)$$

where u , the relative current density, is the ratio of the electric current density J to the heat flux by thermal conduction defined by

$$u = \frac{J}{k\sqrt{T}} \quad (5.2)$$

The total efficiency η of the whole thermoelectric element is

$$\eta = 1 - \exp\left(-\int_{T_c}^{T_h} \frac{\eta_r(u, T)}{T} dT\right) \quad (5.3)$$

As per Eq. 5.3, η is a function of η_r , which is eventually another function of u . Therefore, the real energy conversion efficiency of a thermoelectric device is not only determined by the ZT value of the material, but also depends on u .

Unlike ZT which is exclusively attributed to the material that makes up the thermoelectric element, u , according to the definition by Eq. 5.2, may vary because J and $\kappa\nabla T$ are subject to changes in the load connected to the thermoelectric element and in the temperatures at the two ends of the element, respectively. Thus, u is a variable that depends on two factors, the material and the operating conditions. In the process of designing a thermoelectric device, the first factor is known beforehand while the second one, however, often contains uncertainty if there is a changeable load and/or temperature across the device.

The u value that maximizes η_r in Eq. 5.1 is defined as the compatibility factor S . The expression of S as a function of T is given by

$$S = \frac{\sqrt{1+ZT} - 1}{\alpha T} \quad (5.4)$$

The largest reduced efficiency η_r would approximately be

$$\eta_{r_{\max}} = \frac{\sqrt{1+ZT} - 1}{\sqrt{1+ZT} + 1} \quad (5.5)$$

Since S is temperature dependent according to Eq. 5.4, each infinitely thin slice whose temperature differs from one another as shown in Figure 1 demands a unique S value once T_h and T_c are fixed at both ends. In order to reach the maximum of the efficiency η in Eq. 5.3, u should strictly keep track of S at every thin slice. In some cases, this can be to some degree achieved by gradually changing the cross section area of a thermoelectric leg along the temperature gradient in order to adjust the ratio of J to $\kappa\nabla T$, which inevitably complicates the design and manufacturing of thermoelectric devices. However, in many cases $u \equiv S$, the condition for the optimum solution to Eq. 5.3, is too difficult to meet, especially when the load connected to a thermoelectric device is variable or the temperatures across the thermoelectric device are changeable. Alternatively, a near-optimum solution is to search for a thermoelectric material with an S that shows a weak temperature dependence so that the deviation of η_r from its theoretical maximum would not be too significant when the condition that u equals S cannot be satisfied all the time.

Previous chapters have shown that the hydrothermal treatment with alkali metal salts is able to improve the ZT of polycrystalline p-type $\text{Bi}_{0.4}\text{Sb}_{1.6}\text{Te}_3$ and the optimal Na to Rb molar ratio of 1:2 yields as high ZT as the commercial ingot, which is a very encouraging result. However, a high ZT , as analyzed above, does not necessarily result in an overall high efficiency in a real thermoelectric device. Therefore, it is important to continue to investigate the effects of the hydrothermal treatment on the compatibility factor S , and the data are presented in detail below.

5.2 The Temperature Dependence of the Compatibility Factor

The compatibility factor S of some selected samples as a function of temperature is shown in Figure 5.1. Over the temperature region from 50K to 350K, the significantly higher hump of the p-type $\text{Bi}_{0.4}\text{Sb}_{1.6}\text{Te}_3$ ingot distinctively makes it out of the polycrystalline samples, among which the untreated Bulk Reference has the flattest hump that almost looks like a plateau. In other word, the ingot demonstrates the strongest temperature dependence of S while the untreated Bulk Reference shows the weakest and hydrothermally treated samples are somewhere in-between. Therefore, in addition to ZT , the hydrothermal treatment with alkali metal salts has improved the polycrystalline samples' temperature dependence of the compatibility factor S .

Based on the analysis in previous paragraphs, a high reduced efficiency η_r relies on both high ZT and appropriate u which, ideally, should equal S . The data presented in Chapter 4 have shown that 1Na2Rb hydrothermally treated sample attains the same ZT value as the commercial ingot. So the comparison between these two specimens in term of efficiency in practical applications would be intriguing.

5.3 The Improvement in Overall Performance

Figures 5.2 and 5.3 are the reduced efficiency η_r of the ingot and the 1Na2Rb sample, respectively, as a function of u and T calculated using Eq. 5.1. The crest line of the η_r dome represents where the theoretical maximum η_r is at every temperature point, and the projection of the crest line onto the T - u plane is equivalent to the S curve shown

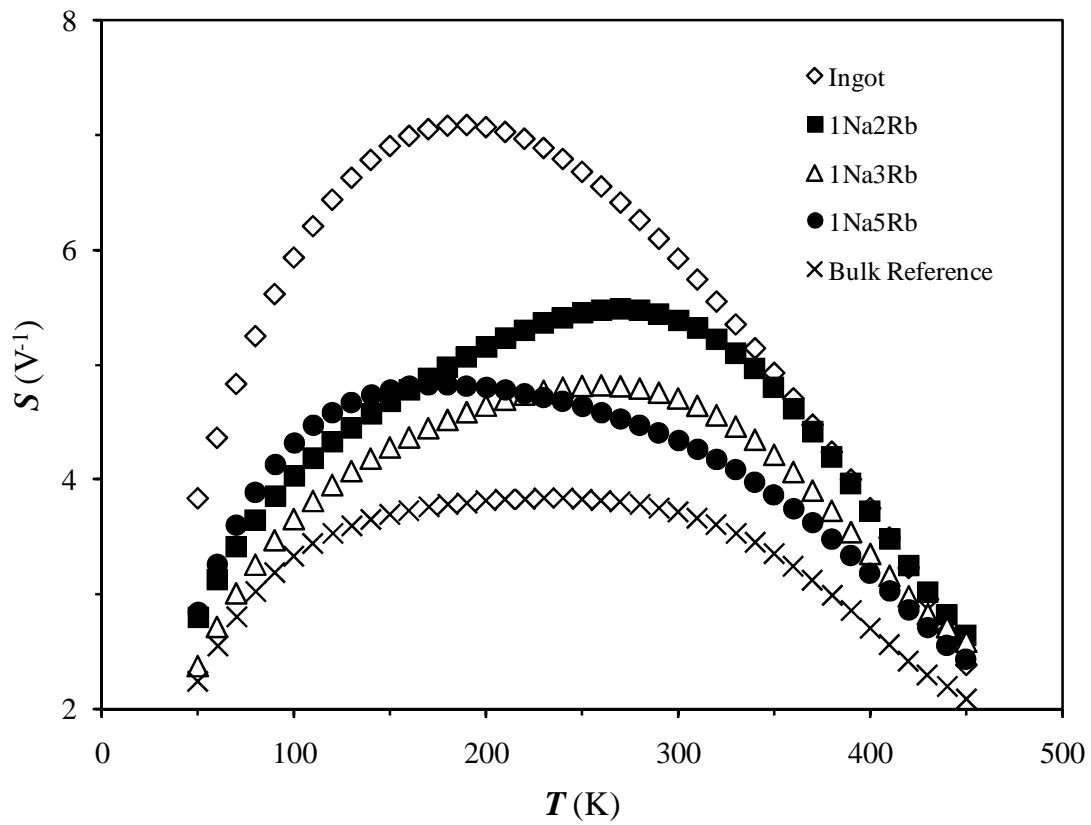


Figure 5.1 The compatibility factor S as a function of temperature T for the as-hydrothermally treated polycrystalline p-type $\text{Bi}_{0.4}\text{Sb}_{1.6}\text{Te}_3$ samples compared with the ingot and the Bulk Reference.

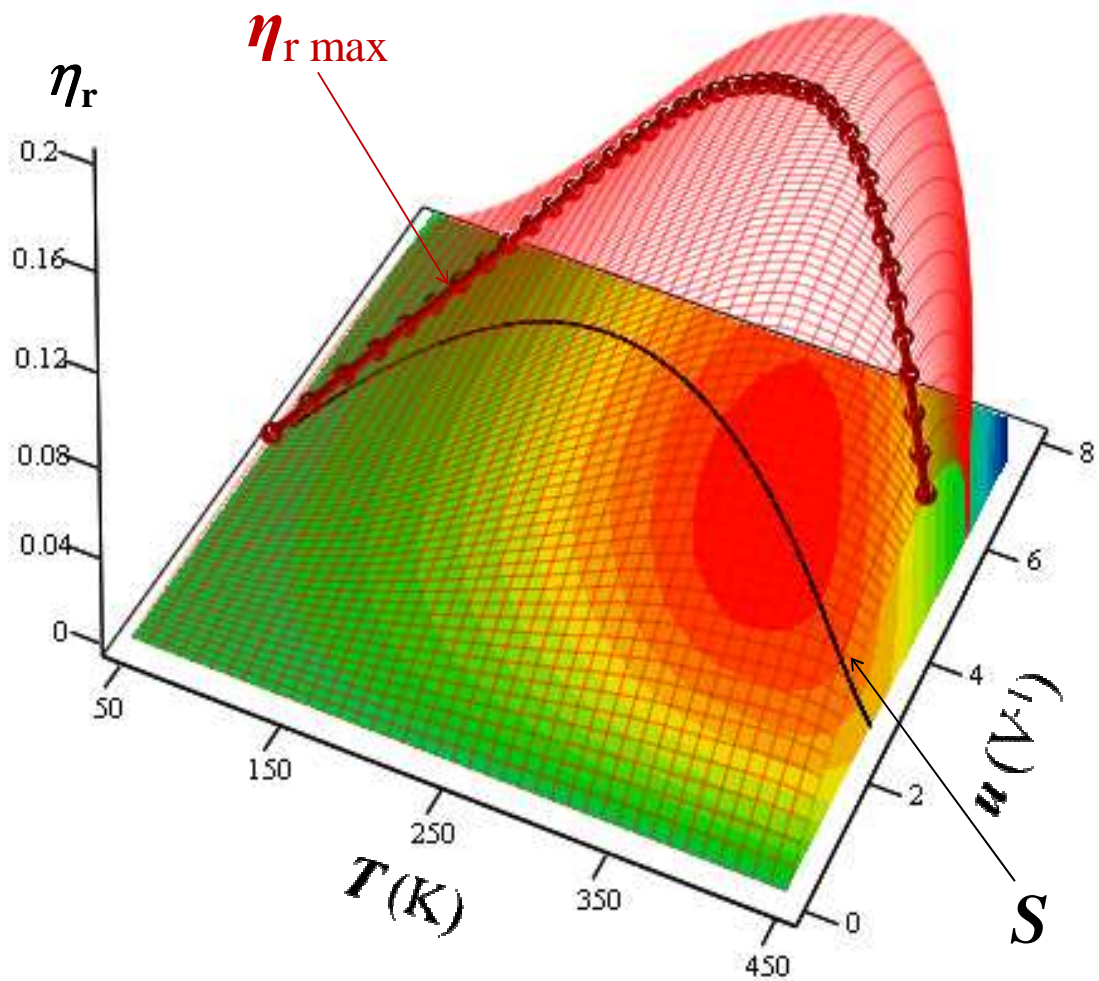


Figure 5.2 The reduced efficiency η_r of the p-type $\text{Bi}_{0.4}\text{Sb}_{1.6}\text{Te}_3$ ingot as a function of temperature T and the relative current density u .

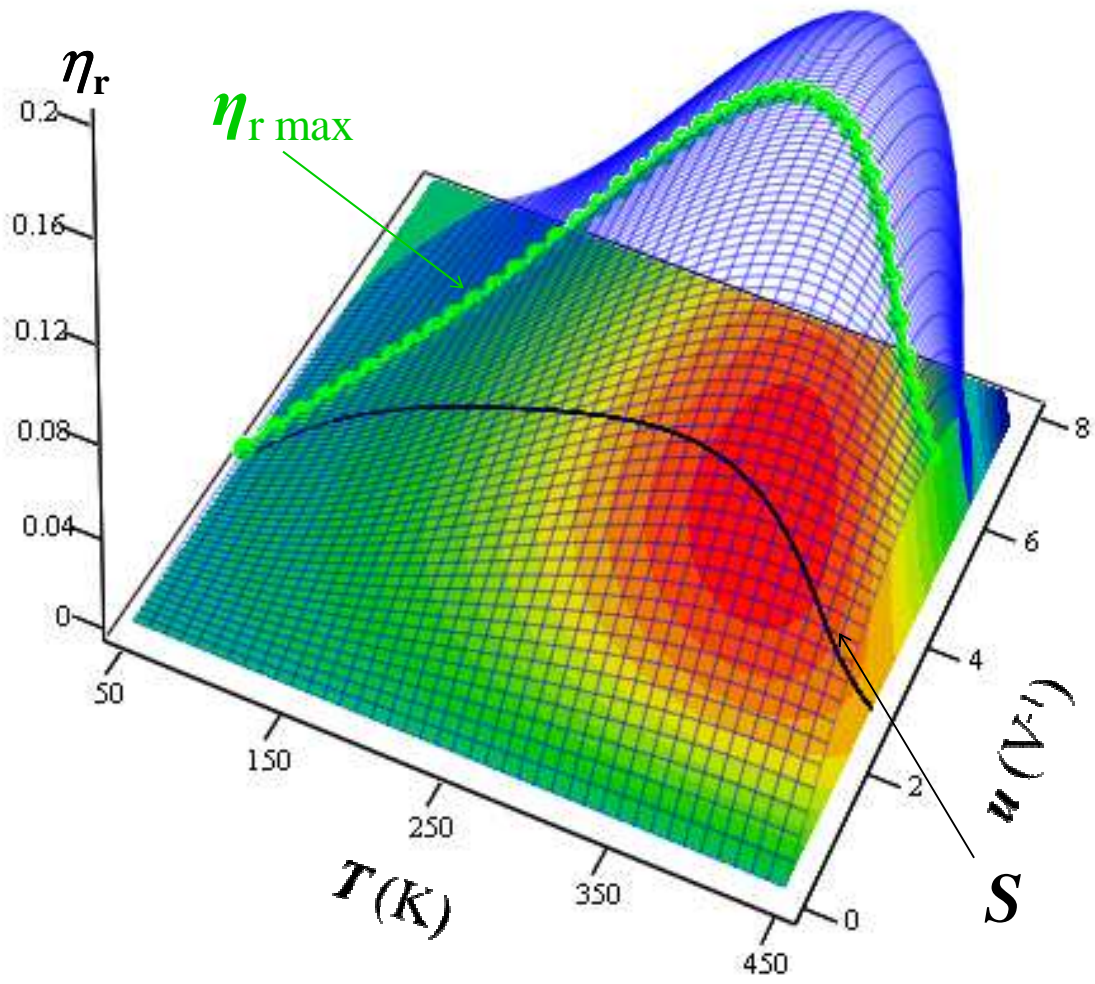


Figure 5.3 The reduced efficiency η_r of the 1Na2Rb-hydrothermally treated p-type $\text{Bi}_{0.4}\text{Sb}_{1.6}\text{Te}_3$ polycrystalline sample as a function of temperature T and the relative current density u .

in Figure 5.1. Therefore, Figures 5.2 and 5.3 provide a more straightforward perspective with which to understand the relationship among η_r , u and S . In the ideal case, if the projection of the crest line of the η_r dome could yield a straight S line on the $T-u$ plane, it would be the easiest for a thermoelectric device to keep track of S , making it work at its best.

Figure 5.4 is a direct comparison in η_r between 1Na2Rb sample and the ingot by placing their η_r domes together. Note that the maximum η_r is solely determined by ZT as stated in Eq. 5.5, these two domes are same in height because the 1Na2Rb and the ingot samples have the same ZT value as shown in Figure 4.9. However, the η_r domes are different in shape, leading to the difference in how complex it is for u in the $T-u$ plane to match S in order to keep η_r on top of the crest line. Judged from the maximum to minimum ratio of the u curves in Figure 5.1, the amplitude in which u varies is less for the 1Na2Rb sample than for the ingot. Therefore, if u deviates from S , or, in another words, if a thermoelectric device works under a non-optimal condition, the device made of 1Na2Rb sample may have better performance than that made of the ingot despite their same maximum ZT values as shown in Figure 4.9.

Suppose S_{Middle} is the S value at the midpoint temperature of a thermoelectric segment working between T_h and T_c . Figure 5.5 shows the comparison in the total efficiency η between the thermoelectric segments made of the 1Na2Rb treated sample and the ingot as a function of the deviation of u from S_{middle} . When the deviation is within $\pm 50\%$, the 1Na2Rb sample often has a higher total efficiency than the ingot for T_c and T_h values of 50K and 450K, respectively. And it always has a higher total efficiency than the

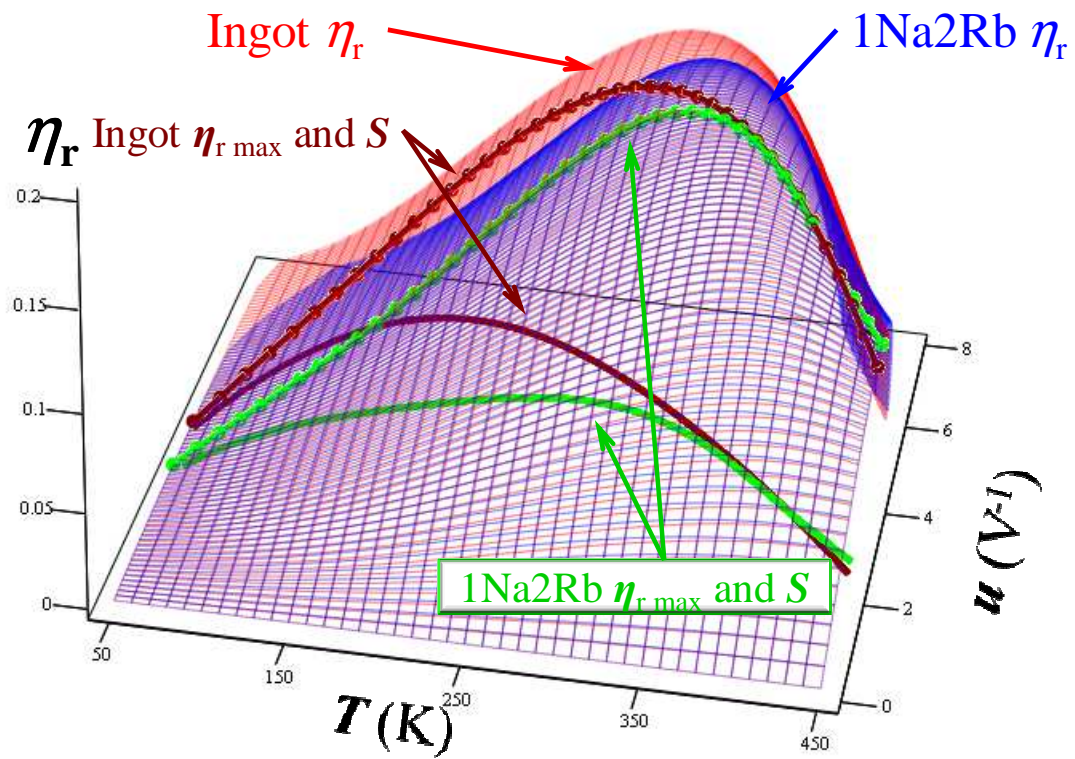


Figure 5.4 The comparison of the reduced efficiency η_r between the p-type $\text{Bi}_{0.4}\text{Sb}_{1.6}\text{Te}_3$ ingot and 1Na2Rb-hydrothermally treated sample.

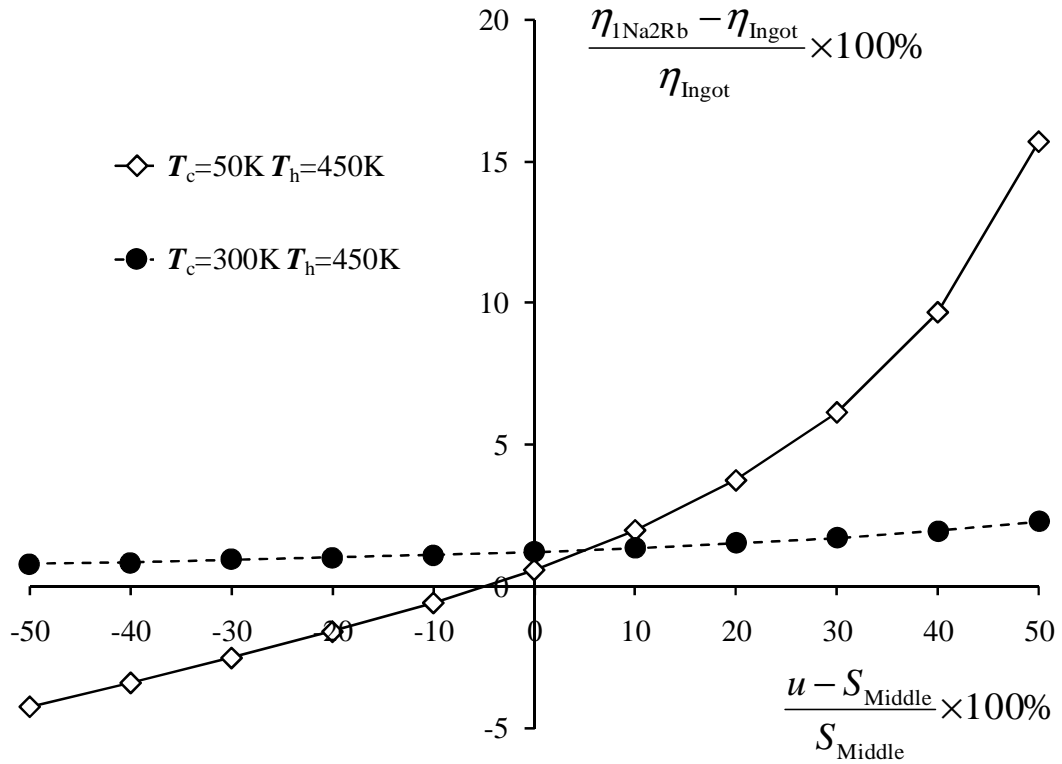


Figure 5.5 The percent difference between the total efficiency of the 1Na2Rb-treated sample, η_{1Na2Rb} , and that of the ingot, η_{ingot} , when the relative current density u deviates from S_{middle} , the compatibility factor value at the midpoint temperature for a thermoelectric element sandwiched between cold and hot ends, T_c and T_h , respectively.

ingot for T_c and T_h values of 300K and 450K, respectively, which are typical operating temperatures for Bi_2Te_3 used in waste heat recovery.

When a thermoelectric device is designed, it is more often for one to know the working temperatures at both ends of the device than the load resistance connected to the device. When a load is connected in a circuit as shown in Figure 1.9 (a), the current equals the ratio of the thermoelectric electric-motive force to the sum of the load resistance and the internal resistance of the thermoelectric device. The resistivity curves in Figure 4.5 have shown that the ingot has much lower resistivity than any polycrystalline samples, treated or untreated. Therefore, the ingot, generally speaking, has smaller internal resistance than the 1Na2Rb sample, which makes the ingot behave more like a voltage source while the other more like a current source. When the load resistance is variable in the circuit, a current source is able to stabilize the current so that the current density J in Eq. 5.2 is constant and consequently u is constant. Although the 1Na2Rb does not work as a perfect current source, its large internal resistance makes u change less than it would in the ingot. Thus, the 1Na2Rb sample is advantageous over the ingot in applications that consist of variable loads.

5.4 Conclusion

Although the figure of merit ZT weighs the most in determining the energy conversion efficiency of a thermoelectric device, the real efficiency of the device is also dependent on the compatibility factor S . Not only can hydrothermal treatment with alkali

metal salts improve the ZT of p-type $\text{Bi}_{0.4}\text{Sb}_{1.6}\text{Te}_3$ polycrystalline samples, but it also weakens the temperature dependence of S of as-treated samples. As a result of the lower temperature dependence of S , the $1\text{Na}2\text{Rb}$ treated polycrystalline sample, which has attained the same ZT value as the ingot, can have overall higher efficiency when operated under non-optimal conditions.

6. SUMMARY

In order to achieve the goal of “PGEC”, one of the challenging tasks of current thermoelectric study is to decouple the inter-relation between ρ and κ , i.e., to minimize κ at the cost of a small or even no increase in ρ . Such efforts have culminated to two prongs: one is toward “forcibly engineered” low dimension systems such as superlattice and quantum dot or well systems,⁹⁷⁻¹⁰⁴ whereas the other persists in bulk materials, for example, the partially filled skutterudite,^{36,105-107} clathrate systems^{108,109} and Zn_4Sb_3 ¹¹⁰.

Most existing thermoelectric materials are in form of polycrystals and the grain boundaries in polycrystalline system are by nature advantageous over single crystals in terms of lower κ . Therefore, a novel strategy of improving thermoelectric performance has been adopted in light of “grain boundary engineering”^{111,112}.

It has been shown in this dissertation that “grain boundary engineering” via the hydrothermal treatment with alkali metal salts can improve both the figure of merit ZT and compatibility factor S of p-type $\text{Bi}_{0.4}\text{Sb}_{1.6}\text{Te}_3$ polycrystalline samples. Compared with other methods, the hydrothermal treatment herein introduced has the following advantages:

1. Very low cost. The alkali metal salts are very cheap and common. Moreover, only a small amount of such chemicals are needed for each treatment.
2. Low energy consumption and short duration for sample preparation. For this hydrothermal treatment technique, it requires relatively low temperature (100 ~ 300°C)

and a relatively short duration (~ 48hours), which could save costs in term of both money and time.

3. Simple technical route without complicated or expensive equipment involved. Autoclaves and ball-milling machines are commonly used production equipment and methods, which also enables the possibility of large-scale industry production and application.
4. Directly makes use of industrial waste materials. During the growth procedure of commercial Bi_2Te_3 ingot, both ends of an ingot go to waste due to composition fluctuation. In addition, as a result of the ingot's brittle nature, there would be an additional 30% waste that comes into being during the subsequent processing such as cutting, assembling and so on. Tellurium sources are rapidly becoming scarce, and its unit price has skyrocketed from \$13/Kg in 2004 to \$215/Kg in 2008.¹¹³ Therefore, the reuse of otherwise wasted ingot would increase Bi_2Te_3 thermoelectric modules' competitiveness on the market.
5. Fully take advantage of polycrystalline materials' large flexibility in varying composition, which allows a greater degree of freedom in order to make functionally gradient-element materials, i.e., a composition gradient along the length of the sample. Distinct from the previous concepts, the concentration variation of alkali elements occurs in the surface layer rather than in the bulk, so it is easier to achieve and control, as simple as stacking the powder of a desired concentration and desired thickness. After the hot-pressing process, the polycrystalline nature guarantees they are also easy to machine. Bear in mind that Bi_2Te_3 ingots are quite well aligned, so the

anisotropy in crystal structure causes them to be more difficult to shape. Again, the shreds and waste powder can be recycled with the hydrothermal treatment.

6. The thermoelectric performance is improved in an inhomogeneous system with the matrix isolated by a surface layer. In principle, it makes this technique easy to apply on other systems as well, seeking for a broader application of the process. The preliminary application of the hydrothermal treatment on PbTe system has been proven successful.
7. In the past several years, several results have been reported on obtaining significant property improvement, whereas these reports mainly involved thermoelectric quantum dots and super-lattice thin films, which are difficult to be used in the routine industrial applications. Considering the feasibility of large-scale production, researchers and industry still need to rely on the bulk thermoelectric materials. The present study is a bulk material investigation, and is still far from complete, even in conventional materials such as Bi_2Te_3 .

A great effort has been spent to ascertain the exact composition and structure of the surface layer formed on the grain boundaries after the hydrothermal treatment. Following are some features of this layer:

1. This surface layer forms a thermoelectrically favorable grain boundary phase that is able to improve ZT by providing extra carriers which compensate carriers' loss in the mobility. A surface layer as insignificant in amount as it is can greatly alter the transport properties of phonons and electrons in the bulk material.

2. Benefitted from the improvement in ZT whereas less temperature dependence of the compatibility factor S due to such surface layer, the thermoelectric device is more adaptive to variable working conditions.
3. Although the SAED attains a new square pattern from this layer, it is not considered to have long range ordering as indicated by some other techniques such as the XRD, HRTEM, etc.
4. It has been found to mainly consist of light elements and accounts for only a very small fraction of the sample mass.
5. It is not stable at high temperature.

Unfortunately, by the time of the completion of this dissertation, there are a lot of questions that remain unanswered about the exact structure and composition of the surface layer. Therefore, ascertaining the structure and composition of this thermoelectrically favorable layer would be the focus of future work. SIMS (secondary ion mass spectrometry) is a very sensitive technique to analyze the composition of solid surfaces. Therefore, it will be considered in the future. It has also been found that the deterioration in the Seebeck coefficient of n-type polycrystalline Bi_2Te_3 samples after the hydrothermal treatment with alkali metal salts was too much to be compensated by the decrease in the thermal conductivity. Although this is a discouraging result, follow-up investigations on it may help discover how this surface layer affects the transport properties in the Bi_2Te_3 system. In addition, hydrothermal treatment with other families of elements may also be an option for future work.

The hydrothermal treatment involves chemical reactions and/or physical changes under high temperature and high pressure. Moreover, such reactions and/or changes would continue in the process of subsequent densification of powder into pellets with hot-pressing during which high temperature and high pressure present. The research on hydrothermally treated polycrystalline $\text{Pb}_{0.75}\text{Sn}_{0.25}\text{Te}$ shows that⁸¹ different hot-pressing conditions can significantly affect the formation of the nanoscaled grain boundary, which, combined with the selection of different alkali metal salts for treatment, leads to differences in thermoelectric performance. Accordingly, “grain boundary engineering” via hydrothermal treatment actually includes a series of reactions and/or changes occurring during the treatment itself and post-treatment such as hot-pressing. This dissertation does not address the influence of post-treatment on samples’ properties, and follow-up investigations on that would make this hydrothermal treatment technique more comprehensive. In recent years, the SPS (spark plasma sintering) technique has been more and more employed for densification than the conventional hot-pressing. It takes a much shorter time for the SPS to densify powders and this is assumed to help nanostructures survive. Therefore, using SPS instead of hot-pressing to solidify treated powders would also be a topic of interest.

REFERENCES

1. D. M. Rowe, *Renewable Energy* **16**, 1251 (1999).
2. T. M. Tritt and M. A. Subramanian, *MRS Bulletin* **31**, 188 (2006).
3. J. Yang and T. Caillat, *MRS Bulletin* **31**, 224 (2006).
4. D. M. Rowe ed., *CRC Handbook of Thermoelectrics* (CRC Press, Boca Raton, FL, 1995).
5. G. S. Nolas, J. Sharp and J. Goldsmid, *Thermoelectrics: Basic Principles and New Materials Developments* (Springer, New York, 2001).
6. D. M. Rowe, *Thermoelectric Handbook: Macro to Nano*, (CRC Press, Boca Raton, FL, 2006).
7. T. J. Seebeck, *Abh. K. Akad. Wiss.*, Berlin, p. 265 (1823).
8. V. L. Ginzburg, *J. Phys. USSR*. **8**, 148 (1944).
9. J. C. Peltier, *Ann. Chem.* **56**, 371 (1834).
10. W. Thomson, *Mathematical and Physical Papers*, Cambridge, **1**, 558 (1882).
11. W. Thomson, *Mathematical and Physical Papers*, Cambridge, **2**, 306 (1882).
12. E. Atenkirsch, *Physikalische Zeitschrift* **10**, 560 (1909).
13. E. Atenkirsch, *Physikalische Zeitschrift* **12**, 920 (1911).

14. M. V. Vedernikov and E. K. Iordanishvili, *Proc. 17th International Conference of Thermoelectrics* (IEEE, Piscataway, NJ, 1998).
15. M. H. Ettenberg, W. A. Jesser and F. D. Rosi, *Proc. 15th Int. Conf. on Thermoelectrics* (IEEE, Piscataway, NJ, 1996).
16. H. J. Goldsmid, *Proc. 17th International Conference of Thermoelectrics*, (IEEE, Piscataway, NJ, 1998).
17. A. F. Ioffe, *Semiconductor Thermoelements and Thermoelectric Cooling*, (Infosearch, London, 1957).
18. G. J. Snyder and E. S. Toberer, *Nature Materials* **7**, 106 (2008).
19. S. Bhattacharya, PhD Dissertation, Clemson University, SC 29634, USA (2003).
20. T. M. Tritt, *Science* **283**, 804 (1999).
21. F. J. Disalvo, *Science* **285**, 703 (1999).
22. X. B. Zhao, X. H. Ji, Y. H. Zhang T. J. Zhu, J. P. Tu and X. B. Zhang, *Appl. Phys. Lett.* **86**, 062111 (2005).
23. X. A. Fan, J. Y. Yang, R. G. Chen, W. Zhu and S. Q. Bao, *Mat. Sci. Eng.: A* **438-440**, 190 (2006).
24. X. Tang, W. Xie, H. Li, W. Zhao and Q. Zhang, *Appl. Phys. Lett.* **90**, 012102 (2007).
25. X. H. Ji, J. He, Z. Su, N. Gothard and T. M. Tritt, *J. Appl. Phys.* **104**, 034907 (2008).

26. R. R. Heikes and R. W. Ure, *Thermoelectricity: Science and Engineering* (Interscience, New York, 1961).
27. F. D. Rosi, E. F. Hockings and N. E. Lindenblad, *RCA Rev.* **22**, 82 (1961).
28. C. Wood, *Rep. Prog. Phys.* **51**, 459–539 (1988).
29. Y. Gelbstein, Z. Dashevsky and M. P. Dariel, *Physica B* **363**, 196–205 (2005).
30. I. B. Cadoff and E. Miller ed., *Thermoelectric Materials and Devices*, (Reinhold, New York, 1960).
31. B. C. Sales, D. Mandrus, B. C. Chakoumakos, V. Keppens and J. R. Thompson, *Phys. Rev. B* **56**, 15081 (1997).
32. D. T. Morelli, G. P. Meisner, B. Chen, S. Hu and C. Uher, *Phys. Rev. B* **56**, 7376 (1997).
33. G. S. Nolas, M. Kaeser, R. T. Littleton IV and T. M. Tritt, *Appl. Phys. Lett.* **77**, 1855 (2000).
34. L. D. Chen, T. Kawahara, X. F. Tang, T. Goto, T. Hirai, J. S. Dyck, W. Chen and C. Uher, *J. Appl. Phys.* **90**, 1864 (2001).
35. G. A. Lamberton, Jr., S. Bhattacharya, R. T. Littleton IV, M. A. Kaeser, T. M. Tritt, J. Yang and G. S. Nolas, *Appl. Phys. Lett.* **80**, 598 (2002).
36. J. Y. Peng, P. N. Alboni, J. He, B. Zhang, Z. Su, T. Holgate, N. Gothard and T. M. Tritt, *J. Appl. Phys.* **104**, 053710 (2008).

37. J. Y. Peng, J. He, Z. Su, P. Alboni, S. Zhu and T. M. Tritt, *J. Appl. Phys.* **105**, 084907 (2009).
38. J. Pierre, R. V. Skolozdra and Y. V. Stadnyk, *J. Magn. Magn. Mater.* **128**, 93 (1993).
39. T. M. Tritt, *Recent Trends in Thermoelectric Materials Research I, Semiconductors and Semimetals*, Vol. 70 (Academic, New York, 2001).
40. S. Bhattacharya, A. L. Pope, R. T. Littleton IV, T. M. Tritt and V. Ponnambalam, Y. Xia and S. J. Poon, *Appl. Phys. Lett.* **77**, 2476 (2000).
41. S. Bhattacharya, T. M. Tritt, Y. Xia, V. Ponnambalam, S. J. Poon and N. Thadhani, *Appl. Phys. Lett.* **81**, 43 (2002).
42. Q. Shen, L. Chen, T. Goto and T. Hirai, *Appl. Phys. Lett.* **79**, 4165 (2002).
43. C. Wood, *Energy Conversion Manage.* **24**, 331 (1984).
44. S. R. Brown, S. M. Kauzlarich, F. Gascoin and G. J. Snyder, *Chem. Mater.* **18**, 1873 (2006).
45. S. M. Kauzlarich, S. R. Brown and G. J. Snyder, *Dalton Trans.*, 2099 (2007).
46. C. Yu, T. J. Zhu, S. N. Zhang, X. B. Zhao, J. He, Z. Su and T. M. Terry, *J. Appl. Phys.* **104**, 013705 (2008).
47. D. A. Wright, *Nature* **181**, 834 (1958).
48. D. Kusano and Y. Hori, *J. Jpn. Inst. Met.* **66**, 1063 (2002).

49. P. W. Zhu, Y. Imai, Y. Isoda, Y. Shinohara, X. Jia and G. Zou, *J. Phys.: Condens. Matter.* **17**, 7319 (2005).
50. P. F. P. Poudeu, J. D'Angelo, H. Kong, A. Downey, J. L. Short, R. Pcionek, T. P. Hogan, C. Uher and M. G. Kanatzidis, *J. Am. Chem. Soc.* **128**, 14347 (2006).
51. M. S. Desselhaus, G. Chen, M. Y. Tang, R. G. Yang, H. Lee, D. Z. Wang, Z. F. Ren, J. P. Fleurial and P. Gogna, *Adv. Mater.* **19**, 1043 (2007).
52. T. C. Harman, M. P. Walsh, B. E. LaForge and G. W. Turner, *J. Electron. Mater.* **34**, L19 (2005).
53. T. M. Tritt, H. Böttner and L. D. Chen, *MRS Bulletin* **33**, 366 (2008).
54. A. W. Allen, *Laser Focus World* **33**, S15 (1997).
55. A. I. Hochbaum, R. Chen, R. D. Delgado, W. Liang, E. C. Garnett, M. Najarian, A. Majumdar and P. Yang, *Nature* **451**, 163(2008).
56. K. Hsu, S. Loo, F. Guo, W. Chen, J. S. Dyck, C. Uher, T. Hogan, E. K. Polychroniadis and M. G. Kanatzidis, *Science* **303**,818(2004).
57. D. Y. Chung, T. Hogan, P. Brazis, M. Rocci-Lane, C. Kannewurf, M. Bastea, C. Uher and M. G. Kanatzidis, *Science* **287**,1024(2000).
58. R. Venkatasubramanian, E. Siivola, T. Colpitts and B. O'Quinn, *Nature* **413**, 597(2001).
59. T. M. Tritt, B. Zhang, N. Gothard, J. He, X.H. Ji, D. Thompson and J. W. Kolis, *Mater. Res. Soc. Symp. Proc.*, 0886-F02-01.1 (2006).

60. B. Poudel, Q. Hao, Y. Ma, Y. Lan, a. Minnich, B. Yu, X. Yan, D. Wang, A. Muto, D. Vashaee, X. Chen, J. Liu, M. S. Dresselhaus, G. Chen and Z. F. Ren, *Science* **320**, 634(2008).
61. A. C. Masset, C. Michel , A. Maignan, M. Hervieu, O. Toulemonde, F. Studer and B. Raveau, *Phys. Rev. B* **62**, 166 (2000).
62. W. Koshibae, K. Tsutsui, and S. Maekawa, *Phys. Rev. B* **62**, 11 (2000).
63. F. Gascoin, S. Ottensmann, D. Stark, S. M. Haïle and G. J. Snyder, *Adv. Func. Mater.* **15**, 1860 (2005).
64. M. Shimi, Heterogeneous materials I: Linear Transport and Optical Properties (Springer, New York, 2003).
65. D. J. Bergman and O. Levy, *J. Appl. Phys.* **70**, 6821 (1991).
66. A. L. Pope, R. T. Littleton IV and T. M. Tritt, *Rev. Sci. Instrum.* **72**, 3129 (2110).
67. <http://www.ulvac.com/thermal/zem.asp>.
68. A. L. Pope, B. Zawilski and T. M. Tritt, *Cryogenics* **41**, 725 (2001).
69. <http://www.netzsch-thermal-analysis.com/en/products/detail/pid,26.html>.
70. <http://www.netzsch-thermal-analysis.com/en/products/detail/pid,4.html>.
71. H. V. Keer, *Principles of the Solid State* (John Wiley & Sons, New York, 1993).
72. R. T. Delves, A. E. Bowley, D. W. Hazelden and H. J. Goldsmid, *Proc. Phys. Soc.* **78**, 838 (1961).

73. I. J. Ohsugi, T. J. Kojima, M. Sakata, M. Yamanashi and I. A. Nishida, *J. Appl. Phys.* **76**, 2235 (1994).
74. J. Nagao, M. Ferhat, E. Hatta and K. Mukasa, *Phys. Stat. Sol. (b)* **219**, 347 (2000).
75. D. J. Ryden, *J. Phys. C: Solid St. Phys.* **4**, 1193 (1971).
76. E. J. Gonzalez, J. E. Blendell, J. P. Cline, J. J. Ritter, P. Maruthamuthu, E. H. Nelson and S. B. Horn, *J. Mater. Res.* **13**, 766 (1998).
77. X. H. Ji, X. B. Zhao, Y. H. Zhang, B. H. Lu and H. L. Ni, *J. Alloys Comp.* **387**, 282 (2005).
78. <http://jbweld.net/products/jbweld.php>.
79. <http://www.qdusa.com/products/ppms.html>.
80. X. H. Ji, J. He, Z. Su, N. Gothard and T. M. Tritt, *J. Appl. Phys.* **104**, 034907 (2008).
81. X. H. Ji, B. Zhang, Z. Su, T. Holgate, J. He and T. M. Tritt, *Phys. Status. Solidi A* **206**, 221 (2009).
82. J. R. Wiese and L. Muldrew, *J. Phys. Chem. Solids.* **15**, 13 (1960).
83. Y. Feutelais, B. Legendre, N. Rodier and V. Agafonov, *Mat. Res. Bull.* **28**, 591 (1993).
84. S. K. Mishra, S. Satpathy and O. Jepsen, *J. Phys.: Condens. Matter.* **9**, 461 (1997).
85. JCPDS-ICDD 1999, International Centre for Diffraction Data, 12 Campus Boulevard, Newtown Square, PA 19073-3273, USA.

86. V. A. Greanya, W. C. Tonjes, R. Liu, C. G. Olsen, D. -Y. Chung and M. G. Kanatzidis, *Phys. Rev. B* **62**, 16425 (2000).
87. J. R. Drabble and C. H. L. Goodman, *J. Phys. Chem. Solids* **5**, 142 (1958).
88. Z. Ding, L. Viculis, J. Nakawatase and R. B. Kaner, *Adv. Mater.* **13**, 797 (2001).
89. J. Bludská, K. Karamazov, J. Navrátil, I. Jakubec and J. Horák, *Solid State Ionics* **171**, 251 (2004).
90. X. B. Zhao, X. H. Ji, Y. H. Zhang, G. S. Cao and J. P. Tu, *Appl. Phys. A* **80**, 1567 (2005).
91. S. Sh Kakhramanov, *Inorg. Mater.* **44**, 13 (2008).
92. Z. Ding, S. Bux. D. J. King, F. L. Chang, T. -H. Chen, S. -C. Huang and R. B. Kaner, *J. Mater. Chem.* **19**, 2588 (2009).
- 93 Y. Maréchal, *J. Chem. Phys.* **95**, 5565 (1991).
- 94 W. Kullmann, J. Geurts, W. Richter, N. Lehner, H. Rauh, U. Steigenberger, G. Eichhorn and R. Geick, *Phys. Stat. Sol. (b)* **125**, 131 (1984).
- 95 W. Richter, H. Khler and C. R. Becker, *Phys. Stat. Sol. (b)* **84**, 619 (1977).
96. G. J. Snyder and T. S. Ursell, *Phys. Rev. Lett.* **91**, 148301 (2003).
97. L. D. Hicks and M. S. Dresselhaus, *Phys. Rev. B* **47**, 12727 (1993).
98. L. D. Hicks and M. S. Dresselhaus, *Phys. Rev. B* **47**, 16631 (1993).

99. L. D. Hicks, T. C. Harman, X. Sun and M. S. Dresselhaus, *Phys. Rev. B* **53**, R10493 (1996).
100. M. S. Dresselhaus, G. Dresselhaus, X. Sun, Z. Zhang, S. B. Cronin, T. Koga, J. Y. Ying and G. Chen, *Microscale Thermophysical Engineering* **3**, 89 (1999).
101. T. C. Harman, P. J. Taylor, D. L. Spears and M. P. Walsh, *J. Electron. Mater.* **29**, L1 (2000).
102. T. Koga, S. B. Cronin, M. S. Dresselhaus, J. L. Liui and K. L. Wang, *Appl. Phys. Lett.* **77**, 1490 (2000).
103. T. C. Harman, P. J. Taylor, M. P. Walsh and B. E. LaForge, *Science* **297**, 2229 (2002).
104. J. Martin, G.S. Nolas, W. Zhang and L. Chen, *Appl. Phys. Lett.* **90**, 222112 (2007).
105. B. C. Sales, D. Mandrus, and R. K. Williams, *Science* **272**, 1325 (1996).
106. R. P. Hermann, R. Jin, W. Schweika, F. Grandjean, D. Mandrus, B. C. Sales and G. J. Long, *Phys. Rev. Lett.* **90**, 135505 (2003).
107. B. C. Sales, B. C. Chakoumakos, and D. Mandrus, *Phys. Rev. B* **61**, 2475 (2000).
108. R. P. Hermann, W. Schweika, O. Leupold, R. Ruffer, G. S. Nolas, F. Grandjean and G. J. Long, *Phys. Rev. B* **72**, 174301 (2005).
109. M. Christensen, F. Juranyi, and B. B. Iversen, *Physica* **385–386B**, 505 (2006).

110. W. Schweika, R. P. Hermann, M. Prager, J. Perþon and V. Keppens, *Phys. Rev. Lett.* **99**, 125501 (2007).
111. B. Zhang, J. He, X. H. Ji and T. M. Tritt, *Appl. Phys. Lett.* **89**, 163114 (2006).
112. X. H. Ji, J. He, P. Alboni, Z. Su, N. Gothard, B. Zhang, T. M. Tritt and J. W. Kolis, *Physica Status Solidi (RRL)* **1**, 229 (2007).
113. *Mineral Commodity Summaries 2009*, U.S. Geological Survey, U.S. Department of the Interior, January 2009.